

BLENDING OF INPUTS AND OUTPUTS FOR MODAL CONTROL OF AEROELASTIC SYSTEMS

Manuel Pusch

Blending of Inputs and Outputs for Modal Control of Aeroelastic Systems

Vom Promotionsausschuss der
Technischen Universität Hamburg
zur Erlangung des akademischen Grades
Doktor-Ingenieur (Dr.-Ing.)
genehmigte Dissertation

von
Manuel Pusch
aus
St. Martin

2020

Erster Gutachter:

Prof. Dr. Herbert Werner
Institut für Regelungstechnik
Technische Universität Hamburg

Zweiter Gutachter:

Prof. Dr.-Ing. Dipl.-Math. Johann Bals
Institut für Systemdynamik und Regelungstechnik
Deutsches Zentrum für Luft- und Raumfahrt (DLR)

Vorsitzender des Prüfungsausschusses:

Prof. Dr.-Ing. Gerhard Bauch
Institut für Nachrichtentechnik
Technische Universität Hamburg

Eingereicht am: 30.4.2020

Tag der mündlichen Prüfung: 6.11.2020

Preface

The present thesis is the result of my work at the Institute of System Dynamics and Control at the German Aerospace Center (DLR) in Oberpfaffenhofen, Germany. My thanks go to Prof. Johann Bals not only for giving me the opportunity to do exciting research at his institute but also for all the insightful discussions and for being part of the examination commission. Likewise, I thank Prof. Herbert Werner from Hamburg University of Technology for promoting this thesis and Prof. Gerhard Bauch for chairing the examination commission.

I would like to thank Gertjan Looye for his constant support and for giving me complete freedom in my research. The combination of this freedom with the outstanding mentorship of Prof. Daniel Ossmann was crucial for the output of my research work. But considering Daniel as only a mentor is a gross oversimplification; his constant availability, passion to help and willingness to share goes above and beyond the norm. He truly became a dear friend of mine and I am really grateful for that.

A very special thanks also goes to my friend and colleague Julian Theis who substantially influenced my research direction. He was always available for discussions and never hesitated to ask critical questions. I am also very grateful to my Ph.D. colleagues Alexander Pollok and Daniel Bender who were always there to share my joy and sorrow, of which a profound friendship developed. My thanks further go to Thiemo Kier for introducing me to the complex field of aeroelasticity and for all the exciting business trips we did together. I also wish to express my gratitude to Andreas Knoblach for his immense support during my initial years at DLR and the many technical as well as personal discussions we have had. Just as I am indebted to all other former and current colleagues at the Institute of System Dynamics and Control who created such a pleasant working atmosphere and helped me with any and all kinds of problems.

Moreover, I would like to thank Prof. Wolf-Reiner Krüger from the Institute of Aeroelasticity at DLR in Göttingen for giving me the opportunity to test the developed control algorithms on a flexible wing in a wind tunnel. My gratitude also goes to Johannes Dillinger, Martin Tang and Jannis Lübker who supported me in preparing and conducting the wind tunnel tests. It was truly inspiring to work together with such skilled researchers and showed me how much can be gained from real teamwork.

This thesis would not have been possible without all my long-term friends standing by my side at all times, in particular, David Reiter, Manuel Burkart,

Joachim Schulze-Ardey, and Andreas Jankl. Thank you for keeping me in balance and all the incredible moments we have had together. Likewise, a heartfelt thanks also goes to my brother Benedikt who helped me with numerous graphical issues not only within this dissertation. Furthermore, I would like to give credit to Tobias Posielek, Tamás Baár and Romaria Lindorfer for carefully proof-reading my thesis and all their constructive feedback.

My deepest gratitude goes to my parents Erwin and Elfriede Pusch who stood behind me at all times and provided me with the basis which made it possible to explore the beauty of this world. They have always promoted critical thinking and encouraged me to pursue my own ideas, which I consider as cornerstones for accomplishing a Ph.D. I am also forever grateful to my brothers Dominik, Johannes and Benedikt for all their support and the fact that I can always count on them. Finally, I would like to sincerely thank my grandmother Anna Pusch whose way of living has always inspired me. She appreciates every single day with vigor and I remain impressed with her incredible positive mindset and her openness to change. I would like to dedicate this thesis to her and thank her for being part of my life.

Abstract

Highly fuel-efficient aircraft designs often suffer from undesired aeroelastic effects, or more specifically, from interactions of structural dynamics and aerodynamics that can cause large structural loads or even instabilities. To counteract these adverse effects, active control of critical aeroelastic modes during flight is becoming increasingly important. To this end, more and more sensors and control surfaces are installed on aircraft, enabling an improved controller performance at the cost of a more complicated design.

In this thesis, two novel modal control approaches for linear time-invariant systems are developed which are based on blending, i.e., weighting and summing up, of control inputs and measurement outputs. In doing so, the original multivariable control problem for controlling a specific targeted mode is reduced to a “single-input single-output” one. In the first approach, input and output blending vectors are computed such that controllability and observability of the targeted mode are maximized in terms of the \mathcal{H}_2 norm. The second control approach searches for blending vectors which allow the poles of the targeted mode to be shifted to desired locations in the complex plane with a minimum static feedback gain. In both approaches, the respective blending vector design problem is formulated as an unconstrained optimization problem of a single variable. This means that controller synthesis becomes independent of the number of actual inputs and outputs. Taking into account explicit mode decoupling constraints, it is ensured that the residual system dynamics are not affected and that each targeted mode can be controlled independently. To further consider actuator constraints like saturation or faults, an enhancement of the proposed control approaches is presented making use of real-time control allocation.

The effectiveness and applicability of the proposed control methods are validated based on three realistic aeroelastic systems. In the first application, a large transport aircraft is considered for which the structural loads during gust encounters are reduced by actively damping the first two wing bending modes. In the second application, a flutter suppression controller is designed to increase the operational velocity range of an unmanned aerial vehicle by stabilizing undesired interactions of structural dynamics and aerodynamics. The third application considers an experimental flexible wing for which a gust load alleviation controller is designed taking into account actuator constraints. The great potential of the proposed control approaches is not only demonstrated by comprehensive linear and nonlinear simulations but also confirmed in extensive wind tunnel tests with the experimental flexible wing.

Contents

Notation	iii
Acronyms and Abbreviations	v
1 Introduction	1
1.1 Control of Aeroelastic Systems	2
1.1.1 Challenges in Control of Aeroelastic Systems	3
1.1.2 Control Concepts for Aeroelastic Systems	4
1.2 Blending-based Modal Control	6
1.3 Main Contributions	7
1.4 Outline	10
2 Background and Review on Blending Techniques	13
3 Blending of Inputs and Outputs for Modal Control	19
3.1 Preliminaries	19
3.1.1 Modal Decomposition of LTI Systems	19
3.1.2 Modal Controllability and Observability	21
3.1.3 Modal Control using Blended Inputs and Outputs	24
3.2 \mathcal{H}_2 -optimal Blending of Inputs and Outputs	27
3.2.1 Problem Definition	27
3.2.2 Efficient \mathcal{H}_2 Norm Computation	28
3.2.3 Efficient Blending Vector Computation	30
3.2.4 Special Cases and Additional Aspects	32
3.2.5 Summary \mathcal{H}_2 -optimal Blending Vector Computation	38
3.2.6 Numerical Examples	39
3.3 Blending-based Pole Placement	43
3.3.1 Problem Definition	43
3.3.2 Efficient Blending Vector Computation	47
3.3.3 Special Cases	49
3.3.4 Summary Blending-based Pole Placement Algorithm	51
3.3.5 Numerical Examples	52
3.4 Spillover Suppression	56
3.4.1 Dynamic Filtering	56
3.4.2 Blending Vector Design with Explicit Mode Decoupling	57
3.5 Handling Actuator Constraints using Control Allocation	59

4	Modeling Aeroelastic Systems	63
4.1	Structural Dynamics Model	63
4.2	Aerodynamics Model	64
4.3	Actuators and Sensors	65
4.4	Model Integration	66
5	Application to Aeroelastic Systems	67
5.1	Active Gust Load Alleviation for a Large Transport Aircraft . . .	67
5.1.1	Aircraft Modeling and Analysis	68
5.1.2	Gust Load Alleviation Controller Design	70
5.1.3	Controller Validation	76
5.1.4	Conclusions	79
5.2	Active Flutter Suppression for an Unmanned Aerial Vehicle . . .	80
5.2.1	Aircraft Modeling and Analysis	81
5.2.2	Flutter Suppression Controller Design	83
5.2.3	Controller Validation	87
5.2.4	Conclusions	91
5.3	Control of a Highly Flexible Wing in a Wind Tunnel	93
5.3.1	Wing Modeling	95
5.3.2	Gust Load Alleviation Controller Design	98
5.3.3	Experimental Validation	101
6	Conclusions	113
A	Appendix	117
A.1	Linear Independent Inputs and Outputs	117
A.2	Proportional-Derivative Controller for Mode Damping	118
	Bibliography	119
	List of Publications	I
	Curriculum Vitae	V

Notation

\mathbb{R}	field of real numbers
$\mathbb{R}_{\geq 0}$	field of non-negative real numbers
$\mathbb{R}_{> 0}$	field of positive real numbers
$\mathbb{R}_{\leq 0}$	field of non-positive real numbers
$\mathbb{R}_{< 0}$	field of negative real numbers
$\mathbb{R}_{\neq 0}$	field of real numbers without zero
$\mathbb{R}^{n \times m}$	set of n -by- m matrices with elements in \mathbb{R}
\mathbb{C}	field of complex numbers
$\mathbb{C}^{n \times m}$	set of n -by- m matrices with elements in \mathbb{C}
j	imaginary number defined as the solution of $j^2 = -1$
s	Laplace variable
I	identity matrix of adequate dimension
0	zero matrix of adequate dimension
X^T	transpose of a matrix X
X^H	Hermitian transpose of a matrix X
X^{-1}	inverse of a matrix X
\dot{x}	derivative of a function x with respect to time
$\Re(x)$	real part of x
$\Im(x)$	imaginary part of x
$ x $	absolute value of x
$\ x\ _2$	2-norm of x
$\ x\ _{\mathcal{H}_2}$	\mathcal{H}_2 norm of x
$\ x\ _{\mathbb{F}}$	Frobenius norm of x
$\text{diag}(x)$	diagonal matrix with the elements of vector x on its diagonal
\square	end of proof
\triangle	end of example

Acronyms and Abbreviations

DLM	doublet lattice method
DOF	degrees of freedom
FE	finite element
FFT	fast Fourier transformation
GLA	gust load alleviation
IMU	inertial measurement unit
LMI	linear matrix inequality
LTI	linear time-invariant
LPV	linear parameter-varying
MIMO	multi-input multi-output
PI	proportional-integral
RMS	root mean square
SISO	single-input single-output
SVD	singular value decomposition
UAV	unmanned aerial vehicle
WRBM	wing root bending moment
e.g.	for example (<i>exempli gratia</i>)
i.e.	that is (<i>id est</i>)
s.t.	subject to

1 Introduction

In order to allow for a more economic and environmentally friendly operation of aircraft, fuel savings are imperative. In this regard, the enormous progress over the past decades is depicted in Figure 1.1 [68], showing a continuous decrease in fuel consumption of commercial airliners. For example, Airbus claims a 25 % lower fuel burn of its latest aircraft family, the A350, when compared with previous-generation aircraft [2]. Another example manifesting this trend is the promise of Boeing to reduce fuel consumption by another 10 % with their new 777X aircraft [20], whose maiden flight took place recently.

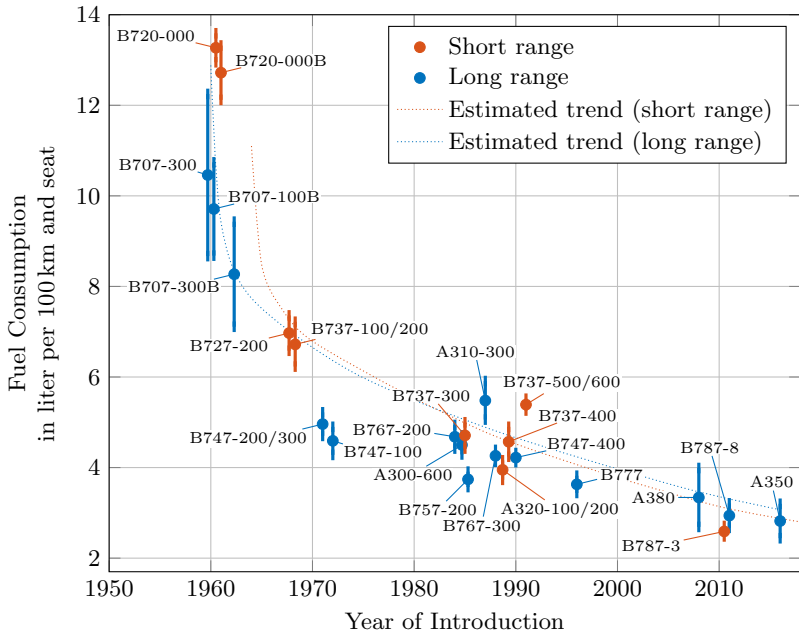


Figure 1.1: Evolution of fuel consumption of commercial aircraft [68, 80]. The error bar for each aircraft comprises different configurations.

Apart from extensive advancements in propulsion technologies, this trend in fuel consumption is largely driven by improvements in aerodynamic efficiency and structural weight reduction [68]. Thereby, composite materials and tailored structures play a key role, allowing for lightweight wing designs which feature a high aspect ratio for a reduced aerodynamic drag. However, these high-aspect-ratio wings, i.e., slender wings of large span, often suffer from an increased flexibility and adverse couplings of structural dynamics and aerodynamics. This coupling is generally known as *aeroelasticity* [24] and considered as one of the major challenges in improving aircraft performance [93]. One example of such adverse aeroelastic effects are lightly damped oscillations which are easily excitable, e.g., by external disturbances like gusts or by control surface deflections commanded by the (auto)pilot. As a result, structural loads are typically increased, and passenger comfort and handling qualities are often degraded. In extreme cases, such couplings can even lead to phenomena like flutter, divergence, or buffeting, which are instabilities and inherently yield structural damage [17]. To counteract these adverse aeroelastic effects and the resulting design limitations, active control technology is increasingly used [32, 152]. This comes along with several new challenges for control engineers [94]. Within this thesis, these challenges are explicitly addressed and control approaches are developed which seek to meet them.

1.1 Control of Aeroelastic Systems

Over the past decades, a large variety of control systems for aeroelastic vehicles have been developed and successfully implemented in series as summarized, e.g., in [94, 109, 132]. One of the first prominent examples is the Rockwell B-1 Lancer, for which a structural mode control system has been developed back in the 1970s to suppress undesired vibrations in the cockpit [168]. Since a simplified aeroelastic model resembling the B-1 aircraft dynamics is nowadays freely available [144], it has become subject to many research studies such as [60, 153]. Another example is a comfort enhancement system implemented on the Airbus A330 and A340 aircraft, which increases the damping of the fuselage during turbulence using the rudder and the elevators [62, 132]. Besides that, control functions for reducing structural loads during turbulence and maneuvers are nowadays standard for large transport aircraft such as the Airbus A380 or the Boeing 787 [132]. A further, rather recent example is the Boeing 747-8 aircraft, where limit cycle oscillations are actively suppressed using the outboard ailerons [35]. The Boeing 747-8 received special attention since this can be seen as an active flutter suppression, which has not been certified on a commercial airliner ever before.

1.1.1 Challenges in Control of Aeroelastic Systems

In the early years, aeroelastic control was mainly used to mitigate design problems such as the undesired vibrations of the B-1 Lancer. In contrast, nowadays, it is aimed at including active control technology from the onset of the aircraft design process [92, 124, 149]. This enables, for instance, weight-optimized aircraft designs by incorporating the beneficial effects of control functions like active load alleviation. The effectiveness of the control system, in turn, depends on the number and type of control surfaces and measurements, which are further parameters to be optimized during aircraft design. Thereby, advances in actuation and sensing technologies provide new possibilities in improving the performance and reliability of the control system and thus the overall aircraft. For instance, sophisticated sensors like micro-electro-mechanical accelerometers or fiber optical sensors enable a large number of highly accurate measurements at low cost [4, 83]. Similarly, smart materials based on, e.g., smart memory alloys or piezoelectric ceramics allow for a fast and precise control of aircraft structures [15, 111]. An example of a promising concept is the *variable camber continuous trailing edge flap* (VCCTEF) [111, 113], which is depicted in Figure 1.2. The VCCTEF features numerous span-wise flaps, where each flap itself consists of three chord-wise segments, allowing for a targeted control of the wing shape and thus the local lift, drag, and loads. Increasing the number of control effectors and measurements, however, generally complicates controller design and requires sophisticated synthesis methods with dedicated tuning capabilities. Additionally, advanced control techniques are required to take advantage of possible actuator and sensor redundancies in case of failure or saturation.

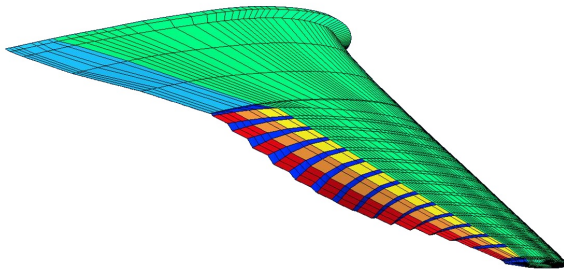


Figure 1.2: The *variable camber continuous trailing edge flap* (VCCTEF) concept, consisting of 42 individually controllable segments [112].

For a sophisticated control design, a thorough modeling of the complex coupling of structural dynamics and aerodynamics is required. To that end, the structural dynamics and aerodynamics are usually modeled separately and afterwards interconnected as depicted in Figure 1.3. Both models are commonly derived using methods based on discretization [17] and are generally of large order, especially when considering unsteady aerodynamics and complex aircraft structures [80, 152]. On top of that, the dynamics of an aeroelastic system usually depend on parameters like the velocity of the surrounding airflow or the aircraft mass, which can change substantially during flight. And even though great progress in aeroelastic modeling has been made over the years, modeling accuracy especially of the aerodynamics is still limited. Hence, aeroelastic controller design generally faces uncertain models of high order which are parameter-dependent.

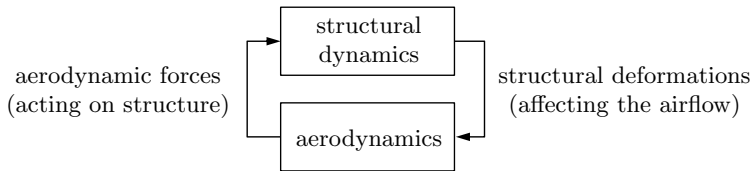


Figure 1.3: Aeroelasticity, described as a feedback interconnection of structural dynamics and aerodynamics.

Taking a closer look at the considered control problem, i.e., the mitigation of adverse aeroelastic effects, it can often be seen as a modal control problem. This is due to the fact that most adverse aeroelastic effects can be characterized by individual modes which are unstable or feature an insufficient damping. When controlling these critical aeroelastic modes, it is commonly desired to leave the remaining system dynamics unaffected. This involves, for instance, the rigid-body dynamics of the aircraft, which are typically controlled separately, or other non-critical aeroelastic modes. In highly optimized aircraft designs, however, aeroelastic modes and also rigid-body dynamics are often tightly spaced in frequency, which certainly complicates a targeted mode control.

1.1.2 Control Concepts for Aeroelastic Systems

To cope with the described challenges in aeroelastic control, a great variety of multi-input multi-output (MIMO) control approaches has been applied. An overview of different aeroelastic control applications is given, e.g., in [93, 109, 152], where the used control methods and design procedures are reviewed as follows.

Specifically controlling the modes of a system or placing its poles is generally known as modal control, a term first introduced by Rosenbrock in the 1960s [137]. When all states are measured, an arbitrary pole placement can be achieved by a static feedback of the system's states, see, e.g., [1, 136, 137]. If state measurements are not possible, state observation methods are commonly applied, introducing additional dynamics into the control system [95, 120]. A different approach is to formulate the closed-loop specifications in terms of the \mathcal{H}_2 or \mathcal{H}_∞ norm, which is then minimized during controller synthesis [33, 169]. The resulting controller commonly has the same order as the synthesis model augmented with tunable weighting filters to impose the closed-loop specifications. This means that if the number of inputs and outputs increases, typically the controller order and the number of free tuning parameters also increases. In practice, however, low-order controllers which are easy to tune are desired or even necessary for numerically stable controller design and tuning. To keep the controller order low, model order reduction routines are often applied on the synthesis model or the controller itself [105, 142], whereby closed-loop guarantees are commonly lost. As an alternative, structured controller design directly optimizes the controller gains [7, 73]. Thereby, the challenge is to choose an adequate controller structure with a minimum number of free parameters and find a satisfactory solution to the generally non-convex design problem. In this respect, the simplest controller structure certainly consists of static feedback gains, for what numerous dedicated synthesis algorithms exist [141], but which commonly also suffer from a bad scaling with the number of inputs and outputs [150]. Another technique is to decentralize the control design process and implement multiple independent controllers [11, 27], which often leads to a limited overall controller performance. A famous approach of this category is collocated control [13, 121], where easily tunable single-input single-output (SISO) loops are created by connecting nearby actuators and sensors.

Besides an increasing number of inputs and outputs, aeroelastic controller design also needs to deal with the limited accuracy of aeroelastic models and their parameter-varying nature. One way of doing that is to consider a set of models instead of a single model for controller design, which is also known as multi-model controller design [6, 14]. The challenge thereby is to select an adequate set of models optimally reflecting the entire parameter space and uncertainties, where it is noted that closed-loop guarantees are only given for the selected models. A more systematic approach is robust control or μ -synthesis, where uncertainties and parameter variations of bounded magnitude can be considered in an integrated way [118, 170]. The resulting controllers are often conservative [16], which may be evaded by introducing gain-scheduling in dependence of known varying parameters [87]. Thereby, the well-known linear parameter-varying (LPV) framework provides a large body of theoretical results for performance and stability guarantees not only at chosen design points but also

in between [147, 165]. In practice, however, computational complexity for LPV controller synthesis scales badly with the order of the model and requires advanced model order reduction techniques to be applicable to aeroelastic systems [43, 108, 157].

To enable a maximum reliability and performance of the control system, also actuator constraints such as faults or saturation need to be considered. This may be achieved by exploiting the versatility of the LPV framework [37, 166], e.g., by introducing a so-called saturation indicator as a scheduling variable. Other prominent approaches for coping with actuator constraints include control allocation [34, 72] or model predictive control [44, 107]. In both approaches, a constrained optimization problem is solved at each sampling instance, which generally limits the size of the problem to be solved. Last but not least, the vast field of adaptive and artificial intelligence control methods provides promising approaches for dealing with uncertain and changing system dynamics [8, 140]. In aerospace industry, however, high costs of extensive in-flight tests and certification requirements reflecting the high safety demands still hinder their broad application [93].

1.2 Blending-based Modal Control

The issues with the discussed control approaches call for breaking down the original control problem into smaller ones which can then be solved using common tools that do not scale up well. Thereby, a promising approach is to reduce the complexity of the control problem by introducing virtual inputs and virtual outputs. The virtual inputs and outputs are computed from the actual control inputs and measurement outputs, and are commonly dedicated to a specific control goal. By dedicating the virtual inputs and outputs to a specific control goal, the subsequent controller design is typically greatly facilitated since it becomes independent of the number of actual inputs and outputs. The corresponding control approach has been denoted as *virtual control* [113], where also other denotations exist depending on the method used or the actual control objective, see Chapter 2 for more details.

In this thesis, the virtual input and output signals are computed via frequency-independent linear transformations, or in other words, by blending control inputs and measurement outputs. Hence, the term *blending-based control* is introduced and used throughout the thesis, where the general idea of blending-based control is depicted in Figure 1.4. Considering modal control problems such as the mitigation of adverse aeroelastic effects, it is proposed herein to generate virtual inputs and outputs which are dedicated to the modes to be controlled. As a result, each targeted mode can be controlled by a separate SISO controller, which is typically of low order and hence can easily be tuned and gain-scheduled.

For the design of the corresponding input and output blending vectors or matrices, the goal is to decouple the targeted modes not only from the remaining system dynamics but also from each other. Furthermore, it is desired that the blending of inputs and outputs maintains a maximum controllability and observability of the targeted modes. This allows for decreasing the feedback gains of the individual SISO controllers and thereby minimizes actuator action and increases robustness. The overall order of the resulting controller follows from the individual orders of the SISO controllers, which can typically be tuned on the full-order model. Thus, performance losses or stability issues due to model order reduction are avoided effectively.

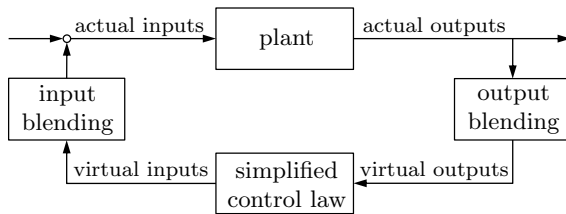


Figure 1.4: Blending-based feedback control.

1.3 Main Contributions

The present thesis addresses control problems arising from highly fuel-efficient aircraft configurations that suffer from undesired interactions of structural dynamics and aerodynamics. Thereby, a major challenge is to specifically control individual critical modes out of a large number of modes using an increasing number of control inputs and measurement outputs. To tackle this problem, two novel modal control methods are developed in this thesis which are based on blending control inputs and measurement outputs. In doing so, the original MIMO control problem is reduced to a SISO control problem, whereby controller design and tuning is greatly facilitated. The contributions of this thesis are divided into theoretical and practical contributions. The theoretical contributions refer to the mathematical background of the respective control methods and the practical contributions comprise the validation of the proposed control methods on realistic aeroelastic applications.

The first major theoretical contribution is a control method which is based on an \mathcal{H}_2 -optimal blending of inputs and outputs for controlling a specific mode. Thereby, the \mathcal{H}_2 norm is considered as a measure for the combined controllability and observability of the targeted mode. Hence, maximizing the \mathcal{H}_2 norm in blending vector design allows reducing the feedback gains in subsequent SISO

controller design. To efficiently compute the corresponding blending vectors, a new theorem for determining the \mathcal{H}_2 norm of an individual mode is derived in Section 3.2.2. The theorem does not require to solve any Lyapunov equation and is considered as the second major contribution of this thesis. Additionally, the \mathcal{H}_2 -optimal blending approach is generalized to also consider unstable or undamped modes, for which the \mathcal{H}_2 norm is not defined. The overall \mathcal{H}_2 -optimal blending approach is described in Section 3.2 and was published in [126].

The third major theoretical contribution refers to a blending-based control approach for placing the pole or conjugate complex pole pair of an individual mode at a predefined location. Thereby, the desired pole shift is achieved by feeding back blended outputs to blended inputs with a static gain of minimal magnitude. This requires that the blending of inputs and outputs generates a SISO loop with a desirable root locus along which the targeted poles are moved. The resulting feedback controller is static and of rank one since it consists of the input and output blending vectors scaled by the static feedback gain. The blending-based pole placement approach is described in Section 3.3 and was published in [129].

Both control approaches are developed considering only a single mode but are generalized for controlling multiple modes. To that end, different methods for decoupling the targeted modes from each other as well as from the residual system dynamics are proposed in Section 3.4. The decoupling methods are based on either the frequency or the shape of the modes to be decoupled, where the former is included in SISO controller design and the latter in blending vector design. Furthermore, both blending vector design problems are formulated as unconstrained optimization problems of a single variable, regardless of whether mode decoupling is enforced or not. This means that controller synthesis becomes independent of the number of actual inputs and outputs, which makes the proposed control approaches especially attractive for systems with a large number of inputs and outputs.

Another main theoretical contribution is the consideration of actuator constraints such as faults or saturation in blending-based control laws. For this purpose, the virtual inputs are distributed to the actual control inputs in real-time by making use of a dynamic control allocation. The corresponding control allocation problem is formulated as a convex optimization problem that aims at maintaining nominal controller performance as effectively as possible without exceeding actuator limitations. In that way, actuator redundancy is optimally exploited allowing for increasing not only the reliability of the control system but also its performance. The proposed augmentation of a blending-based control law with dynamic control allocation is described in Section 3.5 and was published in [115].

In order to demonstrate the practical relevance of the theoretical contributions, the proposed control methods are validated on three realistic aeroelastic

applications. As a first application, a large transport aircraft is considered for which the structural loads during gust encounters are reduced by actively damping the first two wing bending modes. Both the \mathcal{H}_2 -optimal blending and the blending-based pole placement approach are applied in order to demonstrate and compare their strengths and weaknesses. During the design of both controllers, special care is taken not to affect any other modes, especially not the ones associated with the rigid-body motions since they are controlled separately. For the given active damping control problem, concrete guidelines for tuning the two different controllers are given by introducing a single tuning parameter for each mode to be damped. Both controllers are thoroughly tested using standardized gust simulations and show similarly good load alleviation capabilities. The promising simulation results and general design procedure of the two blending-based controllers are described in Section 5.1. Preliminary results were published in [123], where the \mathcal{H}_2 -optimal blending approach is applied to a derivative of the considered large transport aircraft.

In the second application, a flutter suppression controller is designed to extend the operational velocity range of an unmanned aerial vehicle (UAV) by stabilizing undesired interactions of structural dynamics and aerodynamics. To that end, the generalized \mathcal{H}_2 -optimal blending approach is used, proving its applicability also to unstable systems. The effectiveness of the derived controller is thoroughly evaluated in nonlinear simulations including also the primary flight control system. The overall controller design procedure for active flutter suppression and the corresponding simulation results are described in Section 5.2 and were published in [128].

The third and final application considers an experimental flexible wing for which a gust load alleviation controller is designed taking into account actuator constraints. This is achieved by actively damping the first wing bending mode using the \mathcal{H}_2 -optimal blending approach in combination with the proposed control allocation. The gust load alleviation controller is successfully validated in extensive wind tunnel tests including a variety of gust excitations at multiple airspeeds, and different actuator saturation and fault scenarios. The controller design procedure and the experimental results are described in Section 5.3 and were published in [86, 115, 127].

In all three applications, the respective blending-based controllers are designed on full-scale aeroelastic models, which are of large order by nature. The direct use of high-order models is enabled by splitting up controller design into a blending vector design and a SISO controller design, two separate but less complex problems. Furthermore, in the latter two applications, overall controller performance is increased by scheduling the gains of the respective SISO controllers. This proves that blending-based control opens up new possibilities for a gain-scheduled controller design, which can quickly become challenging for systems with a large number of inputs, outputs, or states.

1.4 Outline

The structure of the thesis is given as follows and illustrated in Figure 1.5. In Chapter 2, the idea of blending-based control is detailed and existing blending methods are reviewed and categorized. In Chapter 3, preliminaries on modal control are given and the two different blending vector design methods for controlling individual modes are developed. The corresponding blending vector computation algorithms are compactly summarized to allow for a direct application and system-theoretical special cases are discussed. Additionally, numerical examples are given for a better understanding and for illustrating important aspects of each blending method. Moreover, advanced extensions for blending-based control laws are proposed to systematically handle spillover effects and actuator constraints.

In the latter part of the thesis, the developed blending-based control approaches are validated on three different aeroelastic systems: a large transport aircraft, an unmanned aerial vehicle, and a flexible wing in a wind tunnel. To that end, the corresponding aeroelastic systems are first modeled using the approach described in Chapter 4. The actual controller design and validation procedure for stabilizing or damping critical aeroelastic modes is then described in Chapter 5. This includes a thorough evaluation of the performance of each control law by means of comprehensive simulations and, for the flexible wing, also by extensive wind tunnel tests.

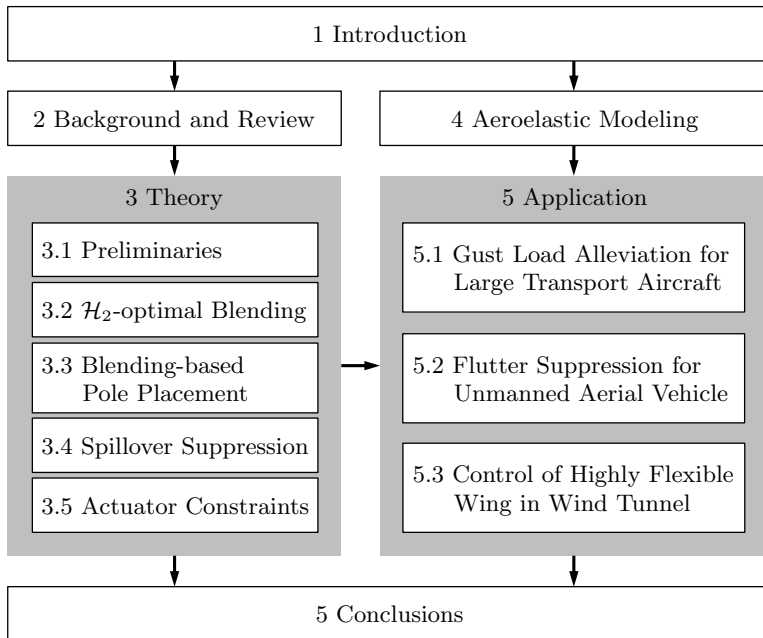


Figure 1.5: Dependency graph of thesis chapters.

2 Background and Review on Blending Techniques

In this chapter, the blending-based control concept introduced in Section 1.2 is further detailed and a review on existing blending techniques is given.

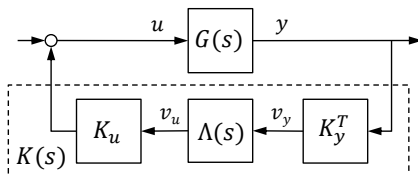


Figure 2.1: Feedback interconnection of blending-based controller $K(s)$ and plant $G(s)$.

In blending-based control, a virtual output $v_{y,i}$ is generated by blending the actual measurements y using an output blending vector $k_{y,i} \in \mathbb{R}^{n_y}$. Or more generally, a set of virtual outputs $v_y = [v_{y,1} \cdots v_{y,n_i}]^T$ is computed as

$$v_y = K_y^T y,$$

where the output blending matrix $K_y = [k_{y,1} \cdots k_{y,n_i}]$ collects the corresponding output blending vectors $k_{y,i}$, $i = 1, \dots, n_i$. Similarly, a virtual input $v_{u,j}$ is distributed to the actual control inputs u by means of an input blending vector $k_{u,j} \in \mathbb{R}^{n_u}$. Considering multiple virtual inputs $v_u = [v_{u,1} \cdots v_{u,n_j}]^T$, the actual control inputs are computed as

$$u = K_u v_u,$$

where the input blending matrix $K_u = [k_{u,1} \cdots k_{u,n_j}]$ collects the corresponding input blending vectors $k_{u,j}$, $j = 1, \dots, n_j$. By means of the generated virtual inputs and outputs, the design of a “simplified” control law $\Lambda(s)$ is enabled. Thereby, “simplified” may refer to, e.g., a diagonal controller structure or a reduced number of inputs and outputs of $\Lambda(s)$. The overall feedback controller is depicted in Figure 2.1 and given as

$$K(s) = K_u \Lambda(s) K_y^T. \quad (2.1)$$

Herein, the input and output blendings are considered to be real-valued, i.e., *static* matrices, which may restrict achievable controller performance. Replacing K_u and K_y by *dynamic* filters, however, introduces additional degrees of freedom. This contradicts the general idea of facilitating the control design procedure for multivariable systems. Hence, in the following literature review, only *static* blending approaches are considered, which are classified according to the following principal objectives:

- reduction of inputs and outputs
- decoupling of inputs and outputs
- isolation of system dynamics.

All three objectives are considered to simplify the subsequent controller design and are discussed as follows. Note that most of the reviewed methods are not known as *blending methods* but can be seen as suchlike. Respective *dynamic* blending approaches are well summarized and documented in, e.g., [91, 158].

Reduction of Inputs and Outputs

In control design, corresponding tuning parameters are often associated with the control inputs and measurement outputs of the underlying system. This allows, for instance, to weight the usage of individual actuators or the importance of a single measurement. However, for systems with a large number of control inputs or measurement outputs, the tuning of the corresponding weights may become cumbersome. Hence, generating a reduced number of virtual inputs and virtual outputs and using them for controller design offers a great possibility to facilitate controller design and tuning.

One of the most basic blending approaches is to use polynomials for generating the virtual inputs or virtual outputs. Thereby, the coefficients of the chosen polynomial are considered as the virtual inputs or outputs and the indeterminate is associated with the actual control input or measurement output, respectively. To illustrate this, the following example is given.

Example 2.1. Considering the coefficients $v_{u,1}$, $v_{u,2}$ and $v_{u,3}$ of a quadratic polynomial as virtual inputs, the i^{th} control input as

$$u_i = v_{u,1} + v_{u,2} i + v_{u,3} i^2,$$

where indeterminate i reflects the index of the respective control input. The

resulting input blending matrix is hence given as

$$K_u = \begin{bmatrix} 1 & 1 & 1 \\ 1 & 2 & 2^2 \\ \vdots & \vdots & \vdots \\ 1 & n_i & n_i^2 \end{bmatrix}$$

and allows controlling an arbitrary large number of control inputs u_i , $i = 1, \dots, n_i$ by a reduced number of virtual inputs $v_{u,j}$, $j = 1, 2, 3$. \triangle

To also take into account the spatial location of the corresponding actuators or sensors, multivariate polynomials can be used with each indeterminate representing a different spatial direction. In [113], virtual control inputs based on Fourier series are introduced for wing shape control, where both the span- and chord-wise actuator locations are taken into account. Since the considered wing cannot be deformed arbitrarily, the deflection difference of neighboring actuators is physically limited, which can be ensured by choosing a sufficiently small polynomial degree. Other similar approaches are described in [21] and [134], where virtual control inputs are generated using Chebyshev and Bernstein polynomials, respectively. However, these types of polynomials do not consider any control objective and thus, achievable controller performance is typically limited.

As a remedy, [122] proposes to blend control inputs based on the control objective formulated in terms of dedicated transfer channels. To that end, a balancing state space transformation is performed, where the obtained Hankel singular values are used as a measure for selecting an adequate number of virtual inputs. This is very useful since both controller complexity and achievable performance generally increase with the number of virtual inputs and hence need to be carefully balanced.

Decoupling of Inputs and Outputs

Apart from reducing the number of inputs and outputs, blending can also be used to diagonalize the whole underlying MIMO system such that each virtual input controls a single virtual output. This assumes that the underlying system, and the input and output blending matrices are quadratic, i.e., $n_u = n_y = n_i = n_j$. In the ideal case, the blending of inputs and outputs yields the diagonal system $K_y^T G(s) K_u = \text{diag}([g_1(s) \dots g_{n_i}(s)])$. Thereby, each decoupled subsystem $g_i(s)$, $i = 1, \dots, n_i$ can be individually controlled by a separate SISO controller. Quadratic MIMO systems which can be perfectly diagonalized are called *dyadic*, where corresponding blending matrices can be directly computed, e.g., by the algorithm proposed in [116]. In general, however, a perfect

diagonalization is not possible and only an approximation with dominating diagonal elements can be achieved.

One of the most basic approaches to approximately diagonalize a quadratic system is to scale control inputs and measurement outputs [101]. The resulting blending matrices are diagonal, which usually limits decoupling accuracy since input and output signals are not blended but only weighted.

A more advanced approach, denoted as *approximate commutative control* [97], blends inputs and outputs based on the eigenvectors of the frequency response at a certain frequency ω_0 . Thereby, the so-called *ALIGN procedure* [82] is applied to obtain real-valued approximations of the generally complex-valued eigenvectors. However, the quality of the overall system decoupling greatly depends on the choice of the frequency ω_0 and may only be accurate in the vicinity of ω_0 . To select an optimal ω_0 which maximizes decoupling accuracy, [158] formulates a corresponding optimization problem using μ -analysis. Alternatively, [98] extends the *ALIGN procedure* to consider not only a single but multiple frequencies.

Another approach is the *approximate reversed frame normalization* [66], which uses singular value decomposition (SVD) instead of eigendecomposition for decoupling inputs and outputs. Thereby, the complex-valued singular vectors are approximated based on a so-called quasi-Nyquist decomposition which adds the phase information of the singular vectors to the singular values. In comparison to *approximate commutative control*, the *approximate reversed frame normalization* generally achieves a better numerical stability and is less sensitive to noise in the frequency response. In [64], optimality of the so-called *SVD controllers* in terms of \mathcal{H}_2 -, \mathcal{H}_∞ - and μ -optimal control is investigated for a special class of systems which can be decomposed as $G(s) = U\Sigma(s)V$. Thereby, U and V are unitary real-valued matrices and $\Sigma(s)$ describes a diagonal transfer function matrix. The results of [64] have been generalized and extended in [160], where blended inputs and outputs may not only be decoupled but also reduced in number.

In *pseudo-diagonalization* [98], the entries of the blending matrices are directly optimized to yield a diagonal dominance at multiple frequencies. The resulting mathematical problem of simultaneously diagonalizing a set of matrices may be solved using a Jacobi iteration when formulating it as an *simultaneous generalized Schur decomposition* [28]. Blending only inputs or only outputs yields simplified optimization problems, which can be formulated as linear matrix inequalities (LMIs) [23] or even be solved analytically [57]. Besides that, the achievable performance of the subsequently designed SISO controllers may also be considered in the optimization problem. This is proposed, e.g., in [158], where a non-convex optimization problem is formulated based on the μ -interaction measure given in [52].

Isolation of System Dynamics

A slightly different but similar objective for blending vector design is to isolate the system dynamics of interest in order to control them without affecting the rest of the system. Again, the goal is to obtain a diagonal system $K_y^T G(s) K_u = \text{diag}([g_1(s) \dots g_{n_j}(s)])$, where the isolated SISO subsystems $g_j(s)$, $j = 1, \dots, n_j$ describe the system dynamics to be actively controlled. This means that K_u and K_y feature the same number of columns, i.e., the number of generated virtual inputs and virtual outputs is equal but may vary from the number of the actual inputs and outputs.

In the ideal case, a full mode decoupling can be achieved, i.e., each mode can be controlled by a separate SISO controller. This, however, requires a sufficient number of suitable control inputs and measurement outputs as stated in the necessary conditions formulated in [67]. A corresponding control approach is the *independent modal space control* [104], which is based on matrix inversion and developed for controlling flexible structures. However, note that flexible structures generally feature an infinite number of modes and hence, with a finite number of actuators and sensors only a finite number of modes can be controlled. Another similar blending approach is presented in [45] and extended in [42], where *modal actuators and sensors* are designed for controlling individual flexible modes. Besides, the blending of inputs and outputs may also be used to isolate the rigid-body modes of mechanical systems like, e.g., a levitated beam [145] or a robot [29].

In case it is desired to decouple one part of the system dynamics from the other, corresponding blending approaches are presented in [9] and [10]. Both approaches formulate the blending vector design problem in terms of LMIs, where the input and output blending vectors are computed separately in an iterative way. One specific goal thereby is to control a single mode $M(s)$ without affecting the rest of the system $G(s)$. In other words, the goal for designing the input and output blending vectors k_u and k_y is to isolate $M(s)$ from $G(s)$ such that $k_y^T G(s) k_u \approx k_y^T M(s) k_u$. This may be achieved by directly using the shape of the targeted mode as blending vectors as proposed by [63]. Another approach is *modal isolation and damping for adaptive aeroservoelastic suppression (MIDAAS)* [26], which computes input and output blending vectors by different methods in an iterative way and directly provides a static gain feedback controller of rank one. The *MIDAAS* approach has been successfully validated in real-time piloted simulations [26] and flight test experiments [25, 81] with goal to increase modal damping of lightly damped or even unstable aeroelastic modes. The same goal of controlling individual aeroelastic modes is followed in this thesis. To that end, two new blending vector design approaches are developed in the following chapter, focusing on a joint design of the interdependent input and output blending vectors.

3 Blending of Inputs and Outputs for Modal Control

In this chapter, two novel blending methods for individual mode control are developed based on the initially discussed preliminaries. The first blending method aims at emphasizing the targeted mode by maximizing its controllability and observability in terms of the \mathcal{H}_2 norm. The second method aims at blending inputs and outputs such that a desired pole shift is enabled with a static gain feedback of minimum magnitude. Both methods focus on controlling individual modes respectively poles, and allow taking into account spillover effects from residual modes. Additionally, an extension to handle actuator constraints is developed which is based on real-time control allocation.

3.1 Preliminaries

The preliminaries given in this section start with modal decomposition of linear time-invariant (LTI) systems. Subsequently, methods for assessing controllability and observability of individual modes are discussed. Eventually, the general modal control approach followed in this thesis is introduced.

3.1.1 Modal Decomposition of LTI Systems

An LTI system with n_u inputs, n_y outputs and n_x states can be represented in state space as

$$\hat{G} : \begin{bmatrix} \hat{x} \\ y \end{bmatrix} = \begin{bmatrix} \hat{A} & \hat{B} \\ \hat{C} & D \end{bmatrix} \begin{bmatrix} \hat{x} \\ u \end{bmatrix}, \quad (3.1)$$

where $\hat{A} \in \mathbb{R}^{n_x \times n_x}$, $\hat{B} \in \mathbb{R}^{n_x \times n_u}$, $\hat{C} \in \mathbb{R}^{n_y \times n_x}$, $D \in \mathbb{R}^{n_y \times n_u}$. In case $D = 0$, the LTI system \hat{G} is called *strictly proper*. Assuming that \hat{A} is diagonalizable, the real Jordan normal form of \hat{G} is given as

$$G : \begin{bmatrix} \dot{x}_1 \\ \vdots \\ \dot{x}_{n_i} \\ y \end{bmatrix} = \begin{bmatrix} A_1 & & 0 & B_1 \\ & \ddots & & \vdots \\ & & A_{n_i} & B_{n_i} \\ \hline C_1 & \dots & C_{n_i} & D \end{bmatrix} \begin{bmatrix} x_1 \\ \vdots \\ x_{n_i} \\ u \end{bmatrix}, \quad (3.2)$$

and can be computed according to [59] by applying a similarity transformation

$$\hat{x} = Tx = [T_1 \ \dots \ T_{n_i}] [x_1^T \ \dots \ x_{n_i}^T]^T. \quad (3.3)$$

In Equation (3.3), the transformation matrix T consists of the sub matrices T_i with $i = 1, \dots, n_i$, which are derived by carrying out an eigenvalue decomposition on \hat{A} . For a real eigenvalue p_i with a real eigenvector v_i ,

$$T_i = v_i \quad \text{and} \quad A_i = p_i. \quad (3.4)$$

For a conjugate complex pole pair $p_i = \Re(p_i) \pm j\Im(p_i)$ associated with the conjugate complex eigenvector pair $v_i = \Re(v_i) \pm j\Im(v_i)$,

$$T_i = [\Re(v_i) \ \Im(v_i)] \quad \text{and} \quad A_i = \begin{bmatrix} \Re(p_i) & \Im(p_i) \\ -\Im(p_i) & \Re(p_i) \end{bmatrix}. \quad (3.5)$$

Note that the eigenvectors v_i can be scaled arbitrarily, which does not affect A_i but changes the modal input and output matrices B_i and C_i , respectively. Based on the real Jordan normal form (3.2), the output

$$y = \sum_{i=1}^{n_i} y_i + Du$$

is a superposition of the direct feedthrough Du and the responses of the individual modes

$$M_i : \begin{bmatrix} \dot{x}_i \\ y_i \end{bmatrix} = \begin{bmatrix} A_i & B_i \\ C_i & 0 \end{bmatrix} \begin{bmatrix} x_i \\ u \end{bmatrix}. \quad (3.6)$$

This means that a mode M_i is a strictly proper LTI system of first (real pole) or second (conjugate complex pole pair) order and has n_u inputs and n_y outputs. Note that modes with a conjugate complex pole pair are also referred to as oscillating or dynamic modes since they describe a harmonic oscillator.

Alternatively, an LTI system may also be described by a transfer function matrix which is derived from its state space representation (3.1) as

$$\hat{G}(s) = \hat{C} (sI - \hat{A})^{-1} \hat{B} + D, \quad (3.7)$$

where s denotes the Laplace variable. Considering the individual mode M_i from Equation (3.6), its transfer function matrix is given as

$$M_i(s) = C_i(sI - A_i)^{-1} B_i = \begin{cases} \frac{R_1}{s - p_i} & \text{if } \Im(p_i) = 0 \\ \frac{R_1 s + R_0}{(s - p_i)(s - \bar{p}_i)} & \text{otherwise,} \end{cases} \quad (3.8)$$

where the coefficient matrices

$$R_0 = \det(A_i) C_i A_i^{-1} B_i, \quad (3.9)$$

$$R_1 = C_i B_i \quad (3.10)$$

are independent of the state space realization of M_i .

In general, a mode M_i is considered to be *asymptotically stable* if $\Re(p_i) < 0$ and *unstable* if $\Re(p_i) > 0$. In case $\Re(p_i) = 0$, the mode is considered to be *undamped*, which also includes a pole in the origin. Furthermore, the natural frequency of a mode is given as $\omega_{n,i} = |p_i|$ and for $\omega_{n,i} \neq 0$, the corresponding relative damping is $\zeta_i = -\Re(p_i)/\omega_{n,i}$. Note that the modes M_i are commonly sorted according to their natural frequency, i.e., $\omega_{n,1} \leq \omega_{n,2} \leq \dots \leq \omega_{n,n_i}$.

3.1.2 Modal Controllability and Observability

In general, the states of a dynamical system are considered as *controllable* if they can be steered from any initial value to any final value by choosing an appropriate input signal [75]. Similarly, a dynamical system is said to be *observable* if any initial state can be uniquely determined from the time history of the input and output signals. There are many different ways to evaluate controllability and observability of dynamical systems as reviewed, e.g., in [74, 148, 159]. Within this thesis, however, it is not the goal to evaluate an entire dynamical system but rather an individual targeted mode $M_i(s) = C_i(sI - A_i)^{-1} B_i$ defined in Equation (3.8). The mode $M_i(s)$ is considered as controllable if $B_i \neq 0$ and observable if $C_i \neq 0$, which directly results from common controllability and observability tests introduced, e.g., by Kálmán, Gilbert or Hautus [74]. Another test yielding the same conditions is based on the observability and controllability Gramian, which are defined as follows and need to be positive definite for all $T \in \mathbb{R}_{>0}$ to ensure controllability and observability [163].

Definition 3.1 (Controllability and Observability Gramian [148]). For a given asymptotically stable LTI system $G(s) = C(sI - A)^{-1} B + D$ the controllability Gramian is

$$W_c(T) = \int_0^T e^{At} B B^H e^{A^H t} dt \quad (3.11)$$

and the observability Gramian is

$$W_o(T) = \int_0^T e^{A^H t} C^H C e^{At} dt. \quad (3.12)$$

To further quantify the *grade* of controllability and observability, any p -norm $\|B_i\|_p$ and $\|C_i\|_p$ may be taken as a corresponding measure. Alternatively, [55]

proposes to measure the angle between the left or right Eigenvector of A_i and the columns of B_i or the rows of C_i , respectively. Other approaches are based on the singular or eigenvalues of the observability and controllability Gramians as proposed in, e.g., [54, 105]. However, all these quantification methods introduce a dependency on the state space realization of $M_i(s)$, which is generally not desired but the case when examining observability and controllability independently of each other. Hence, it may be recommended to evaluate controllability and observability in a joint manner. A well-known measure of this type is proposed by Litz [89].

Definition 3.2 (Litz dominance measure [89]). The Litz dominance measure is

$$q_{jkl} = \frac{|r_{jkl}|}{|p_k|}, \quad (3.13)$$

where $r_{jkl} \in \mathbb{C}$ denotes the residue from the j^{th} input to the l^{th} output associated to the pole $p_k \in \mathbb{C}$, $k = 1, \dots, n_x$ of a diagonalizable LTI system of order n_x .

The Litz dominance measure is based on an approximation of the step response but can also be interpreted in terms of the sensitivity of p_k with respect to the static feedback gain connecting the l^{th} output with the j^{th} input. This makes the measure well suitable for selecting dominant poles [90] as well as for optimally placing actuators and sensors [14]. Another well-established measure invariant to state space transformations are the Hankel singular values, which are defined as follows.

Definition 3.3 (Hankel singular values [148]). The Hankel singular values of an asymptotically stable LTI system are

$$\sigma_{H,k} = \sqrt{\lambda_k(\bar{W}_c \bar{W}_o)}, \quad (3.14)$$

where $\lambda_k(\bar{W}_c \bar{W}_o)$ denotes the k^{th} eigenvalue of the product of the controllability and observability Gramians $\bar{W}_c = \lim_{T \rightarrow \infty} W_c(T)$ and $\bar{W}_o = \lim_{T \rightarrow \infty} W_o(T)$.

The Hankel singular values provide a useful measure of the energy contribution of each state variable to the input-output behavior in so-called balanced state space realizations. Hence, the Hankel singular values serve as a basis for the well-known balanced model order reduction where states with a small energy contribution are discarded, see, e.g., [105, 119]. Note that to obtain a single gross measure from the set of Litz dominance measures (3.13) or Hankel singular values (3.14), some sum or maximum value is generally taken, see, e.g., [46, 48, 56, 89, 105].

In addition to this, also system norms such as the Hankel, \mathcal{H}_∞ or \mathcal{H}_2 norm are well suited for jointly evaluating modal controllability and observability, see

e.g., [47]. The main reason for this are the meaningful physical interpretations of the different system norms. For instance, the Hankel system norm, defined as the largest Hankel singular value, can be seen as a kind of induced norm from past inputs to future outputs as the following definition reveals.

Definition 3.4 (Hankel norm [148]). The Hankel norm of an asymptotically stable LTI system $G(s)$ with inputs u and outputs y is

$$\|G(s)\|_{\text{H}} = \max_k \sigma_{\text{H},k} = \max_{u(t) \neq 0} \frac{\sqrt{\int_0^\infty \|y(\tau)\|_2^2 d\tau}}{\sqrt{\int_{-\infty}^0 \|u(\tau)\|_2^2 d\tau}}. \quad (3.15)$$

In contrast, the \mathcal{H}_∞ norm describes the “worst-case” steady state gain for sinusoidal inputs at any frequency, which is equivalent to the induced \mathcal{L}_2 or power norm.

Definition 3.5 (\mathcal{H}_∞ norm [148]). The \mathcal{H}_∞ norm of an asymptotically stable LTI system $G(s)$ with inputs u and outputs y , and zero initial states is

$$\|G(s)\|_{\mathcal{H}_\infty} = \max_{\omega \in \mathbb{R}} \sigma_{\max}(G(j\omega)) = \max_{u(t) \neq 0} \frac{\|y(t)\|_2}{\|u(t)\|_2}, \quad (3.16)$$

where $\sigma_{\max}(G(j\omega))$ denotes the maximum singular value of the frequency response $G(j\omega)$.

Considering the \mathcal{H}_2 norm, it can be seen as the square root of the sum of output energies when applying unit impulses to each individual input as seen in Definition 3.6. Moreover, the \mathcal{H}_2 norm describes the expected root mean square value of the system output in response to white Gaussian noise excitation [148]. And in case of SISO systems, it can be also be interpreted as the maximum possible output value when the energy of the input signal is bounded to one, i.e., the maximum energy-to-peak gain [80].

Definition 3.6 (\mathcal{H}_2 norm [148]). The \mathcal{H}_2 norm of an asymptotically stable, strictly proper LTI system $G(s)$ with zero initial states is

$$\|G(s)\|_{\mathcal{H}_2} = \sqrt{\int_0^\infty \|H(t)\|_{\text{F}}^2 dt} = \sqrt{\frac{1}{2\pi} \int_{-\infty}^\infty \|G(j\omega)\|_{\text{F}}^2 d\omega}, \quad (3.17)$$

where $\|\bullet\|_{\text{F}}$ denotes the Frobenius norm and $H(t)$ denotes the impulse response matrix of $G(s)$.

In Section 3.2, the \mathcal{H}_2 norm is selected for jointly evaluating modal controllability and observability. Its close relation to the other measures given here is qualitatively discussed in Section 3.2.4 and quantitatively demonstrated by means of a numerical example in Section 3.3.5. Note that the \mathcal{H}_2 norm, just as the Hankel and \mathcal{H}_∞ norm, is only defined for asymptotically stable systems, but can be generalized also for unstable systems as described in Section 3.2.4.

3.1.3 Modal Control using Blended Inputs and Outputs

The modal control approach followed in this thesis aims at separately controlling individual targeted modes $\{M_j(s)\}_{j=1}^{n_j} \subset \{M_i(s)\}_{i=1}^{n_i}$. To that end, each targeted mode j is isolated by blending control inputs and measurement outputs in order to enable controlling it by a simple SISO controller. Hence, the blending-based control law from Equation (2.1) can be seen as a superposition of the individual modal controllers

$$K_j(s) = k_{u,j} \lambda_j(s) k_{y,j}^T, \quad (3.18)$$

with the SISO controller $\lambda_j(s)$, and the input and output blending vectors $k_{u,j} \in \mathbb{R}^{n_u}$ and $k_{y,j} \in \mathbb{R}^{n_y}$, respectively. The overall feedback controller is thus given as

$$K(s) = K_u \Lambda(s) K_y^T = \sum_{j=1}^{n_j} K_j(s), \quad (3.19)$$

where the input and output blending vectors of all modal controllers are collected as columns in the input and output blending matrices $K_u \in \mathbb{R}^{n_u \times n_j}$ and $K_y \in \mathbb{R}^{n_y \times n_j}$, and the respective SISO controllers are collected on the diagonal of the simplified control law

$$\Lambda(s) = \begin{bmatrix} \lambda_1(s) & \cdots & 0 \\ \vdots & \ddots & \vdots \\ 0 & \cdots & \lambda_{n_j}(s) \end{bmatrix}. \quad (3.20)$$

In this way, the original MIMO control design problem is reduced to multiple SISO ones, which can be solved independently in case the targeted modes can be sufficiently isolated through the input and output blending. The overall controller structure is depicted in Figure 3.1, where the focus of this thesis is put on the design of the corresponding input and output blending vectors. In what follows, remarks on SISO controller design and handling of direct feedthrough are given before developing the corresponding blending vector design strategies.

Remarks on SISO Controller Design

In order to enable an independent design of the SISO controllers $\lambda_j(s)$, it is generally required that the targeted mode is sufficiently isolated from the rest of the system dynamics. To achieve that, it is primarily proposed to apply spillover suppression techniques described in detail in Section 3.4. If the required mode isolation is possible, the performance of an individual SISO controller is not

affected when closing all SISO loops, since the individual loops do not interact. As a result, the design of the respective SISO controllers can be performed independently of each other.

In case the desired mode isolation cannot be achieved, the individual SISO loops interact and an independent SISO controller design may not yield the desired overall performance. This can be the case when the frequency separation of the considered modes is too small or the number of measurements or effectors is insufficient. As a remedy, a sequential loop closing can be applied [40, 65, 99], which can be seen as a cascaded controller design. This means that each loop is directly closed after designing a controller K_j and the resulting system with the partially closed loops is used as a basis for designing the next controller K_{j+1} . Thereby, a repeated modal decomposition needs to be carried out after each loop closure since the next mode to be controlled may have been affected by the already closed loops. Alternatively, the blending vectors may be computed only once for the original system and only the SISO loops may be closed in a sequential way. This avoids a repeated modal decomposition but is only recommended in case of a minor interaction between the individual SISO loops. Furthermore, it is noted that the order in which the loops are closed introduces an additional degree of freedom for the control engineer and may also affect overall controller performance.

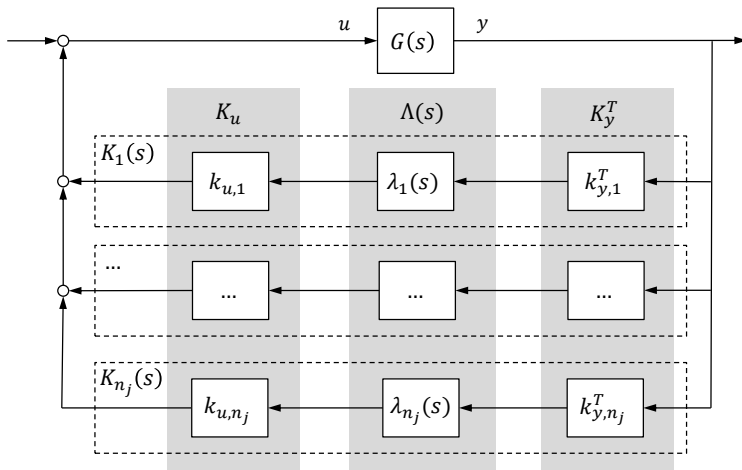


Figure 3.1: Blending-based modal feedback controller where each $K_j(s)$ controls a mode $M_j(s)$ with $j = 1, \dots, n_j$.

Remarks on Direct Feedthrough

In general, mechanical systems feature a roll-off at higher frequencies, i.e., the feedthrough matrix $D \in \mathbb{R}^{n_y \times n_u}$ is zero. If this is not the case, the feedthrough term needs to be eliminated for the proposed blending-based modal control approach. This can be achieved by introducing a new measurement output $\tilde{y} = y - Du$, where y denotes the original measurements and u the control commands computed by the controller. However, note that this requires well-posedness, i.e., that $I + D_K D$ is invertible, where $D_K \in \mathbb{R}^{n_u \times n_y}$ denotes the feedthrough matrix of the controller derived using the measurements \tilde{y} .

Alternatively, the feedthrough matrix D may also be eliminated by designing the input and output blending vectors k_u and k_y in a way such that $k_y^T D k_u^T = 0$. A corresponding procedure is proposed in Section 3.4.2 allowing for considering orthogonality constraints during blending vector design. Note that the procedure is mainly proposed for explicitly decoupling the targeted mode from residual modes, but it is also useful for eliminating direct feedthrough.

3.2 \mathcal{H}_2 -optimal Blending of Inputs and Outputs

In general, the blending of inputs and outputs decreases, or, in a best-case, maintains the controllability and observability of the underlying system and hence its modes. Consequently, a goal for blending vector design is a minimum reduction in controllability and observability, which can be measured in a joint way by means of the \mathcal{H}_2 norm as discussed in Section 3.1.2. In what follows, a new method is developed for efficiently computing blending vectors which yield a maximum \mathcal{H}_2 norm when applied to the mode to be controlled. The blending method is further extended to undamped and unstable modes, for which the \mathcal{H}_2 norm is not defined. Additionally, the connection of \mathcal{H}_2 -optimality to other controllability and observability measures is discussed. Note that although the approach is derived for a single mode, it is easily extended to higher-order systems where multiple modes need to be controlled as described in Section 3.1.3. The properties of the proposed \mathcal{H}_2 -optimal blending approach are demonstrated by means of two numerical examples in Section 3.2.6 and its effectiveness is shown based on three realistic aeronautical applications in Chapter 5.

3.2.1 Problem Definition

To describe the efficiency of a pair of blending vectors designed for controlling an individual mode, the following measure is used.

Definition 3.7 (Blending vector efficiency for asymptotically stable mode). Let the asymptotically stable mode $M(s)$ be given and feature n_u inputs and n_y outputs. Furthermore, let $M(s)$ be controllable and observable, which means that $\|M(s)\|_{\mathcal{H}_2} > 0$. Then, the blending vector efficiency of a pair of input and output blending vectors $k_u \in \mathbb{R}^{n_u}$, $\|k_u\|_2 = 1$ and $k_y \in \mathbb{R}^{n_y}$, $\|k_y\|_2 = 1$ for controlling $M(s)$ is

$$\eta = \frac{\|k_y^T M(s) k_u\|_{\mathcal{H}_2}}{\|M(s)\|_{\mathcal{H}_2}}. \quad (3.21)$$

From Definition 3.7, it can be seen that $\eta \in [0, 1]$, where $\eta = 0$ indicates that the blended mode $k_y^T M(s) k_u$ is not controllable, not observable or both. In contrast, $\eta = 1$ means that the blending of inputs and outputs does not affect the controllability and observability of the targeted mode. Hence, the goal for blending vector design is to maximize η , or, the \mathcal{H}_2 norm of the blended mode. The resulting optimization problem can thus be formulated as

$$\begin{aligned} & \underset{k_u \in \mathbb{R}^{n_u}, k_y \in \mathbb{R}^{n_y}}{\text{maximize}} && \|k_y^T M(s) k_u\|_{\mathcal{H}_2} \\ & \text{subject to} && \|k_u\|_2 = 1 \\ & && \|k_y\|_2 = 1. \end{aligned} \quad (3.22)$$

Blending vectors which solve the optimization problem (3.22) are considered as \mathcal{H}_2 -optimal and are derived in an efficient way as follows.

3.2.2 Efficient \mathcal{H}_2 Norm Computation

In order to solve the blending vector design problem (3.22), the \mathcal{H}_2 norm needs to be computed. This is generally performed in a numerically efficient way using the following theorem, which is based on the definition of the \mathcal{H}_2 norm given in Equation (3.17).

Theorem 3.1 (Gramian-based \mathcal{H}_2 norm computation, [169]). *For an asymptotically stable and strictly proper LTI system G with a state space representation $\dot{x} = Ax + Bu$, $y = Cx$, the \mathcal{H}_2 norm is*

$$\|G\|_{\mathcal{H}_2} = \sqrt{\text{tr}[C\bar{W}_c C^H]} = \sqrt{\text{tr}[B^H \bar{W}_o B]}, \quad (3.23)$$

where the controllability and observability Gramian \bar{W}_c and \bar{W}_o are obtained by solving the Lyapunov equations

$$A\bar{W}_c + \bar{W}_c A^H + BB^H = 0, \quad (3.24)$$

$$A^H \bar{W}_o + \bar{W}_o A + C^H C = 0. \quad (3.25)$$

Proof. The proof is taken from [169] and summarized as follows. Since G is asymptotically stable, the impulse response matrix is given as

$$H(t) = \begin{cases} Ce^{At}B & t \geq 0 \\ 0 & t < 0 \end{cases},$$

which yields when substituted into Equation (3.17)

$$\begin{aligned} \|G\|_{\mathcal{H}_2}^2 &= \int_0^\infty \text{tr}[H(t)H(t)^H] dt = \int_0^\infty \text{tr}[H(t)^H H(t)] dt \\ &= \int_0^\infty \text{tr}[Ce^{At}BB^H e^{A^H t}C^H] dt = \int_0^\infty \text{tr}[B^H e^{A^H t}C^H Ce^{At}B] dt. \end{aligned}$$

The theorem follows from the fact that the controllability and observability Gramian obtained from Equations (3.24) and (3.25) can also be represented as

$$\bar{W}_c = \int_0^\infty e^{At}BB^H e^{A^H t} dt,$$

$$\bar{W}_o = \int_0^\infty e^{A^H t}C^H Ce^{At} dt. \quad \square$$

In case of first- or second-order systems, the \mathcal{H}_2 norm can also be computed in a more direct way as given by the following theorem. Note that the theorem is especially developed for \mathcal{H}_2 -optimal blending vector design but may also be useful for other applications.

Theorem 3.2 (\mathcal{H}_2 norm of first- or second-order LTI systems). *Let the transfer function matrix $M : \mathbb{C} \rightarrow \mathbb{C}^{n_y \times n_u}$ be given and describe a strictly proper and asymptotically stable LTI system of first or second order. Furthermore, let ω_n and ζ denote the natural frequency and relative damping of M . Then, the \mathcal{H}_2 norm of M is*

$$\|M\|_{\mathcal{H}_2} = \sqrt{\zeta \omega_n} \|M(j\omega_n)\|_{\mathbb{F}}, \quad (3.26)$$

where $\|\bullet\|_{\mathbb{F}}$ denotes the Frobenius norm.

Proof. The proof is derived for the more general case of an LTI system with a single conjugate complex pole pair. For systems with real-valued poles, the proof follows the same procedure and is not given here.

To begin with, the strictly proper transfer function from input $j \in \{1, 2, \dots, n_u\}$ to output $i \in \{1, 2, \dots, n_y\}$

$$m_{ij}(s) = \frac{r}{s-p} + \frac{\bar{r}}{s-\bar{p}} = c(sI - A)^{-1}b$$

is realized in state space by choosing

$$A = \begin{bmatrix} p & 0 \\ 0 & \bar{p} \end{bmatrix}, b = \begin{bmatrix} 1 \\ 1 \end{bmatrix}, c = [r \quad \bar{r}],$$

where r and \bar{r} denote the conjugate complex (scalar) residues associated to the conjugate complex pole pair p and \bar{p} . By analytically solving the Lyapunov equation (3.24), the corresponding controllability Gramian is computed as

$$\bar{W}_c = - \begin{bmatrix} \frac{1}{p+\bar{p}} & \frac{1}{2p} \\ \frac{1}{2\bar{p}} & \frac{1}{p+\bar{p}} \end{bmatrix}.$$

Based on this, the squared \mathcal{H}_2 norm of m_{ij} is computed according to Theorem 3.1 as

$$\|m_{ij}\|_{\mathcal{H}_2}^2 = c \bar{W}_c c^H = \frac{4p\bar{p}r\bar{r} + (r^2\bar{p} + \bar{r}^2p)(p + \bar{p})}{-2p\bar{p}(p + \bar{p})}. \quad (3.27)$$

The same result is obtained by computing the square of Equation (3.26) as

$$\begin{aligned} \|m_{ij}\|_{\mathcal{H}_2}^2 &= \omega_n \zeta \|m_{ij}(j\omega_n)\|_{\mathbb{F}}^2 = -\frac{1}{2}(p + \bar{p}) |m_{ij}(j\sqrt{p\bar{p}})|^2 \\ &= \frac{4p\bar{p}r\bar{r} + (r^2\bar{p} + \bar{r}^2p)(p + \bar{p})}{-2p\bar{p}(p + \bar{p})}. \end{aligned}$$

Eventually, it follows from the definition of the \mathcal{H}_2 norm given in Equation (3.17) that

$$\|M\|_{\mathcal{H}_2}^2 = \sum_{i=1}^{n_y} \sum_{j=1}^{n_u} \|m_{ij}\|_{\mathcal{H}_2}^2,$$

since the squared Frobenius norm of a matrix is defined as the sum of the squared magnitudes of its elements. \square

Remark 3.1. The natural frequency ω_n and relative damping ζ for a system with a single real pole or a conjugate complex pole pair are defined in Section 3.1.1. Considering an asymptotically stable system with two real-valued poles $p_1 < 0$ and $p_2 < 0$, it can be seen as an overdamped system with $\omega_n = \sqrt{p_1 p_2}$ and $\zeta = -\frac{p_1 + p_2}{2\omega_n} \geq 1$.

Remark 3.2. In case M features only a single input and a single output, Equation (3.26) reduces to $\|M\|_{\mathcal{H}_2} = \sqrt{\zeta\omega_n} |M(j\omega_n)|$.

3.2.3 Efficient Blending Vector Computation

Based on Theorem 3.2, the objective function of the blending vector design problem (3.22) can be reformulated as

$$\|k_y^T M(s) k_u\|_{\mathcal{H}_2} = \sqrt{\zeta\omega_n} |k_y^T M(j\omega_n) k_u|, \quad (3.28)$$

where $M(j\omega_n)$ denotes the frequency response of $M(s)$ at its natural frequency ω_n . Since the term $\sqrt{\zeta\omega_n}$ is actually independent of the blending vectors, the original problem of maximizing the \mathcal{H}_2 norm in (3.22) can be turned into a problem of maximizing the magnitude of the complex scalar $z = k_y^T M(j\omega_n) k_u$. In what follows, a rather uncommon way for computing the magnitude of a complex number is given allowing for an efficient blending vector design.

Proposition 3.1 (Magnitude of a complex number). *Let $z \in \mathbb{C}$ be given and the corresponding real and imaginary part be denoted as $\Re(z)$ and $\Im(z)$, respectively. Then,*

$$|z| = \max_{\phi \in \mathbb{R}} (\Re(z) \cos \phi + \Im(z) \sin \phi). \quad (3.29)$$

Proof. The extrema of

$$f(\phi) = \Re(z) \cos \phi + \Im(z) \sin \phi \quad (3.30)$$

can be computed by finding the roots of its derivative $\partial f(\phi)/\partial \phi$. Selecting only the roots $\phi^* = \arg z$ which are associated to maxima, and substituting $\Re(z) = |z| \cos \phi^*$ and $\Im(z) = |z| \sin \phi^*$ into Equation (3.30), it follows

$$f(\phi^*) = |z| \cos^2 \phi^* + |z| \sin^2 \phi^* = |z|. \quad \square$$

Remark 3.3. The intuition behind Proposition 3.1 is that the magnitude of a complex number can be directly read by rotating it onto the positive real axis in the complex plane. See [123] for more details.

Computing the magnitude of $z = k_y^T M(j\omega_n) k_u$ according to Proposition 3.1 and factoring out the real-valued blending vectors k_y and k_u , it is derived that

$$|k_y^T M(j\omega_n) k_u| = \max_{\phi} (k_y^T F(\phi) k_u), \quad (3.31)$$

where $F(\phi) : \mathbb{R} \rightarrow \mathbb{R}^{n_y \times n_u}$ is defined as

$$F(\phi) = \Re(M(j\omega_n)) \cos \phi + \Im(M(j\omega_n)) \sin \phi. \quad (3.32)$$

Recalling that the actual goal is to find a maximum of Equation (3.31) gives

$$\begin{aligned} \max_{k_u, k_y} |k_y^T M(j\omega_n) k_u| &= \max_{k_u, k_y} \max_{\phi} (k_y^T F(\phi) k_u) \\ &= \max_{\phi} \max_{k_u, k_y} (k_y^T F(\phi) k_u). \end{aligned} \quad (3.33)$$

With $\|k_u\|_2 = \|k_y\|_2 = 1$, it follows that

$$\max_{k_u, k_y} (k_y^T F(\phi) k_u) = \|F(\phi)\|_2 = \sigma^*, \quad (3.34)$$

which can be directly computed for a given value of ϕ by applying an SVD on

$$F(\phi) = U \Sigma V^T = \begin{bmatrix} k_y^* & \bullet \\ 0 & \bullet \end{bmatrix} \begin{bmatrix} \sigma^* & 0 \\ 0 & \bullet \end{bmatrix} \begin{bmatrix} k_u^* & \bullet \end{bmatrix}^T, \quad (3.35)$$

where the placeholder \bullet denotes a matrix of adequate size. In Equation (3.35), both $U \in \mathbb{R}^{n_y \times n_y}$ and $V \in \mathbb{R}^{n_u \times n_u}$ are orthogonal matrices which are real-valued since $F(\phi)$ is also real-valued. Furthermore, $\Sigma \in \mathbb{R}^{n_y \times n_u}$ is a rectangular matrix with the singular values of $F(\phi)$ in descending order on its diagonal. Selecting only the largest singular value $\sigma^* \in \mathbb{R}_{\geq 0}$, the corresponding input and output singular vectors $k_u^* \in \mathbb{R}^{n_u}$ and $k_y^* \in \mathbb{R}^{n_y}$ directly yield the input and output blending vectors which solve Equation (3.34) for a given value of ϕ .

Eventually, inserting Equation (3.34) into Equation (3.33), an equivalent formulation of the optimization problem (3.22) is derived as

$$\begin{aligned} \max_{k_u, k_y} \quad & \|k_y^T M(s) k_u\|_{\mathcal{H}_2} \\ \text{s.t.} \quad & \|k_u\|_2 = \|k_y\|_2 = 1 \end{aligned} \quad \Leftrightarrow \quad \max_{\phi} \|F(\phi)\|_2 \sqrt{\zeta \omega_n}, \quad (3.36)$$

where it is emphasized that $\phi \in \mathbb{R}$ is unconstrained while $k_u \in \mathbb{R}^{n_u}$ and $k_y \in \mathbb{R}^{n_y}$ are constrained. Solving $\max_{\phi} \|F(\phi)\|_2$ yields an optimal phase angle ϕ^* for which the \mathcal{H}_2 -optimal blending vectors can be directly determined according to Equation (3.35). Hence, the number of optimization variables is reduced from $n_u + n_y$ to a single one, or, in other words, the difficulty of finding a solution to Equation (3.22) becomes independent of the number of actual inputs and outputs.

3.2.4 Special Cases and Additional Aspects

This subsection discusses special cases and additional aspects of the proposed \mathcal{H}_2 -optimal blending method that either simplify the computation of the blending vectors or are of conceptual interest.

Reduction of Computational Effort

Considering the original blending vector design problem (3.22), its solution according to Equation (3.36) requires to carry out an SVD on $F(\phi)$ for each iteration of ϕ . The computational cost of a single SVD largely depends on the size of $F(\phi)$, which is given by the number of inputs and outputs of the underlying system. Hence, if the underlying system has a large number of inputs and outputs, the computational effort to solve (3.36) may be high and lack numerical accuracy. For this reason, it is suggested to previously decompose the targeted mode as

$$M(s) = C(sI - A)^{-1}B = Q_C \underbrace{R_C(sI - A)^{-1}R_B^T}_{\tilde{M}(s)} Q_B^T, \quad (3.37)$$

where both $Q_C \in \mathbb{R}^{n_y \times n_{\tilde{y}}}$ and $Q_B \in \mathbb{R}^{n_u \times n_{\tilde{u}}}$ form orthonormal bases, and $\tilde{M}(s)$ describes a transfer function matrix with $n_{\tilde{u}} \leq 2$ inputs and $n_{\tilde{y}} \leq 2$ outputs. To that end, $B^T = Q_B R_B$ and $C = Q_C R_C$ from a minimal realization $\{A, B, C\}$ of $M(s)$ are decomposed using, e.g., a thin QR decomposition. See Appendix A.1 for more details.

From Equation (3.37) it follows that $\|M(j\omega_n)\|_2 = \|\tilde{M}(j\omega_n)\|_2$ since Q_B and Q_C act as unitary transformations. This allows reformulating Equation (3.36) as

$$\max_{k_u, k_y} \|k_y^T M(s) k_u\|_{\mathcal{H}_2} = \sqrt{\zeta \omega_n} \max_{\phi} \|\tilde{F}(\phi)\|_2, \quad (3.38)$$

where $\tilde{F}(\phi) : \mathbb{R} \rightarrow \mathbb{R}^{n_{\tilde{y}} \times n_{\tilde{u}}}$ is defined as

$$\tilde{F}(\phi) = \Re(\tilde{M}(j\omega_n)) \cos \phi + \Im(\tilde{M}(j\omega_n)) \sin \phi. \quad (3.39)$$

As the matrix returned by $\tilde{F}(\phi)$ has a maximum size of 2×2 , the term $\|\tilde{F}(\phi)\|_2$ and also its derivative $\partial \|\tilde{F}(\phi)\|_2 / \partial \phi$ can be computed analytically as given, e.g., in [148]. For optimization, this means that computational effort and numerical inaccuracy can be greatly reduced, especially when the given number of inputs and outputs is high. Note that if the real or imaginary part of $M(j\omega_n)$ is zero, the \mathcal{H}_2 -optimal blending vectors can be computed without the need of solving optimization problem (3.36), which makes the proposed decomposition unnecessary for this special case.

Scaling of Inputs and Outputs

In general, the proposed \mathcal{H}_2 -optimal blending is sensitive to the scaling of inputs and outputs. This means that an appropriate scaling of the system's inputs and outputs is crucial in order to obtain meaningful blending vectors since different signals with possibly different physical units are united in a single one. Hence, it is proposed to group the respective signals according to their physical units and to scale them in groups. This allows for normalizing different physical units among one another while maintaining the relative importance of individual signals. In comparison, scaling each signal with the corresponding maximum value as proposed, e.g., in [148], may lead to a loss of information and an undesirable prioritization of individual signals. To demonstrate this, an example is given in Section 3.2.6. Furthermore, it is noted that a targeted scaling may also be used as a tuning possibility for blending vector design.

Single Real-valued Pole

In case the targeted mode $M(s)$ features only a single real-valued pole $p \in \mathbb{R}$, i.e., $M(s) = c(s - p)^{-1}b^T$, it follows from Theorem 3.2 that

$$\max_{k_u, k_y} \|k_y^T M(s) k_u\|_{\mathcal{H}_2} = \sqrt{\zeta \omega_n} \max_{k_u, k_y} |k_y^T c b^T k_u|, \quad (3.40)$$

where $\|k_u\|_2 = \|k_y\|_2 = 1$. Based on that, the \mathcal{H}_2 -optimal blending vectors which solve Equation (3.40) are directly given as

$$k_u^* = \frac{b}{\|b\|_2} \quad \text{and} \quad k_y^* = \frac{c}{\|c\|_2},$$

where $b \in \mathbb{R}^{n_u}$ and $c \in \mathbb{R}^{n_y}$.

Undamped Poles

According to Section 3.1.1, a mode $M(s)$ with a real pole p or a conjugate complex pole pair p and \bar{p} is considered undamped if $\Re(p) = 0$. Since the \mathcal{H}_2 norm of $M(s)$ is not defined in this case, it is suggested to use the following proposition for blending vector computation.

Proposition 3.2 (Blending vector efficiency factor for undamped modes). *Let an oscillating mode be given as $M(s) = \frac{R}{s-p} + \frac{\bar{R}}{s-\bar{p}}$, where $R \in \mathbb{C}^{n_y \times n_u}$ and $\bar{R} \in \mathbb{C}^{n_y \times n_u}$ denote the conjugate complex residues associated to the conjugate complex pole pair $p \in \mathbb{C}$ and $\bar{p} \in \mathbb{C}$. Then, for a given pair of input and output blending vectors $k_u \in \mathbb{R}^{n_u}$ and $k_y \in \mathbb{R}^{n_y}$ with $\|k_y\|_2 = \|k_u\|_2 = 1$, the limit of*

the blending vector efficiency factor for $\Re(p) \rightarrow 0^-$ is given as

$$\eta_{\text{lim}} = \lim_{\Re(p) \rightarrow 0^-} \eta = \frac{|k_y^T R k_u|}{\|R\|_{\text{F}}}, \quad (3.41)$$

where $\|R\|_{\text{F}} = \sqrt{\text{tr}(RR^H)}$ denotes the Forbenius norm of R .

Proof. Taking the definition of the blending vector efficiency η from Equation (3.21) and computing the \mathcal{H}_2 norm according to Theorem 3.2, it can be written

$$\eta = \frac{\|k_y^T M(s) k_u\|_{\mathcal{H}_2}}{\|M(s)\|_{\mathcal{H}_2}} = \frac{\sqrt{\zeta\omega_n} \|k_y^T M(j\omega_n) k_u\|_{\text{F}}}{\sqrt{\zeta\omega_n} \|M(j\omega_n)\|_{\text{F}}}. \quad (3.42)$$

Substituting the frequency response

$$M(j\omega_n) = \frac{R}{j\omega_n - p} + \frac{\bar{R}}{j\omega_n - \bar{p}} = \frac{R(j\omega_n - \bar{p}) + \bar{R}(j\omega_n - p)}{(j\omega_n - p)(j\omega_n - \bar{p})}$$

into the right hand side of Equation (3.42) yields then

$$\eta = \frac{\|k_y^T (R(j\omega_n - \bar{p}) + \bar{R}(j\omega_n - p)) k_u\|_{\text{F}}}{\|R(j\omega_n - \bar{p}) + \bar{R}(j\omega_n - p)\|_{\text{F}}}.$$

Assuming without loss of generality that $\Im(p) \geq 0$, it follows for $\Re(p) \rightarrow 0^-$ that $p \rightarrow j\omega_n$ and $\bar{p} \rightarrow -j\omega_n$, which yields

$$\lim_{\Re(p) \rightarrow 0^-} \eta = \frac{|k_y^T R k_u|}{\|R\|_{\text{F}}} = \frac{|k_y^T \bar{R} k_u|}{\|\bar{R}\|_{\text{F}}}.$$

□

Based on Proposition 3.2, the matrix function $F(\phi)$ defined in Equation (3.32) can be replaced by

$$F_{\text{lim}}(\phi) = \Re(R) \cos \phi + \Im(R) \sin \phi.$$

Equally, the matrix function $\tilde{F}(\phi)$ defined in Equation (3.39) can be replaced by

$$\tilde{F}_{\text{lim}}(\phi) = \Re(\tilde{R}) \cos \phi + \Im(\tilde{R}) \sin \phi,$$

where \tilde{R} denotes the residue of the decomposed mode $\tilde{M}(s)$ from Equation (3.37). The \mathcal{H}_2 -optimal blending vectors can then be derived by first computing $\phi^* = \arg \max_{\phi} \|\tilde{F}_{\text{lim}}(\phi)\|_2$ and subsequently computing the singular vectors of $\tilde{F}_{\text{lim}}(\phi^*)$ similarly to Equation (3.35). Furthermore, it is noted that maximizing η_{lim} is equivalent to maximizing the Litzz dominance measure [89]. This can be directly seen from Definition 3.2 and is also discussed at the end of Section 3.2.4.

Unstable Poles

Similarly to an undamped mode, the \mathcal{H}_2 norm of an unstable mode with $\Re(p) > 0$ is also not defined. Taking the frequency domain definition of the \mathcal{H}_2 norm from Equation (3.17), it can be seen that the \mathcal{H}_2 norm becomes a maximum if and only if the integral over the (squared) magnitude of the frequency response becomes a maximum. For an unstable mode, this integral can also be computed by exploiting the fact that the magnitude is not affected when mirroring the unstable pole(s) across the imaginary axis. As a result, an asymptotically stable system is obtained for which the \mathcal{H}_2 norm can be computed as given in Section 3.2.2. Based on that, it is proposed to design the blending vectors of an unstable mode by first mirroring the underlying poles across the imaginary axis and then applying the algorithm described above.

Single-Input or Single-Output Systems

For systems with a single input *or* a single output, the blending vector design is restricted to only outputs or only inputs, respectively. Considering the case where only inputs of an oscillating mode $M(s)$ are blended, the \mathcal{H}_2 -optimal blending vector design problem (3.22) reduces to

$$\underset{k_u \in \mathbb{R}^{n_u}}{\text{maximize}} \quad \|M(s)k_u\|_{\mathcal{H}_2} \quad \text{subject to} \quad \|k_u\|_2 = 1. \quad (3.43)$$

To solve optimization problem (3.43), Theorem 3.2 is first reformulated as

$$\|M(s)k_u\|_{\mathcal{H}_2} = \sqrt{\omega_n \zeta} |M(j\omega_n)k_u| = \sqrt{\omega_n \zeta} \left| \begin{bmatrix} \Re(M(j\omega_n)) \\ \Im(M(j\omega_n)) \end{bmatrix} k_u \right|.$$

Then, the \mathcal{H}_2 -optimal input blending vector $k_{u,\text{in}}^*$ is directly derived by carrying out a SVD on

$$F_{\text{in}} = \begin{bmatrix} \Re(M(j\omega_n)) \\ \Im(M(j\omega_n)) \end{bmatrix} = U\Sigma V^T = \begin{bmatrix} \bullet & \bullet \\ 0 & \bullet \end{bmatrix} \begin{bmatrix} \sigma_{\text{in}}^* & 0 \\ 0 & \bullet \end{bmatrix} \begin{bmatrix} k_{u,\text{in}}^* & \bullet \end{bmatrix}^T, \quad (3.44)$$

where $\sigma_{\text{in}}^* = \|F_{\text{in}}\|_2$ denotes the maximum singular value of F_{in} . Similarly, the \mathcal{H}_2 -optimal output blending vector $k_{y,\text{out}}^*$ for a single-input system is derived by carrying out a SVD on

$$F_{\text{out}} = \begin{bmatrix} \Re(M(j\omega_n)) & \Im(M(j\omega_n)) \end{bmatrix} = U\Sigma V^T = \begin{bmatrix} k_{y,\text{out}}^* & \bullet \\ 0 & \bullet \end{bmatrix} \begin{bmatrix} \sigma_{\text{out}}^* & 0 \\ 0 & \bullet \end{bmatrix} \begin{bmatrix} \bullet & \bullet \end{bmatrix}^T, \quad (3.45)$$

where $\sigma_{\text{out}}^* = \|F_{\text{out}}\|_2$ denotes the maximum singular value of F_{out} . Note that the given procedure also applies to MIMO systems where only inputs or only outputs are subject to blending. However, independently deriving pair of input and

output blending vectors in this way does not guarantee \mathcal{H}_2 -optimality applying both vectors together. This is demonstrated in the numerical example given in Section 3.2.6.

Relation to Other Controllability and Observability Measures

The proposed blending approach maximizes the \mathcal{H}_2 norm of the blended mode as a measure of its controllability and observability. In this subsection, the relation of the \mathcal{H}_2 norm measure to the other modal controllability and observability measures reviewed in Section 3.1.2 is discussed, where first- and second-order modes are viewed separately.

Considering a *first-order* mode, it is given according to Equation (3.8) as $M(s) = R/(s-p)$, where the residue $R \in \mathbb{R}^{n_y \times n_u}$ and the pole $p \in \mathbb{R}$. A pair of input and output blending vectors k_u and k_y which maximizes the \mathcal{H}_2 norm of the blended first order mode also maximizes any other system norm of it. This becomes clear when writing

$$\|k_y^T M(s) k_u\| = |k_y^T R k_u| \left\| \frac{1}{s-p} \right\|, \quad (3.46)$$

where $\|\bullet\|$ denotes any system norm such as the Hankel, \mathcal{H}_∞ or \mathcal{H}_2 norm. Equation (3.46) further reveals that \mathcal{H}_2 -optimal blending vectors also maximize the Litz dominance measure [89], which is given as $d = |k_y^T R k_u|/|p|$, see also Definition 3.2.

Similar relations can be found for a *second-order* mode $M(s) = R/(s+p) + \bar{R}/(s+\bar{p})$, which is described by the conjugate complex pole pair $p \in \mathbb{C}$ and $\bar{p} \in \mathbb{C}$, and the conjugate complex residues $R \in \mathbb{C}^{n_y \times n_u}$ and $\bar{R} \in \mathbb{C}^{n_y \times n_u}$. Blending the inputs and outputs of such a second-order mode, the transfer function $m(s) = k_y^T M(s) k_u = r_1 \frac{s-z}{s^2+2\zeta\omega_n s+\omega_n^2}$ is obtained, where the zero $z \in \mathbb{R}$, the gain $r_1 \in \mathbb{R}$, the natural frequency $\omega_n \in \mathbb{R}_{>0}$, and the relative damping $\zeta \in [-1, 1]$. Considering the magnitude of the frequency response of $m(s)$, it features only a single peak (or maximum) and increasing this single peak generally increases also the area below it. Since the peak is associated to the \mathcal{H}_∞ norm and the area below to the \mathcal{H}_2 norm of the blended mode, \mathcal{H}_2 - and \mathcal{H}_∞ -optimality of blending vectors are closely related. This relation becomes especially obvious when considering lightly damped modes, i.e., $\zeta = -\Re(p)/|p| \ll 1$, as in this case

$$\|m(s)\|_{\mathcal{H}_\infty} \approx |m(j\omega_n)| = \frac{\|m(s)\|_{\mathcal{H}_2}}{\sqrt{\zeta\omega_n}}, \quad (3.47)$$

which directly results from Definition 3.5 and Theorem 3.2. More precisely, the \mathcal{H}_∞ norm of a SISO system is the largest magnitude of its frequency response, which is around natural frequency $\omega_n = |p|$ for lightly damped modes. The

magnitude of the frequency response at ω_n , in turn, is directly related to the \mathcal{H}_2 norm as given by the right hand side of Equation (3.47).

For a better understanding, the magnitude of an example transfer function $m(s) = \omega_n^2 / (s^2 + 2\zeta\omega_n s + \omega_n^2)$ is plotted in Figure 3.2 for different values of relative damping ζ . The corresponding peak values are connected with a red line (—) which approaches ω_n with decreasing ζ . Hence, the \mathcal{H}_∞ norm of a lightly damped mode with blended inputs and outputs can be approximated by the magnitude of its frequency response at ω_n and is thus proportional to the \mathcal{H}_2 norm. Note that this example only shows the relation of the \mathcal{H}_∞ and \mathcal{H}_2 norms for blended modes with $z = 0$. However, it is observed for blended modes that a large value of one norm typically also yields a large value of the other norm, see also the example in Section 3.3.5.

Based on the close relation of the \mathcal{H}_∞ and \mathcal{H}_2 norm measure for blending vector efficiency, a connection to measures based on the Hankel singular values is given by the following theorem.

Theorem 3.3 (Upper and lower bound of \mathcal{H}_∞ norm [169]). *Let the asymptotically stable LTI system $G(s)$ be given. Then,*

$$\|G(s)\|_{\mathcal{H}} \leq \|G(s)\|_{\mathcal{H}_\infty} \leq 2 \sum_{k=1}^{n_x} \sigma_{\mathcal{H},k}, \quad (3.48)$$

where $\|\bullet\|_{\mathcal{H}}$ and $\|\bullet\|_{\mathcal{H}_\infty}$ denote the Hankel and \mathcal{H}_∞ norm, respectively, and $\sigma_{\mathcal{H},k}$ are the Hankel singular values of $G(s)$.

Proof. The proof can be found in [169]. □

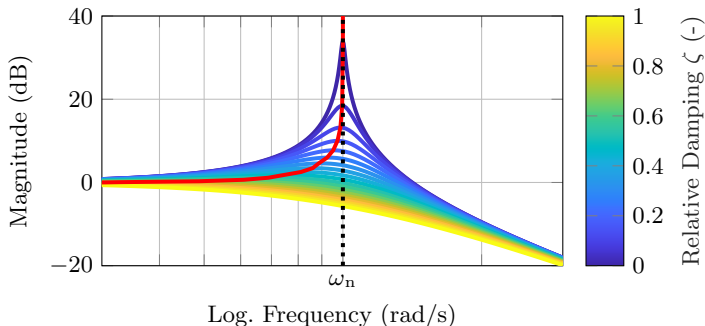


Figure 3.2: Magnitude of the transfer function $m(s) = \omega_n^2 / (s^2 + 2\zeta\omega_n s + \omega_n^2)$ for varying relative dampings ζ . The corresponding peak values, which are equivalent to the respective \mathcal{H}_∞ norm, are connected with (—).

Theorem 3.3 reveals that the \mathcal{H}_∞ norm provides a lower bound to the double sum of the Hankel singular values of the underlying system. In this respect, a large \mathcal{H}_∞ norm generally implies also large Hankel singular values, where a second-order mode features at most two non-zero Hankel singular values. Hence, it can be assumed that blending vectors which maximize the \mathcal{H}_2 norm of the blended mode also result in large Hankel singular values, especially in case of light damping.

In addition to this, it is shown in Section 3.2.4 that, for undamped modes, the generalized \mathcal{H}_2 -optimal blending vectors are also optimal in terms of the Litz dominance measure. This can be directly seen from Proposition 3.2, which describes the blending vector efficiency for undamped modes as $\eta_{\text{lim}} = |k_y^T R k_u| / \|R\|_F$. Thus, maximizing η_{lim} during blending vector design also maximizes the Litz dominance measure, which is also driven by the term $|k_y^T R k_u|$ as given in Definition 3.7. Note that the same holds when using the conjugate complex residue \bar{R} instead of R .

Finally, it is noted that the discussed connections of the different modal controllability and observability measures are demonstrated by means of a numerical example in Section 3.3.5.

3.2.5 Summary \mathcal{H}_2 -optimal Blending Vector Computation

The \mathcal{H}_2 -optimal blending vector design problem defined in Equation (3.22) can be efficiently solved by first solving the optimization problem

$$\phi^* = \arg \max_{\phi \in \mathbb{R}} \|F(\phi)\|_2, \quad (3.49)$$

where

$$F(\phi) = \Re(M(j\omega_n)) \cos \phi + \Im(M(j\omega_n)) \sin \phi. \quad (3.50)$$

In Equation (3.50), $M(j\omega_n)$ denotes the frequency response of the targeted mode $M(s)$ at its natural frequency ω_n . To also consider undamped or unstable modes, for which the \mathcal{H}_2 norm is infinite by definition, it is proposed to adapt $F(\phi)$ as described in Section 3.2.4. Note that due to the given periodicity of $F(\phi)$, the search for an optimal phase angle may be restricted to an interval of size π , e.g., $\phi \in [0, \pi[$. Additionally, computational effort for solving optimization problem (3.49) may be further reduced by a preceding decomposition of $M(s)$ according to Equation (3.37). After determining ϕ^* according to Equation (3.49), the corresponding \mathcal{H}_2 -optimal input and output blending vectors k_u^* and k_y^* can be derived carrying out an SVD on

$$F(\phi^*) = U \Sigma V^T = \begin{bmatrix} k_y^* & \bullet \\ 0 & \bullet \end{bmatrix} \begin{bmatrix} \sigma^* & 0 \\ 0 & \bullet \end{bmatrix} \begin{bmatrix} k_u^* & \bullet \end{bmatrix}^T, \quad (3.51)$$

where $\sigma^* = \|F(\phi^*)\|_2$ denotes the maximum singular value of $F(\phi^*)$. Furthermore, it is noted that the computation of the \mathcal{H}_2 -optimal blending vectors greatly simplifies for systems with a single input or a single output and also for modes with a single real pole as discussed in Section 3.2.4.

3.2.6 Numerical Examples

Example 1: Comparison of Jointly and Separately Computed Blending Vectors

In Section 3.2.4, blending vectors are derived which are considered as \mathcal{H}_2 -optimal when applied individually, i.e., when blending only inputs or only outputs. In the following example, it is demonstrated that these separately computed blending vectors do not necessarily yield \mathcal{H}_2 -optimality when applied together. The considered oscillating mode $M(s) = C(sI - A)^{-1}B$ is defined by

$$A = \begin{bmatrix} -1 & 1 \\ -1 & -1 \end{bmatrix}, B = \begin{bmatrix} 0.78 & 1.20 \\ 1.17 & -0.79 \end{bmatrix}, C = \begin{bmatrix} 1.74 & 3.14 \\ -3.11 & 1.69 \end{bmatrix}, \quad (3.52)$$

and features a natural frequency $\omega_n = \sqrt{2}$ and a relative damping $\zeta = 1/\sqrt{2}$. In a first step, input and output blending vectors which guarantee \mathcal{H}_2 -optimality when applied together are jointly computed as summarized in Section 3.3.4. To that end, the optimization problem (3.49) is solved and $\phi^* \approx 3\pi/4 + k\pi, k \in \mathbb{Z}$ is obtained. The corresponding \mathcal{H}_2 -optimal pair of input and output blending vectors is then derived according to Equation (3.51) as

$$k_u^* = \begin{bmatrix} -0.074 \\ 0.997 \end{bmatrix} \quad \text{and} \quad k_y^* = \begin{bmatrix} -0.524 \\ -0.852 \end{bmatrix}.$$

Normalizing the objective function $\|F(\phi)\|_2$ from Equation (3.49) by $\|M(j\omega_n)\|_2$ yields the efficiency factor η from Equation (3.21) as a function of the optimization variable ϕ . Depicting $\eta(\phi)$ in Figure 3.3, it can be seen that the corresponding maximum value

$$\eta^* = \frac{\|k_y^{*T} M(s) k_u^*\|_{\mathcal{H}_2}}{\|M(s)\|_{\mathcal{H}_2}} = \frac{\|F(\phi^*)\|_2}{\|M(j\omega_n)\|_2} = 0.66 \quad (3.53)$$

can easily be found using some gradient-based optimization algorithm. In a second step, the input and output blending vectors are computed separately according to Equations (3.44) and (3.45) as

$$k_{u,\text{in}}^* = \begin{bmatrix} 0.047 \\ 0.999 \end{bmatrix} \quad \text{and} \quad k_{y,\text{out}}^* = \begin{bmatrix} -0.935 \\ -0.354 \end{bmatrix}.$$

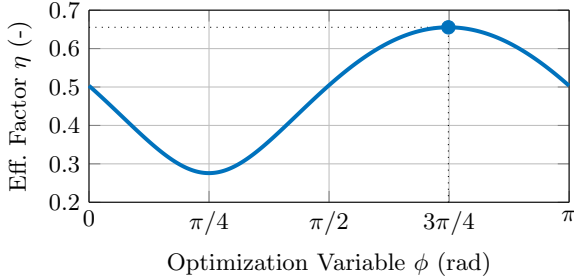


Figure 3.3: Efficiency factor $\eta(\phi)$ to be maximized for \mathcal{H}_2 -optimal blending of inputs and outputs.

As already described, these two blending vectors are considered \mathcal{H}_2 -optimal only when applied individually but not jointly. This becomes obvious when computing the efficiency factor

$$\eta_{\text{in-out}}^* = \frac{\|k_{y,\text{out}}^{*T} M(s) k_{u,\text{in}}^*\|_{\mathcal{H}_2}}{\|M(s)\|_{\mathcal{H}_2}} = 0.51,$$

which is clearly smaller than $\eta^* = 0.66$ from Equation (3.53). Blending the mode $M(s)$ with the two different pairs of input and output blending vectors yields the transfer functions

$$\begin{aligned} k_y^{*T} M(s) k_u^* &= 4.68 \frac{s + 1.43}{s^2 + 2s + 2}, \\ k_{y,\text{out}}^{*T} M(s) k_{u,\text{in}}^* &= 1.95 \frac{s + 3.44}{s^2 + 2s + 2}, \end{aligned}$$

which are compared in Figure 3.4. Therein, the difference of the computed efficiency factors η^* and $\eta_{\text{in-out}}^*$ is clearly recognizable since the \mathcal{H}_2 norm of a SISO system is related to the area below its maximum singular value.

Example 2: Impact of Input and Output Scaling on Blending Vector Design

As described in Section 3.2.4, the scaling of inputs and outputs usually affects the resulting \mathcal{H}_2 -optimal blending vectors. To demonstrate this, the \mathcal{H}_2 -optimal output blending vectors are computed for the mode

$$M(s) = C(sI - A)^{-1}B = \begin{bmatrix} 9 & 9 \\ 1 & 2 \end{bmatrix} \left(sI - \begin{bmatrix} -1 & 1 \\ -1 & -1 \end{bmatrix} \right)^{-1} \begin{bmatrix} 0 \\ 1 \end{bmatrix} \quad (3.54)$$

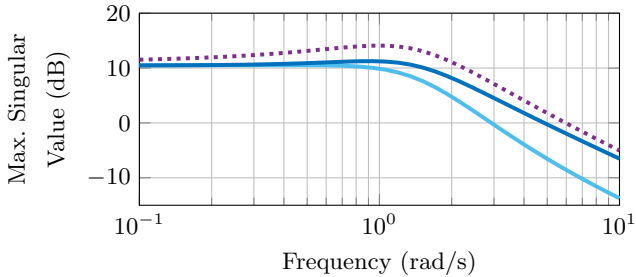


Figure 3.4: Comparison of the maximum singular value of the mode $M(s)$ without blended inputs and outputs (\cdots), and with inputs and outputs blended by jointly (—) and separately (—) computed \mathcal{H}_2 -optimal blending vectors.

using two different output scalings. Considering that both measurements are of same unit, the unit normalization proposed in Section 3.2.4 yields a unit scaling matrix $S_{y,1} = I$. For the scaled mode $S_{y,1}M(s)$, the scaled \mathcal{H}_2 -optimal output blending vector $\bar{k}_{y,1}$ is computed according to Equation (3.45). From $\bar{k}_{y,1}$, the actual blending vector of unit length is then obtained as

$$k_{y,1} = \frac{S_{y,1}\bar{k}_{y,1}}{\|S_{y,1}\bar{k}_{y,1}\|_2} = \bar{k}_{y,1} = \begin{bmatrix} 0.983 \\ 0.182 \end{bmatrix},$$

which is identical to the scaled blending vector since $S_{y,1}$ is a unit matrix. The obtained blending vector $k_{y,1}$ clearly prioritizes the first measurement and yields an efficiency factor

$$\eta_1 = \frac{\|k_{y,1}M(s)\|_{\mathcal{H}_2}}{\|M(s)\|_{\mathcal{H}_2}} \approx 1. \quad (3.55)$$

This means that blending the outputs of mode $M(s)$ does not, or only marginally, reduce its observability. In contrast, scaling both measurements with their corresponding maximum value $y_{\max} = [5 \ 1]$ yields the scaled \mathcal{H}_2 -optimal output blending vector $\bar{k}_{y,2} = [0.730 \ 0.683]^T$, from which the actual blending vector is computed as

$$k_{y,2} = \frac{S_{y,2}\bar{k}_{y,2}}{\|S_{y,2}\bar{k}_{y,2}\|_2} = \begin{bmatrix} 0.209 \\ 0.978 \end{bmatrix},$$

where the corresponding scaling matrix $S_{y,2} = \text{diag}(y_{\max})^{-1}$. The resulting efficiency factor

$$\eta_2 = \frac{\|k_{y,2}M(s)\|_{\mathcal{H}_2}}{\|M(s)\|_{\mathcal{H}_2}} \approx 0.38 \quad (3.56)$$

is clearly less than $\eta_1 \approx 1$ from unit scaling. This is reasonable since the obtained blending vector prioritizes the second measurement, which has a smaller gain than the first measurement. Hence, it is summarized that the scaling of inputs and outputs usually affects the resulting blending vectors. This, however, may also be used as a tuning possibility for blending vector design.

3.3 Blending-based Pole Placement

For many dynamical systems it is required to specifically shift the poles of an individual mode, especially when these poles are lightly damped or even unstable. To achieve that, a novel pole placement approach is developed in this section, which is based on blending control inputs and measurement outputs. Thereby, the goal for blending vector design is to create a SISO loop with a desirable root locus along which the targeted pole is moved by means of a static gain feedback of minimal magnitude. As a result, a static output feedback controller of rank one is obtained for each mode to be controlled. To ensure a sufficient isolation of the targeted modes, respective decoupling techniques are described in Section 3.4 and can be directly considered during blending vector design. The effectiveness of the proposed pole placement approach is demonstrated by means of a numerical example in Section 3.3.5 and a realistic aeronautical application in Section 5.1.

3.3.1 Problem Definition

The task of shifting the pole(s) of an individual mode $M(s)$ to a desired location can quickly become challenging when the number of control inputs or measurement outputs is increased. To reduce the complexity of the control problem, it is proposed to first blend inputs and outputs and then apply a constant feedback for the desired pole placement. As a result, a static output feedback controller of rank one is obtained as

$$K = k_u \lambda k_y^T, \quad (3.57)$$

where $k_u \in \mathbb{R}^{n_u}$ and $k_y \in \mathbb{R}^{n_y}$ are the corresponding input and output blending vectors, and $\lambda \in \mathbb{R}$ is the feedback gain. The resulting closed-loop interconnection for controlling a single mode $M(s)$ is given in Figure 3.5, where the controller K is composed as given in Equation (3.57).

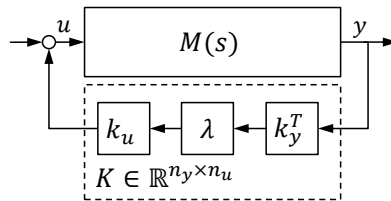


Figure 3.5: Closed-loop interconnection of mode $M(s)$ with static output feedback controller K for pole placement.

In order to derive the rank-one controller K , it is suggested to split up its design into a blending vector design and a subsequent feedback gain computation. The goal is thereby to achieve the desired closed-loop dynamics with a minimum absolute feedback gain $|\lambda|$ and blending vectors of unit length, i.e., $\|k_u\|_2 = 1$ and $\|k_y\|_2 = 1$. Thus, a pair of input and output blending vectors of unit length is considered as optimal for the given control problem when $|\lambda|$ is minimal. In what follows, the underlying optimization problem for the corresponding controller synthesis is derived.

According to Equation (3.8), the transfer function matrix of an oscillating mode with a conjugate complex pole pair p and \bar{p} is given as

$$M(s) = \frac{R_1 s + R_0}{(s - p)(s - \bar{p})} = \frac{R_1 s + R_0}{s^2 + 2\zeta\omega_n s + \omega_n^2}, \quad (3.58)$$

where $R_0 \in \mathbb{R}^{n_y \times n_u}$, $R_1 \in \mathbb{R}^{n_y \times n_u}$, $\omega_n = |p| \neq 0$ and $\zeta = -\Re(p)/\omega_n$. Blending the inputs and outputs of $M(s)$ through the vectors k_u and k_y yields

$$m(s) = k_y^T M(s) k_u = \frac{r_1 s + r_0}{s^2 + 2\zeta\omega_n s + \omega_n^2}, \quad (3.59)$$

with the coefficients

$$r_0 = k_y^T R_0 k_u \quad \text{and} \quad r_1 = k_y^T R_1 k_u. \quad (3.60)$$

From Equation (3.59), it can be seen that the blending of inputs and outputs does not change the poles of the underlying mode but rather specifies a zero at

$$z = -\frac{r_0}{r_1}. \quad (3.61)$$

The closed-loop transfer function for feedback of the blended outputs to the blended inputs with gain λ is obtained as

$$m_{\text{cl}}(s) = \frac{m(s)}{1 - \lambda m(s)} = \frac{r_1 s + r_0}{s^2 + \underbrace{(2\zeta\omega_n - \lambda r_1)}_{2\zeta_{\text{cl}}\omega_{\text{n,cl}}} s + \underbrace{\omega_n^2 - \lambda r_0}_{\omega_{\text{n,cl}}^2}}. \quad (3.62)$$

To achieve desired closed-loop dynamics, i. e., a specified natural frequency $\omega_{\text{n,cl}}$ and relative damping ζ_{cl} , the two conditions hence are

$$\omega_n^2 - \lambda r_0 = \omega_{\text{n,cl}}^2, \quad (3.63)$$

$$2\zeta\omega_n - \lambda r_1 = 2\zeta_{\text{cl}}\omega_{\text{n,cl}}. \quad (3.64)$$

Based on Equations (3.63) and (3.64), the blending vector design problem to achieve the desired pole placement with a feedback gain λ of minimum magnitude is thus given as

$$\begin{aligned}
 & \text{minimize} && |\lambda| \\
 & \lambda \in \mathbb{R}, k_u \in \mathbb{R}^{n_u}, k_y \in \mathbb{R}^{n_y} \\
 & \text{subject to} && \lambda k_y^T R_0 k_u = \omega_n^2 - \omega_{n,\text{cl}}^2 \\
 & && \lambda k_y^T R_1 k_u = 2\zeta\omega_n - 2\zeta_{\text{cl}}\omega_{n,\text{cl}} \\
 & && \|k_u\|_2 = 1 \\
 & && \|k_y\|_2 = 1.
 \end{aligned} \tag{3.65}$$

To efficiently solve the optimization problem (3.65), it is first reformulated. To this end, Equations (3.63) and (3.64) are solved for r_0 and r_1 , respectively, and the location of the zero z from Equation (3.61) is computed as

$$z = -\frac{r_0}{r_1} = -\frac{\omega_n^2 - \omega_{n,\text{cl}}^2}{2(\zeta\omega_n - \zeta_{\text{cl}}\omega_{n,\text{cl}})}. \tag{3.66}$$

The case $\zeta\omega_n = \zeta_{\text{cl}}\omega_{n,\text{cl}}$ is a singularity which is treated in Section 3.3.3. The singularity occurs when a conjugate complex pole pair is shifted only in the direction of the imaginary axis, i.e., $\Re(p) = \Re(p_{\text{cl}})$. In this case, the resulting zero can be interpreted as $z = \infty$, where it is noted that in reality it does not exist since $r_1 = 0$. Another special case discussed in Section 3.3.3 is $\omega_n^2 = \omega_{n,\text{cl}}^2$, which yields $z = 0$. In that case, the relative damping is changed without affecting the natural frequency. In other words, the conjugate complex pole pair is shifted along a circle around the origin. Both special cases are marked in Figure 3.6, that illustrates the possible closed-loop locations in the complex plane for a given pole pair (✕) in dependence on the sign of z .

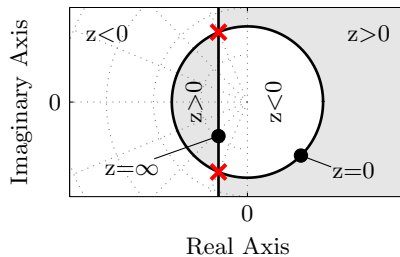


Figure 3.6: Possible closed-loop pole locations for a given pole pair (✕) in the complex plane in dependence on the zero z generated by blending inputs and outputs.

In order to derive the blending vector design problem, Equation (3.61) is reformulated as

$$r_0 + zr_1 = 0, \quad (3.67)$$

where the zero location z is specified by Equation (3.66). Substituting $r_0 = k_y^T R_0 k_u$ and $r_1 = k_y^T R_1 k_u$ from Equation (3.60) in Equation (3.67), and factoring out the blending vectors k_u and k_y yields

$$k_y^T \underbrace{(R_0 + zR_1)}_P k_u = 0 \quad (3.68)$$

as a necessary constraint for k_y and k_u . To incorporate the objective of minimizing the magnitude of the feedback gain $|\lambda|$, Equation (3.64) is reformulated as

$$\lambda = 2 \frac{\zeta\omega_n - \zeta_{cl}\omega_{n,cl}}{r_1}, \quad (3.69)$$

which shows that minimizing $|\lambda|$ is equivalent to maximizing $|r_1|$. Recalling from Equation (3.60) that $r_1 = k_y^T R_1 k_u$ hence yields the equivalent objective function

$$\max |r_1| = \max |k_y^T R_1 k_u|. \quad (3.70)$$

Note that maximizing $|r_1|$ also maximizes the \mathcal{H}_2 norm of the blended mode on condition that the zero z is fixed as required for pole placement. This becomes obvious when computing the \mathcal{H}_2 norm of the blended mode from Equation (3.59) as

$$\|k_y^T M(s) k_u\|_{\mathcal{H}_2} = \left\| \frac{r_1 s + r_0}{s^2 + 2\zeta\omega_n s + \omega_n^2} \right\|_{\mathcal{H}_2} = |r_1| \left\| \frac{s - z}{s^2 + 2\zeta\omega_n s + \omega_n^2} \right\|_{\mathcal{H}_2}. \quad (3.71)$$

Hence, blending vectors which solve Equation (3.65) are considered as \mathcal{H}_2 -optimal provided that the pole placement constraints from Equations (3.63) and (3.64) are fulfilled. Furthermore, Equation (3.71) reveals that blending vector optimality is not only given in terms of the \mathcal{H}_2 norm but also in terms of other system norms such as the Hankel or \mathcal{H}_∞ norm. This is due to the fact that only the constant value $|r_1|$ is maximized while the remaining part including the dynamics of the mode does not change.

Combining the constraint (3.68) with the objective function (3.70), the blending vector design problem for pole placement is eventually formulated as

$$\begin{aligned} & \underset{k_u \in \mathbb{R}^{n_u}, k_y \in \mathbb{R}^{n_y}}{\text{maximize}} && |k_y^T R_1 k_u| \\ & \text{subject to} && k_y^T P k_u = 0 \\ & && \|k_u\|_2 = 1 \\ & && \|k_y\|_2 = 1, \end{aligned} \quad (3.72)$$

where $P = R_0 + zR_1$ according to Equation (3.68) and $z = \frac{\omega_{n,c1}^2 - \omega_n^2}{2(\zeta\omega_n - \zeta_{c1}\omega_{n,c1})}$ according to Equation (3.66). Solving the optimization problem (3.72), optimal blending vectors are obtained, which are then inserted into Equation (3.69) directly yielding the corresponding minimum feedback gain. Hence, the computation of the overall controller K is reduced to solving Equation (3.72).

3.3.2 Efficient Blending Vector Computation

In this subsection, a numerically efficient algorithm for solving the blending vector design problem (3.72) is derived. The algorithm is described without loss of generality for a system with $n_u \leq 2$ inputs and $n_y \leq 2$ outputs. For systems with $n_u > 2$ or $n_y > 2$, a dynamic mode can always be expressed as

$$M(s) = Q_C \underbrace{R_C(sI - A)^{-1} R_B^T Q_B^T}_{\tilde{M}(s)}, \quad (3.73)$$

where both $Q_C \in \mathbb{R}^{n_y \times n_{\tilde{y}}}$ and $Q_B \in \mathbb{R}^{n_u \times n_{\tilde{u}}}$ form orthonormal bases, and $\tilde{M}(s)$ is a transfer function matrix with $n_{\tilde{u}} \leq 2$ inputs and $n_{\tilde{y}} \leq 2$ outputs, see Appendix A.1 for more details. Hence, the input and output blending vectors \tilde{k}_u and \tilde{k}_y for controlling $\tilde{M}(s)$ can be computed as follows and of these, the blending vectors for controlling the original mode $M(s)$ are obtained as

$$k_u = Q_B \tilde{k}_u \quad \text{and} \quad k_y = Q_C \tilde{k}_y. \quad (3.74)$$

Note that Q_B and Q_C act as unitary transformations such that neither the objective function nor the length of the blending vectors is affected.

For efficiently computing the optimal blending vectors, the pole placement constraint $k_y^T P k_u = 0$ from Equation (3.68) is used to reduce the number of decision variables in Equation (3.72). Considering a mode with $n_u = 2$ inputs and $n_y = 2$ outputs, three different cases need to be distinguished thereby depending on the rank of P , which is at most two.

Case 1 (rank $P = 2$)

Since P has full rank, the constraint $k_y^T P k_u = 0$ can only be satisfied when k_y is orthogonal to $P k_u$. This allows computing the output blending vector k_y from a given input blending vector k_u . Define the signed permutation matrix

$$\Pi = \begin{bmatrix} 0 & -1 \\ 1 & 0 \end{bmatrix}. \quad (3.75)$$

A suitable output blending vector then is

$$k_y = \pm \frac{\Pi P k_u}{\|P k_u\|_2}. \quad (3.76)$$

Note that in Equation (3.76), the output blending vector is normalized to length one, i.e., the constraint $\|k_y\|_2 = 1$ is achieved. To ensure the same for the input blending vector, k_u is expressed in polar coordinates as

$$k_u = \begin{bmatrix} \cos \phi \\ \sin \phi \end{bmatrix}. \quad (3.77)$$

As a result, $k_u(\phi)$ depends on the single parameter $\phi \in \mathbb{R}$. From Equation (3.76), $k_y(k_u(\phi))$ is also uniquely determined through ϕ . Hence, the optimization problem (3.72) can be equivalently reformulated as the unconstrained optimization problem

$$\max_{\phi \in \mathbb{R}} \frac{|k_u(\phi)^T P^T \Pi^T R_1 k_u(\phi)|}{\|Pk_u(\phi)\|_2}. \quad (3.78)$$

With $\phi^* \in \mathbb{R}$ solving Equation (3.78), optimal input and output blending vectors are directly obtained from Equation (3.77) and Equation (3.76) as $k_u^* = [\cos \phi^* \ \sin \phi^*]^T$ and $k_y^* = \Pi P k_u^* / \|P k_u^*\|_2$, respectively.

Case 2 (rank $P = 1$)

If rank $P = 1$, an SVD on P yields

$$P = U \Sigma V^T = \begin{bmatrix} u_1 & u_2 \end{bmatrix} \begin{bmatrix} \sigma_1 & 0 \\ 0 & 0 \end{bmatrix} \begin{bmatrix} v_1 & v_2 \end{bmatrix}^T, \quad (3.79)$$

where both $U \in \mathbb{R}^{2 \times 2}$ and $V \in \mathbb{R}^{2 \times 2}$ are orthogonal matrices, and $\sigma_1 \in \mathbb{R}_{>0}$. From Equation (3.79), two candidate pairs $i = 1, 2$ of optimal input and output blending vectors $k_{u,i}^*$ and $k_{y,i}^*$ are directly obtained as

$$k_{y,1}^* = u_2 \Rightarrow k_{u,1}^* = \frac{R_1^T k_{y,1}^*}{\|R_1^T k_{y,1}^*\|_2}, \quad (3.80)$$

$$k_{u,2}^* = v_2 \Rightarrow k_{y,2}^* = \frac{R_1 k_{u,2}^*}{\|R_1 k_{u,2}^*\|_2}. \quad (3.81)$$

The idea behind Equations (3.80) and (3.81) is to first select an input or output blending vector $k_{u,2}^*$ or $k_{y,1}^*$ that satisfies the pole placement constraint $k_y^T P k_u = 0$ from Equation (3.68). Then, the objective function $|k_y^T R_1 k_u|$ from Equation (3.72) can only be maximized when either $k_{u,1}^*$ is parallel to $(k_{y,1}^*)^T R_1$ or $k_{y,2}^*$ is parallel to $R_1 k_{u,2}^*$. Eventually, the pair of blending vectors that yields the maximum objective function $|(k_{y,i}^*)^T R_1 k_{u,i}^*|$ is considered as optimal.

Case 3 (rank $P = 0$)

In case rank $P = 0$, the constraint $k_y^T P k_u = 0$ vanishes and the optimal blending vectors k_y^* and k_u^* are directly obtained from an SVD on R_1 . More specifically, the objective $|k_y^T R_1 k_u|$ is maximized by choosing k_y and k_u as the left and right singular vectors associated with the largest singular value of R_1 .

3.3.3 Special Cases

This subsection discusses special cases of the proposed pole placement method that either simplify the computation of the blending vectors or are of conceptual interest.

Active Damping

When the control objective is to increase relative damping of an individual mode without affecting its natural frequency, i.e., $\zeta_{cl} > \zeta$ and $\omega_{n,cl} = \omega_n$, the poles are shifted along a circle around the origin, see Figure 3.6. In that case, Equation (3.63) states that $r_0 = 0$ for $\lambda \neq 0$. That is, the optimal blending of inputs and outputs places the zero of the blended mode's transfer function at $z = 0$, see Equation (3.66). While this does not affect the algorithm described in Section 3.3.2, it establishes connections to other commonly encountered control techniques. As a zero at the origin is the frequency domain equivalent to differentiation, the blended measurement signal can be interpreted as a generalized velocity of the dynamic mode, confer [26, 56, 154, 155]. Feeding back such a velocity naturally increases modal damping, see, e.g., [12, 121, 125].

Shifting Poles Parallel to the Imaginary Axis

When the given open-loop poles and desired closed-loop poles have the same real part, i.e., $\Re(p) = \Re(p_{cl})$, $\zeta\omega_n = \zeta_{cl}\omega_{n,cl}$ and Equation (3.66) becomes singular. It follows from (3.64) that $r_1 = 0$ for $\lambda \neq 0$. As a result, the new pole placement constraint is $k_y^T R_1 k_u = 0$ instead of (3.68). Further, the objective function (3.70) is replaced by $\max |k_y^T R_0 k_u|$, as $\min |\lambda|$ with $\lambda = (\omega_n^2 - \omega_{n,cl}^2)/r_0$ from Equation (3.63) is now equivalent to $\max |r_0|$. Summing up, the blending vector design problem for the singular case $\zeta\omega_n = \zeta_{cl}\omega_{n,cl}$ is given as

$$\begin{aligned} & \underset{k_u \in \mathbb{R}^{n_u}, k_y \in \mathbb{R}^{n_y}}{\text{maximize}} && |k_y^T R_0 k_u| \\ & \text{subject to} && k_y^T R_1 k_u = 0 \\ & && \|k_u\|_2 = 1 \\ & && \|k_y\|_2 = 1 \end{aligned} \tag{3.82}$$

and can be solved again as described in Section 3.3.2.

Real-valued Poles

In case the targeted mode features only a single real-valued pole $p \in \mathbb{R}$, i.e., the transfer function is $M(s) = c(s - p)^{-1}b^T$ with $b \in \mathbb{R}^{n_u}$ and $c \in \mathbb{R}^{n_y}$, the pole can only be shifted along the real axis. In that case, the open- and closed-loop transfer functions of the blended mode are given as

$$m(s) = k_y^T M(s) k_u = \frac{k_y^T c b^T k_u}{s - p} \quad (3.83)$$

and

$$m_{cl}(s) = \frac{m(s)}{1 - \lambda m(s)} = \frac{k_y^T c b k_u}{s - \underbrace{(p + \lambda k_y^T c b k_u)}_{p_{cl}}}. \quad (3.84)$$

From Equation (3.84), the feedback gain required to place the closed-loop pole at $p_{cl} \in \mathbb{R}$ is directly given as

$$\lambda = \frac{p_{cl} - p}{k_y^T c b k_u}. \quad (3.85)$$

Its absolute value is minimized when the blending vectors of unit length are chosen as

$$k_u^* = \frac{b}{\|b\|_2} \quad \text{and} \quad k_y^* = \frac{c}{\|c\|_2}. \quad (3.86)$$

In case it is desired to shift a conjugate complex pole pair onto the real axis, the resulting mode can be seen as an overdamped system with two poles $p_1 \in \mathbb{R}$ and $p_2 \in \mathbb{R}$ on the real axis. In that case, it follows from $(s - p_1)(s - p_2) = s^2 + 2\zeta\omega_n s + \omega_n^2$ that

$$\omega_n^2 = p_1 p_2 \quad \text{and} \quad 2\omega_n \zeta = -p_1 - p_2. \quad (3.87)$$

Substituting (3.87) in (3.66), the same algorithm as described in Section 3.3.2 can again be used.

Single-Input or Single-Output Systems

For a system with a single input but $n_y > 1$ linearly independent outputs, it follows from Equation (3.68) that $P \in \mathbb{R}^{n_y \times 1}$. In that case, the optimal blending vectors, which solve the optimization problem (3.72), are directly obtained from the constraint (3.68) as

$$k_u^* = 1 \quad \text{and} \quad k_y^* = \pm \Pi P / \|\Pi P\|_2, \quad (3.88)$$

where the permutation matrix Π is defined in Equation (3.75). Similarly, for a system with a single output but $n_u > 1$ linearly independent inputs, $P \in \mathbb{R}^{1 \times n_u}$ and

$$k_u^* = \pm \Pi P^T / \|P\|_2 \quad \text{and} \quad k_y^* = 1. \quad (3.89)$$

Note that this case of only a single input or a single output greatly simplifies the computation of the optimal blending vectors.

3.3.4 Summary Blending-based Pole Placement Algorithm

In order to allow for a straightforward application of the proposed pole placement approach, the findings of Sections 3.3.1 and 3.3.2 are summarized as follows. To begin with, it is recalled that the control objective is to shift the natural frequency and relative damping of an oscillating mode $M(s)$ from $\omega_n \rightarrow \omega_{n,\text{cl}}$ and from $\zeta \rightarrow \zeta_{\text{cl}}$, respectively. A decomposition as stated in (3.73) yields then

$$M(s) = Q_C \frac{R_1 s + R_0}{s^2 + 2\zeta\omega_n s + \omega_n^2} Q_B^T, \quad (3.90)$$

where R_0 and R_1 are real-valued matrices of maximum dimension 2×2 , and both Q_B and Q_C form orthogonal bases. According to (3.77) and (3.76), the blending vectors to achieve the desired pole placement in the generic case $\zeta\omega_n \neq \zeta_{\text{cl}}\omega_{n,\text{cl}}$ are

$$k_u(\phi) = \begin{bmatrix} \cos \phi \\ \sin \phi \end{bmatrix} \quad \text{and} \quad k_y(\phi) = \pm \frac{\Pi P k_u(\phi)}{\|P k_u(\phi)\|_2}, \quad (3.91)$$

where

$$\Pi = \begin{bmatrix} 0 & -1 \\ 1 & 0 \end{bmatrix} \quad \text{and} \quad P = R_0 + \underbrace{\frac{\omega_{n,\text{cl}}^2 - \omega_n^2}{2(\zeta\omega_n - \zeta_{\text{cl}}\omega_{n,\text{cl}})}}_z R_1. \quad (3.92)$$

Solving the equivalent optimization problem (3.78) yields

$$\phi^* = \arg \max_{\phi} \frac{|k_u(\phi)^T P^T \Pi^T R_1 k_u(\phi)|}{\|P k_u(\phi)\|_2}, \quad (3.93)$$

which allows computation of $k_u(\phi^*)$ and $k_y(\phi^*)$ by inserting $\phi = \phi^*$ into Equation (3.91). Note that due to the given periodicity of $k_u(\phi)$, the search for an optimal ϕ^* may be restricted to an interval of size π , e.g., $\phi \in [0, \pi[$. The optimal input and output blending vectors are then obtained from Equation (3.74) as

$$k_u^* = Q_B k_u(\phi^*) \quad \text{and} \quad k_y^* = Q_C k_y(\phi^*). \quad (3.94)$$

Eventually, the desired closed-loop dynamics are achieved by closing the loop with the feedback controller

$$K = \lambda^* k_u^* k_y^{*T}, \quad (3.95)$$

where the feedback gain with minimum magnitude is computed according to Equation (3.69) as

$$\lambda^* = 2 \frac{\zeta \omega_n - \zeta_{cl} \omega_{n,cl}}{k_y (\phi^*)^T R_1 k_u (\phi^*)}. \quad (3.96)$$

Note that Equations (3.91) to (3.93) assume the case $\text{rank } P = 2$. The computation greatly simplifies in case $\text{rank } P < 2$ or when only a single input or output is considered, see Sections 3.3.2 and 3.3.3. For the singular case with $\zeta \omega_n = \zeta_{cl} \omega_{n,cl}$, the matrix R_1 is replaced by R_0 and P is replaced by R_1 in Equations (3.91) and (3.93). The optimal blending vectors are then computed in the same way, but the feedback gain is $\lambda^* = \frac{\omega_n^2 - \omega_{n,cl}^2}{k_y (\phi^*)^T R_1 k_u (\phi^*)}$ as given in Section 3.3.3.

3.3.5 Numerical Examples

Critical Damping

To demonstrate the blending-based pole placement approach, the mode $M(s)$ of the first numerical example from Section 3.2.6 is considered. The control objective is to achieve critical damping, i.e., $\zeta_{cl} = 1$, while the natural frequency should remain unaffected, i.e., $\omega_{n,cl} = \omega_n = \sqrt{2}$. In other words, it is desired to move the open-loop conjugate complex pole pair $p_{1,2} = -1 \pm 1j$ onto the real axis as $p_1 = p_2 = -1$ using the developed pole placement control approach. Note that increasing the damping without changing the frequency of a conjugate complex pole pair is considered as *active damping* as discussed in Section 3.3.3. According to Equation (3.66), the required location of the zero $z = 0$, which results in $P = R_0$ when inserted into Equation (3.68). Solving the unconstrained optimization problem (3.78) yields $\phi^* = 0.333$. Inserting this value into Equations (3.76) and (3.77) yields the optimal input and output blending vectors

$$k_u^* = \begin{bmatrix} 0.326 \\ 0.945 \end{bmatrix} \quad \text{and} \quad k_y^* = \begin{bmatrix} -0.855 \\ 0.518 \end{bmatrix}.$$

From Equation (3.69), the corresponding minimum feedback gain is obtained as $\lambda^* = -0.227$. Hence, the resulting feedback controller is

$$K = \lambda^* k_u^* k_y^{*T} = \begin{bmatrix} -0.031 & 0.067 \\ -0.091 & 0.195 \end{bmatrix}. \quad (3.97)$$

Note that the optimization problem (3.78) has multiple solutions as, actually, $\phi^* = 0.333 + k\pi, k \in \mathbb{Z}$. This ambiguity affects the signs of k_u^* and k_y^* , which cancel out when multiplying the two vectors. Therefore, the resulting controller K is uniquely given by Equation (3.97).

Arbitrary Pole Placement

To illustrate the principle further, the absolute feedback gain $|\lambda|$ required for placing the conjugate complex pole pair at other locations in the complex plane is computed and depicted in Figure 3.7. As expected, $|\lambda|$ increases with the distance of the closed-loop pole from the open-loop pole. Additional solid lines in Figure 3.7 summarize the possible closed-loop pole locations which require the same zero z . The dashed line indicates the singular case $\omega_n \zeta = \omega_{n,cl} \zeta_{cl}$, which can be interpreted as $z = \infty$. For $z = 0$, the natural frequency remains constant and only the relative damping is affected. Note that Figure 3.7 shows only the positive imaginary part due to symmetry with respect to the real axis.

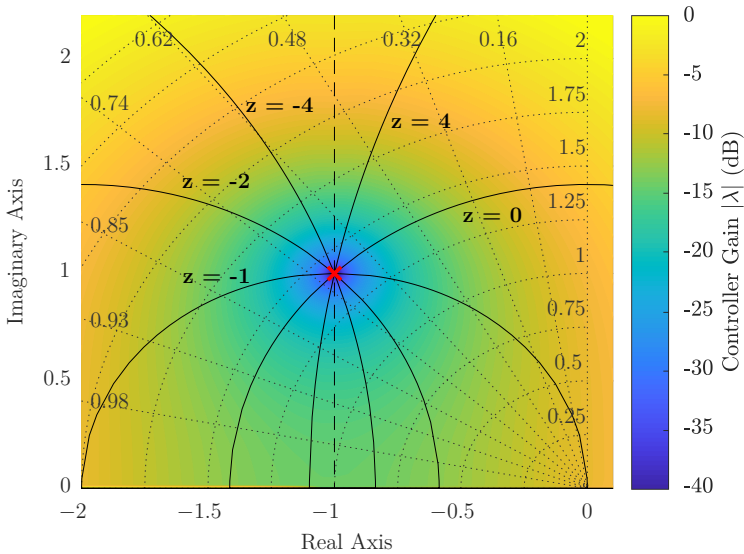


Figure 3.7: Illustration of the feedback gain magnitude $|\lambda|$ required for shifting the given pole (\times) in the complex plane. Constant values of the zero z introduced by blending inputs and outputs are marked as solid lines. The dashed vertical line indicates the singular case $z = \infty$.

Comparison of Different Controllability and Observability Measures

The developed pole placement algorithm computes blending vectors which place the zero z from Equation (3.66) at a specific location depending on the open- and closed-loop poles. An interesting question is now, where to place the zero z in order to maximize the different controllability and observability measures reviewed in Section 3.1.2. Considering the \mathcal{H}_2 norm as a corresponding measure, an optimal location of z is automatically obtained when applying the \mathcal{H}_2 -optimal blending vectors derived in Section 3.2. For other controllability and observability measures, more insight can be obtained by first computing optimal blending vectors for different values of z and then evaluating the corresponding measures. Note that this is enabled by the fact that blending vectors designed for placing the zero z at a predefined location always maximize the system gain $|r_1|$ of the blended mode, see Equation (3.71). This allows a numerical evaluation of the close relation of different modal controllability and observability measures as shown in the following example.

In what follows, five different controllability and observability measures are compared, which are all normalized such that they are within the interval $[0 \ 1]$. Considering the \mathcal{H}_2 , \mathcal{H}_∞ and Hankel (H) system norm, the corresponding measures are defined the same way as in Definition 3.7, i.e.,

$$\eta_{\square} = \frac{\|k_y^T M(s) k_u\|_{\square}}{\|M(s)\|_{\square}}, \quad (3.98)$$

where \square is a place holder for “ \mathcal{H}_2 ”, “ \mathcal{H}_∞ ” or “H” denoting the respective system norm. See Section 3.1.2 for the definition of the corresponding system norms. In addition to this, also the sum of the Hankel singular values is compared in terms of

$$\eta_{\Sigma_H} = \frac{\sum_{k=1}^{n_x} \sigma_{H,k}(k_y^T M(s) k_u)}{\sum_{k=1}^{n_x} \sigma_{H,k}(M(s))}, \quad (3.99)$$

where $\sigma_{H,k}(\bullet)$ denote the Hankel singular values of the place holder \bullet , which is an LTI system of order $n_x = 2$ in this case. Lastly, controllability and observability is evaluated in terms of the Litz dominance measure as

$$\eta_{\text{Litz}} = \frac{|k_y^T R k_u|}{\sum_{j=1}^{n_y} \sum_{l=1}^{n_u} |r_{jl}|}, \quad (3.100)$$

with r_{jl} denoting the entries of the residue $R \in \mathbb{C}^{n_y \times n_u}$ of $M(s) = \frac{R}{s-p} + \frac{\bar{R}}{s-\bar{p}}$. Note that in Equation (3.100), the Litz dominance measure of the blended mode is normalized by the sum of the individual Litz dominance measures of

the original mode, whereby $|p| = |\bar{p}|$ cancels out. See Definition 3.2 for more details on the Litz dominance measure.

The normalized controllability and observability measures introduced in Equations (3.98) to (3.100) are compared at the example mode $M(s)$ given in Equation (3.52). To that end, optimal blending vectors are first derived for different values of the zero z using the algorithm summarized in Section 3.3.4. Subsequently, the blending vectors are applied to $M(s)$ and the respective measures are computed. The results are depicted in Figure 3.8, where the zero $z^* = -1.43$ from \mathcal{H}_2 -optimal blending is marked with a vertical line. It can be seen that the different controllability and observability measures reach their maximum for different but almost identical values of z . This confirms the mostly qualitative comparison of the different controllability and observability measures from Section 3.2.4. An exception is η_{Litz} , which remains almost constant and even decreases slightly around z^* . However, this discrepancy reduces as expected when decreasing the magnitude of the relative damping $|\zeta|$, which is, with a value of $1/\sqrt{2}$, relatively large in this example. Note that for an undamped mode, the \mathcal{H}_2 -optimal blending vectors are also optimal in terms of the Litz dominance measure, see Section 3.2.4 for more details. Furthermore, it is noted that the almost equal values of the different measures for $z = 0$ are a special property of the given example and cannot be generalized.

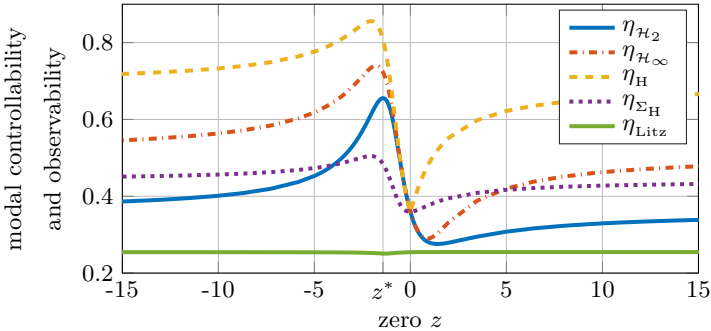


Figure 3.8: Comparison of modal controllability and observability measures for different values of the zero z .

3.4 Spillover Suppression

The blending-based control approaches derived in Sections 3.2 and 3.3 focus on individual modes to be controlled while residual modes are not considered. However, residual modes may still be excited and measured by the blended inputs and blended outputs, which is commonly known as spillover [121]. To avoid spillover, the modes to be controlled need to be well decoupled. This can be achieved by applying dynamic filters, where a sufficient separation in frequency of the targeted and the residual modes is required. Alternatively, it is proposed to exploit the shape of the residual modes and enforce the input and output blending vectors to be orthogonal on them.

3.4.1 Dynamic Filtering

In case the residual modes are well separated in frequency from the mode to be controlled, dynamic filtering allows suppressing an excitation or measurement of the residual modes. On the one hand, this can be achieved by a band-pass filter which emphasizes the frequency of the targeted mode while suppressing the residual modes. On the other hand, band-stop or notch filters can be used to explicitly suppress individual residual modes. Typically, both approaches require the frequencies of the corresponding modes to be well-known. If this is not the case, it is proposed, e.g., in [12], to use a phase-locked loop filter which identifies the frequency of a mode based on the phase of the system response. Note, however, that the phase-locked loop filter requires a sufficiently high signal-to-noise ratio besides well separated natural frequencies of the considered modes. For more advanced and adaptive filtering techniques see, e.g., [58, 88, 164].

Regarding blending vector design, it is required to first apply the respective spillover suppression filters and then carry out the modal decomposition for computing the corresponding blending vectors. This is important since the spillover suppression filters change the system dynamics from the controller point of view. To suppress an excitation or measurement of the residual modes, corresponding filters need to be added to each control input and measurement output. Thereby, it is typically sufficient to either filter the control commands or the measurement signals but not both. In case multiple modes are controlled, it is also important that the individual modal controllers do not interfere. This can be achieved by using a different set of spillover suppression filters for each modal controller, see Section 3.1.3 for more details. Note that in case a modal controller is designed using the same linear filter for each signal, the corresponding filter can be seen as a part of the SISO controller since individually filtering each signal is equivalent to filtering the blended signal.

3.4.2 Blending Vector Design with Explicit Mode Decoupling

In case controlled and residual modes are not well separated in frequency, it is proposed to suppress spillover by considering explicit mode decoupling constraints during blending vector design. More precisely, the input or output blending vectors $k_u \in \mathbb{R}^{n_u}$ or $k_y \in \mathbb{R}^{n_y}$ are enforced to be orthogonal on the input or output matrix B_r or C_r of the corresponding residual mode $M_r(s) = C_r(sI - A_r)^{-1}B_r$. The reasoning is that $M_r(s)$ is uncontrollable from a blended control input when

$$B_r k_u = 0 \quad (3.101)$$

and unobservable from a blended measurement output when

$$C_r^T k_y = 0. \quad (3.102)$$

For more details see the discussion on modal controllability and observability in Section 3.1.2. As a result, a set of residual modes $\{M_r(s)\}_{r=1}^{n_r} \subset \{M_i(s)\}_{i=1}^{n_i}$ is explicitly decoupled when augmenting the original blending vector design problems derived in Sections 3.2 and 3.3 with the constraints

$$\underbrace{[B_1^T \ \dots \ B_{n_r}^T]^T}_{R_u^T} k_u = 0, \quad (3.103)$$

$$\underbrace{[C_1 \ \dots \ C_{n_r}]^T}_{R_y^T} k_y = 0. \quad (3.104)$$

In other words, the blending vectors k_u and k_y are restricted to the null space of

$$R_u^T = [B_1^T \ \dots \ B_{n_r}^T]^T, \quad (3.105)$$

$$R_y^T = [C_1 \ \dots \ C_{n_r}]^T, \quad (3.106)$$

which collect the input and output matrices of the considered residual modes. If one of the null spaces is empty, i.e., $\text{rank } R_u = n_u$ or $\text{rank } R_y = n_y$, the decoupled blending vector design problem is infeasible. This also implies that for a finite number of inputs and outputs, the number of residual modes which can be made uncontrollable or unobservable is limited. Note, however, that for mode decoupling it may be sufficient to make the residual modes either uncontrollable or unobservable but not both.

In order to solve the blending vector design problem augmented with the mode decoupling constraints (3.103) and (3.104), the original optimization variables k_u and k_y are replaced by

$$k_u = N_u \hat{k}_u \quad \text{and} \quad k_y = N_y \hat{k}_y, \quad (3.107)$$

where N_u and N_y denote orthonormal bases of the null spaces of R_u^T and R_y^T , respectively. The blended mode then becomes

$$k_y^T M(s) k_u = \hat{k}_y^T \underbrace{N_y^T M(s) N_u}_{\hat{M}(s)} \hat{k}_u, \quad (3.108)$$

which means that the decoupling constraints are incorporated into blending vector design by simply replacing the original targeted mode $M(s)$ with $\hat{M}(s) = N_y^T M(s) N_u$. Solving the considered blending vector design problem for $\hat{M}(s)$ instead of $M(s)$ yields the optimal blending vectors \hat{k}_u^* and \hat{k}_y^* , from which the actual blending vectors $k_u^* = N_u \hat{k}_u^*$ and $k_y^* = N_y \hat{k}_y^*$ are then obtained according to Equation (3.107). Since N_u and N_y act as unitary linear transformations, neither the objective function nor the norm of the blending vectors is changed. Note that the null spaces for mode decoupling must be included before decomposing the mode by means of Lemma A.1 for the numerically efficient blending vector design algorithms proposed in Sections 3.2.4 and 3.3.2. Furthermore, it is noted that the additional mode decoupling constraints typically decrease the maximum achievable efficiency factor η defined in Equation (3.21) and thereby increase the required feedback gains. Hence, the designer must trade off the importance of decoupling from individual modes and the drawbacks associated with larger feedback gains.

Besides, the described procedure for mode decoupling may also be used to eliminate a non-zero feedthrough matrix $D \neq 0$. For this purpose, the right or left singular vectors of D need to be added as columns to R_u or R_y , respectively. As a result, $k_y^T D k_u^T = 0$, which means that direct feedthrough is successfully suppressed. Alternatively, the feedthrough term may also be directly subtracted from the computed control inputs as discussed in Section 3.1.3.

3.5 Handling Actuator Constraints using Control Allocation

In the case of actuator constraints like saturation or faults, controller performance may be degraded or, in the worst-case, the closed-loop may even become unstable. To counteract this, it is proposed to augment the existing blending-based controller with a control allocation scheme. In general, the objective of a control allocation algorithm is to compute a control input u from a virtual control command v_u which can be realized by the given set of actuators [72]. Assuming sufficient control authority, the input blending matrix K_u can hence be seen as a control allocation since it distributes v_u to u . However, this kind of *unconstrained* control allocation may be unrewarding if control authority is limited, i.e., the capability of the actuators is constrained. In that case, it is recommended to use *constrained* control allocation which also considers actuator constraints. Typically, the constrained control allocation problem is formulated as an optimization problem which is solved at each time sample. If the optimization problem is infeasible, i.e., the virtual control command cannot be realized adequately, controller performance is necessarily degraded, which is commonly described by a so-called slack variable.

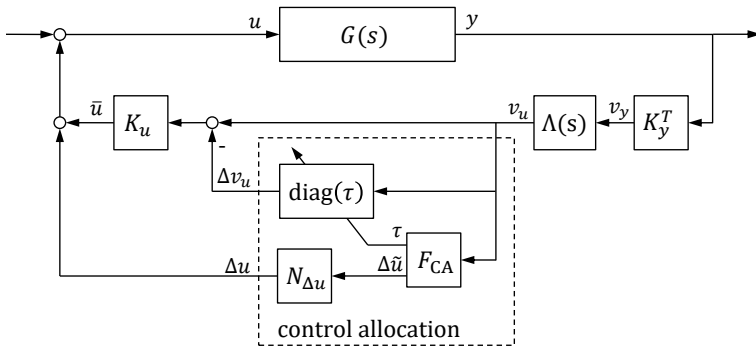


Figure 3.9: Closed-loop interconnection of plant with blending-based controller and control allocation.

The control allocation scheme proposed herein is depicted in Figure 3.9, where the nominal blending-based feedback controller is given according to Equation (3.19) as

$$K(s) = K_u \Lambda(s) K_y^T, \quad (3.109)$$

with $\Lambda(s)$ collecting on its diagonal the individual SISO controllers $\lambda_j(s)$, $j = 1, \dots, n_j$. The given scheme is a reformulation of the more common control allo-

cation scheme described, i.e., in [72] such that the augmentation of the blending-based nominal controller becomes clearly visible. In general, it is desired that the constrained control allocation is only active when the nominal control input $\hat{u} = K_u v_u$ exceeds the upper or lower actuator limit $u_{\min} \in \mathbb{R}_{\leq 0}^{n_u}$ or $u_{\max} \in \mathbb{R}_{\geq 0}^{n_u}$. If this is the case, a control input redistribution vector $\Delta u \in \mathbb{R}^{n_u}$ is added to the nominal control input \hat{u} such that the resulting control input is within actuator limits and nominal controller performance is not affected. In case no feasible Δu can be found, controller performance is degraded such that a feasible Δu exists, which is realized by reducing the virtual control command v_u by

$$\Delta v_u = \text{diag}(\tau) v_u = \begin{bmatrix} \tau_1 & \dots & 0 \\ \vdots & \ddots & \vdots \\ 0 & \dots & \tau_{n_j} \end{bmatrix} v_u. \quad (3.110)$$

In Equation (3.110), $\tau \in \mathbb{R}^{n_j}$ denotes the slack variable, where its elements $\tau_j \in [0 \ 1]$ indicate the relative performance degradation of the individual SISO controllers $c_j, j = 1, \dots, n_j$. This means that for $\tau_j = 1$, the respective SISO controller c_j is actually inactive and $\tau_j = 0$ denotes the nominal case without any performance degradation.

Eventually, the resulting control input is computed as

$$u = K_u v_u - K_u \text{diag}(\tau) v_u + \Delta u = \underbrace{\hat{u} - K_u \Delta v_u}_{\bar{u}} + \Delta u, \quad (3.111)$$

where \bar{u} denotes the reduced nominal control input. All in all, the described control allocation scheme features three different modes which are summarized in Table 3.1.

Table 3.1: Control allocation modes.

mode description	Δu	τ	control input
unconstrained (nominal control)	$= 0$	$= 0$	$u_{\min} \leq \hat{u} \leq u_{\max}$
redistribution only	$\neq 0$	$= 0$	$u_{\min} \leq \hat{u} + \Delta u \leq u_{\max}$
redistribution + performance reduction	$\neq 0$	$\neq 0$	$u_{\min} \leq \bar{u} + \Delta u \leq u_{\max}$

For computing a suitable control input redistribution Δu , the objective is that the redistribution vector should be minimal in terms of some p -norm, where p is typically chosen as 1 or 2. To maintain controller performance, Δu is enforced to be orthogonal on the input blending matrix K_u and hence on the nominal control input $\hat{u} = K_u v_u$. In case the input blending vectors are designed taking into account the mode decoupling constraints introduced in Section 3.4.2, it is

further desirable that Δu is also orthogonal on the input matrices B_r of all considered residual modes $M_r(s) = C_r(sI - A_r)^{-1}B_r$, $r = 1, \dots, n_r$. Additionally, it is also desired that the performance degradation is minimal, which is considered by further minimizing the p -norm of the slack variable τ . Eventually, the optimization problem for control allocation is formulated as

$$\begin{aligned}
 & \underset{\Delta u \in \mathbb{R}^{n_u}, \tau \in \mathbb{R}^{n_j}}{\text{minimize}} && \|W_u \Delta u\|_p + \|W_\tau \tau\|_p \\
 & \text{subject to} && 0 \leq \tau \leq 1 \\
 & && u_{\min} \leq u \leq u_{\max} \\
 & && \Delta u^T [B_1^T \ \dots \ B_{n_r}^T] = 0 \\
 & && \Delta u^T K_u = 0,
 \end{aligned} \tag{3.112}$$

where u is computed according to Equation (3.111). In Equation (3.112), the positive definite weighting matrices $W_u \in \mathbb{R}^{n_u \times n_u}$ and $W_\tau \in \mathbb{R}^{n_j \times n_j}$ are introduced in the objective function for balancing the priority of the individual control inputs and modal SISO controllers. Typically, both matrices are diagonal and W_τ is chosen much larger than W_u in order to prioritize redistribution over performance reduction. Besides, the constraint $0 \leq \tau \leq 1$ is considered in Equation (3.112) to ensure that controller performance is only decreased but not increased ($\tau > 0$) or even “inverted” ($\tau < 0$). Note that to ensure a feasible solution, it is required that $u_{\min} \leq 0$ and $u_{\max} \geq 0$, because in that case a feasible solution can always be obtained by turning off the controller setting $\tau = 1$ and $\Delta u = 0$. To further consider actuator faults, the actuator constraints $u_{\min} \leq u \leq u_{\max}$ are commonly adapted in real-time [72], e.g., by setting the upper and lower limits of a faulty actuator to zero. This ensures that the faulty actuator is not used and the desired control commands are redistributed.

In order to efficiently solve the optimization problem (3.112), the given equality constraints are eliminated by substituting the control input redistribution as

$$\Delta u = N_{\Delta u} \Delta \tilde{u}, \tag{3.113}$$

where $N_{\Delta u} \in \mathbb{R}^{n_u \times n_{\tilde{u}}}$ denotes an orthonormal basis of the null space of

$$R^T = [K_u \ B_1 \ \dots \ B_{n_r}]^T. \tag{3.114}$$

Note that if $\text{rank } R = n_u$, its null space is empty and redistribution is not possible, i.e., $\Delta u = 0$ for all times, which implies that the system is not sufficiently over-actuated. With $\Delta \tilde{u}$ as a new optimization variable, the original

optimization problem (3.112) is turned into

$$\begin{aligned}
 & \underset{\Delta \tilde{u} \in \mathbb{R}^{n_{\tilde{u}}}, \tau \in \mathbb{R}^{n_j}}{\text{minimize}} && \|W_u N_{\Delta u} \Delta \tilde{u}\|_p + \|W_\tau \tau\|_p \\
 & \text{subject to} && u_{\min} \leq u \leq u_{\max} \\
 & && 0 \leq \tau \leq 1.
 \end{aligned} \tag{3.115}$$

In case $p = 1$, Equation (3.115) represents a linear program which can be solved efficiently by using, e.g., the simplex method [110]. In case $p = 2$, a quadratic program is obtained which is convex and hence can be solved efficiently by using, i.e., interior-point methods [22]. In general, the 2-norm minimization tends to use a large number of actuators to a smaller degree in comparison to a 1-norm minimization, which commonly favors the use of a smaller number of actuators but to a higher degree [19]. Furthermore, it is noted that uniqueness of a feasible solution is usually only guaranteed when formulating the objective function in terms of the 2-norm [72].

4 Modeling Aeroelastic Systems

In general, aeroelastic systems like highly flexible aircraft are described by an interconnection of aerodynamic, elastic and inertial forces. This so-called aeroelastic triangle of forces is depicted in Figure 4.1 and named after Arthur Roderick Collar [24]. To compute the individual forces, models of the aerodynamics and the structural dynamics are derived and subsequently interconnected. Also adding sensor equations and actuator models, an integrated aeroelastic model for controller synthesis is obtained featuring multiple control inputs and measurement outputs. The overall aeroelastic modeling procedure used herein is taken from common literature as [17, 133, 144] and summarized as follows.

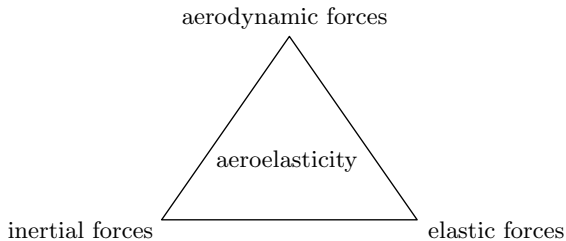


Figure 4.1: Collar's aeroelastic triangle of forces.

4.1 Structural Dynamics Model

The dynamics of the flexible structure are described by a finite element (FE) model, where each node features up to three translational and three rotational degrees of freedom (DOF). The corresponding model equations are given as

$$G_{\text{strc}}(s) = \frac{1}{M_{\text{strc}}s^2 + B_{\text{strc}}s + K_{\text{strc}}}, \quad (4.1)$$

where M_{strc} , B_{strc} and K_{strc} denote the mass, damping and stiffness matrix of the FE model. Note that the damping matrix B_{strc} is often poorly known and hence assumptions like the Rayleigh damping [131] are typically applied. Since FE models are usually of very large dimension, they are commonly reduced by

Guyan reduction [53] and modal truncation [102]. For modal truncation, a modal decomposition, also called modal analysis, is carried out. Taking into account the assumptions from [162], the thereby obtained structural modes can be divided into rigid-body and flexible modes. This allows describing the decoupled rigid body motions also with a different set of equations, which may be required in case of large amplitudes. For instance, it is recommended to describe the rigid-body motions of flexible aircraft by the nonlinear equations of motions from flight mechanics when performing extreme flight maneuvers [79]. Note that the structural modes described here are not to be confused with aeroelastic modes, which are obtained by carrying out a modal decomposition on the full aeroelastic model and generally contain contributions from numerous structural modes. For more insights on modeling of flexible structures in general and of aircraft, see, e.g., [103] and [144], respectively.

4.2 Aerodynamics Model

The aerodynamics are modeled in frequency domain using the doublet lattice method (DLM) [3]. The DLM captures both steady and unsteady aerodynamics and discretizes the lifting surfaces by so-called aerodynamic panels. The derived aerodynamics model $Q_{\text{aero}}(s)$ computes the aerodynamic loads caused by the surrounding airflow, which includes contributions from the structural displacements x_{strc} and the flap deflections δ_{flap} . To also consider gusts, the gust field is evaluated at each aerodynamic panel and the orthogonal components, normalized by the free stream velocity v_∞ , are collected in w_{gust} . Based on that, the overall aerodynamic loads acting on the structural nodes are given as

$$p_{\text{aero}} = \underbrace{\begin{bmatrix} Q_{\text{gust}}(s) & Q_{\text{flap}}(s) & Q_{\text{strc}}(s) \end{bmatrix}}_{Q_{\text{aero}}(s)} \begin{bmatrix} w_{\text{gust}} \\ \delta_{\text{flap}} \\ x_{\text{strc}} \end{bmatrix},$$

with $Q_{\text{aero}}(s)$ depending on the velocity, Mach number and dynamic pressure of the free stream. Assuming that the gust field is one dimensional and orthogonal to the free stream velocity, the normalized gust velocity of the foremost panel $w_{\text{gust}}^{(0)}$ can be delayed for the panels further downstream yielding

$$w_{\text{gust}} = \underbrace{\begin{bmatrix} e^{-\frac{\Delta x_1}{v_\infty} s} & \dots & e^{-\frac{\Delta x_{n_p}}{v_\infty} s} \end{bmatrix}^T}_{G_{\text{delay}}(s)} w_{\text{gust}}^{(0)},$$

where Δx_p , $p = 1, \dots, n_p$ denotes the distance from the foremost panel to the panel p in downstream direction. Thereby, the high-dimensional gust input w_{gust} can be replaced by the scalar gust input $w_{\text{gust}}^{(0)}$, which decreases the computational effort for gust simulations. In order to realize the aeroelastic model in

state space, e.g., for controller design, rational function approximations are carried out on $G_{\text{delay}}(s)$ and $Q_{\text{aero}}(s)$. For the gust delay model $G_{\text{delay}}(s)$, Padé approximation is typically used, where the resulting model order can be reduced by grouping the aerodynamic panels in zones [78]. Thereby, it is worth to mention that the simplest but least accurate way to model a gust input is to consider only a single gust zone, i.e., that the gust acts at all aerodynamic panels simultaneously. For the aerodynamics model $Q_{\text{aero}}(s)$, a well-established and reliable method has been proposed by Roger [135], which usually yields models of relatively high order. To avoid this, different low-order approximations have been proposed, e.g., in [77] or [130]. In any case, a careful balancing between model order and model accuracy is required as discussed, e.g., in [76] and [80].

4.3 Actuators and Sensors

The actuators driving the flaps are typically identified separately and the derived transfer functions are collected on the diagonal of $G_{\text{flap}}(s)$. In doing so, the actual flap deflections are computed as

$$\delta_{\text{flap}} = G_{\text{flap}}(s) \delta_{\text{flap}}^{(\text{cmd})}, \quad (4.2)$$

where $\delta_{\text{flap}}^{(\text{cmd})}$ denotes flap deflections commanded by the control system. Note that the actuator model $G_{\text{flap}}(s)$ commonly includes delays from signal processing and features a low-pass characteristic introduced by the physical inertia of the actuator and flap.

For feedback control, the system response to external disturbances like gusts needs to be measured. Commonly, this includes measurements of rotational rates y_{rate} and translational accelerations y_{acc} at different locations on the structure and in different spatial directions. Furthermore, strain gauges are installed to verify the structural loads y_{load} with and without active control. The individual measurements are summed up in

$$y_{\text{meas}} = \begin{bmatrix} y_{\text{load}} \\ y_{\text{rate}} \\ y_{\text{acc}} \end{bmatrix} = \underbrace{\begin{bmatrix} T_{\text{load}} K_{\text{strc}} \\ T_{\text{rate}} s \\ T_{\text{acc}} s^2 \end{bmatrix}}_{G_{\text{meas}}(s)} x_{\text{strc}} \quad (4.3)$$

and depend on the displacements x_{struct} of the structural model as well as its derivatives. Note that x_{struct} captures both rigid-body motions and the flexible deformations of the aircraft structure as described in Section 4.1. In Equation (4.3), the matrices T_{rate} and T_{acc} describe a transformation from the nodal to the corresponding sensor coordinate system(s). The cut loads at a certain cross section $y_{\text{load}} = T_{\text{load}} K_{\text{strc}} x_{\text{strc}}$ are obtained by summing up the nodal

loads $K_{\text{strc}}x_{\text{strc}}$ using the linear transformation matrix T_{load} . Note that the nodal loads are computed here using the so-called *mode displacement method* and may also be computed using, e.g., the well-known *force summation method*. See [17] or [41] for more details and comparative studies. Besides the measurements of the aircraft response y_{meas} , the velocity of the free stream is typically also measured and used for control. Thereby, it is worth to mention that common conventions for qualifying free stream velocity are true airspeed, equivalent airspeed, calibrated airspeed and indicated airspeed. Note that the different types of airspeed can easily be computed from each other assuming that parameters like air density or instrument error are known, see, e.g., [51] for more details.

4.4 Model Integration

In order to obtain the integrated aeroelastic model, the structural dynamics model from Section 4.1 is coupled with the aerodynamics model from Section 4.2. This is achieved by setting

$$p_{\text{ext}} = p_{\text{aero}} + p_{\text{other}},$$

where p_{other} summarizes any other loads acting on the structure, e.g. from engines, landing gears, clamping, aerodynamic drag or gravitation. Furthermore, the actuator dynamics and measurement equations described in Section 4.3 are considered in the integrated model. The resulting interconnection of the individual models is depicted in Figure 4.2. The described modeling procedure is used in the following chapter for deriving accurate models of the aeroelastic systems considered to demonstrate the effectiveness of the proposed blending-based modal control approaches.

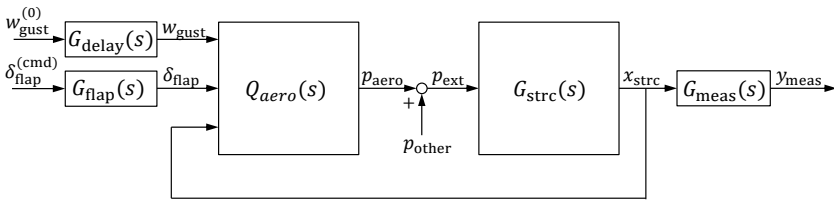


Figure 4.2: Integrated aeroelastic model.

5 Application to Aeroelastic Systems

In this chapter, the blending-based control approaches introduced in Chapter 3 are applied to three different aeroelastic systems. To that end, detailed aeroelastic models of the considered systems are derived using the modeling procedure described in Chapter 4. As a first aeroelastic system, a large transport aircraft is considered for which a gust load alleviation (GLA) system is designed in order to reduce structural loads during gust encounters. For comparison reasons, both the \mathcal{H}_2 -optimal blending approach and the blending-based pole placement approach are applied with the goal to increase the damping of the highly flexible aircraft structure. Secondly, the operational velocity range of an UAV is successfully extended by actively suppressing flutter, demonstrating the applicability of the \mathcal{H}_2 -optimal blending approach to unstable systems. Finally, an actively controlled flexible wing is tested in a wind tunnel, where the blending-based control law includes control allocation to consider actuator limitations and faults. Furthermore, it is noted that parts of this chapter were published in separate research articles [30, 31, 115, 123, 127, 128, 151, 167].

5.1 Active Gust Load Alleviation for a Large Transport Aircraft

In this section, the blending-based control approaches proposed in Chapter 3 are applied to a large transport aircraft in order to reduce its structural loads during gust encounters. This is also known as active GLA and considered as a key technology to improve the performance of next-generation aircraft [132]. The twin-engined transport aircraft taken into account is originally designed within the DLR project Digital-X [84] and augmented as described in [123]. The highly flexible wings of the aircraft feature a span of 58 m and are sensitive to external disturbances like gusts. In comparison to conventional transport aircraft, the considered aircraft is equipped with an increased number of sensors and control surfaces. This allows for better control of the aircraft and its flexible deformations but also leads to new challenges in controller design. To handle the large number of control inputs and measurement outputs, the \mathcal{H}_2 -optimal blending approach and the blending-based pole placement approach from Chapter 3 are applied and compared. To that end, a high-dimensional aeroelastic model of the transport aircraft is derived as described in Section 5.1.1. The loads dominating aeroelastic modes are systematically identified and isolated by means of blending control inputs and measurement outputs. Thereby, the same mode

decoupling constraints are considered for both blending approaches to ensure comparability. The isolated modes can then be individually damped by separate SISO controllers, which are designed and tuned in a systematic way taking into account actuator constraints and robustness requirements. The two different controller designs are described in Section 5.1.2, where the achieved load reduction is thoroughly evaluated in Section 5.1.3 considering different gust excitations. The encouraging results reveal the suitability of the proposed blending-based control approaches for active GLA, especially when a large number of measurements and control surfaces is available.

5.1.1 Aircraft Modeling and Analysis

The considered large transport aircraft is modeled according to Chapter 4. To that end, the aircraft is discretized by 2998 aerodynamic panels and 133 structural nodes, which are both depicted in Figure 5.1. To control the highly flexible

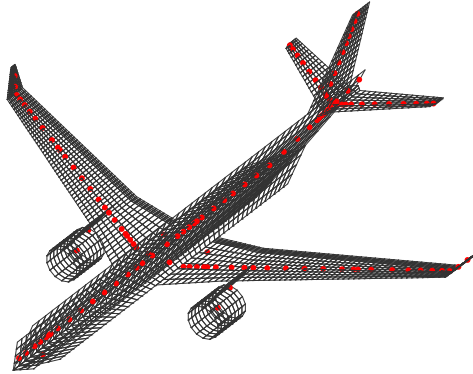


Figure 5.1: Discretized aircraft model with aerodynamic boxes (black) and structural nodes (red).

aircraft, it features a pair of elevators and 9 equally distributed control surfaces on the trailing edge of each wing. The actuator of each control surface is approximated by a second-order Butterworth low pass filter with a cutoff frequency of $\omega_c = 40$ rad/s. The response of the flexible aircraft is captured by 11 distributed inertial measurement units (IMUs), where 2 IMUs are located on the tips of the horizontal tail plane (HTP), 3 IMUs are located on each wing and 3 IMUs are located along the fuselage. Each of the IMUs measures rotational rates and translational accelerations in three spatial directions, resulting in 66

measurement signals available for feedback control. Furthermore, strain gauges are placed at the wing root in order to monitor structural loads and validate the GLA controller performance. The location of the strain gauges, the IMUs and control surfaces are depicted in Figure 5.2. Additionally, a vertical gust input is

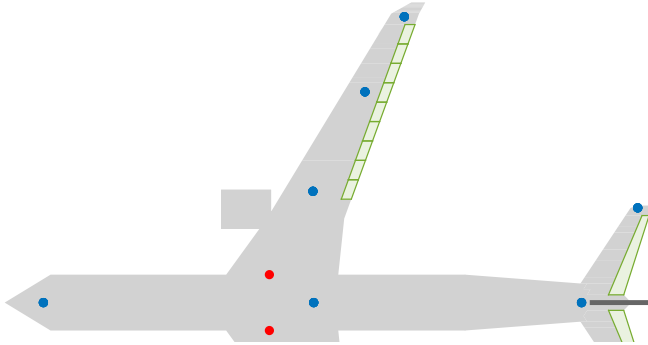


Figure 5.2: Location of control surfaces (□), inertial measurement units (●) and strain gauges (●).

modeled by grouping aerodynamic panels into 30 zones in the direction of flight, where the time delay for each zone is modeled using Padé approximations.

For GLA controller design, a single flight point at an altitude of 9108 m and Mach 0.86 is taken into account, where an international standard atmosphere [69] is assumed. At this flight point, gust encounters cause the maximum wing root bending moment (WRBM), which is known to be a major driver for wing sizing [85]. Herein, only symmetric vertical gust encounters are considered, meaning that the gusts and hence the resulting aircraft response are equal on the left- and right-hand side of the aircraft. Thus, all asymmetric structural modes can be discarded without loss of modeling accuracy. Eventually, a linear longitudinal aircraft model with 264 states is obtained.

Carrying out a modal decomposition on this model, the corresponding aeroelastic modes are obtained, where the first seven modes are listed in Table 5.1. As it is typical for highly flexible aeroelastic systems, all modes besides the rigid-body modes are very lightly damped and the spacing between the respective frequencies is small. In the longitudinal aircraft model given here, only one rigid body mode is present which describes a rapid pitching motion and is commonly denoted as “short period mode”. In general, the coupling of airspeed and flight altitude is described by another rigid-body mode commonly known as “phugoid mode”, which is neglected here since its contribution to the WRBM is minor and a constant airspeed is assumed.

In order to determine the aeroelastic modes which have a large contribution to the WRBM, a modal dominance measure based on the \mathcal{H}_2 norm is introduced. To that end, $M_i^{d \rightarrow p}$ is defined as the transfer function of a single aeroelastic mode i from the vertical gust input to the WRBM output, or in general terms, from the disturbance inputs d to the performance outputs p . Based on that, the dominance of each mode is quantified by $\|M_i^{d \rightarrow p}\|_{\mathcal{H}_2}$, where the \mathcal{H}_2 norm is used in a similar manner as for the evaluation of the combined controllability and observability in Section 3.2.1. Considering the given aeroelastic modes, the first and second wing bending mode are the most dominant ones as expected and given in Table 5.1. Note that in Table 5.1, the transfer function $M_i^{d \rightarrow p}$ is normalized by the \mathcal{H}_2 norm of the 1st wing bending mode $\|M_2^{d \rightarrow p}\|_{\mathcal{H}_2}$. The respective modal dominances can also be recognized in the open-loop frequency response from the vertical gust input to the WRBM output in Figure 5.7 in Section 5.1.3. This frequency response check ensures that individual modes do not cancel out in the overall system response as described, e.g., in [89]. For the purpose of GLA, it is hence desired to actively damp the two wing bending modes, which is described in the following subsection.

Table 5.1: Symmetric aeroelastic modes in the frequency range of interest.

i	mode name	$\omega_{n,i}$ (rad/s)	ζ_i (-)	$\ M_i^{d \rightarrow p}\ _{\mathcal{H}_2}$	objective
1	short period	1.6	0.42	0.167	decouple
2	wing bending (1 st)	10.9	0.12	1.000	damp
3	fuselage bending	15.6	0.03	0.033	-
4	engine	18.4	0.03	0.019	-
5	wing transverse	21.9	0.03	0.067	decouple
6	wing bending (2 nd)	25.2	0.05	0.175	damp
7	HTP bending	34.4	0.05	0.038	decouple

5.1.2 Gust Load Alleviation Controller Design

The goal of the GLA system is to increase the relative damping of the first and second wing bending mode and thereby reduce the WRBM during gust encounters. To that end, the \mathcal{H}_2 -optimal blending approach from Section 3.2 and the blending-based pole placement approach from Section 3.3 are used and compared. In both control approaches, the inputs and outputs of the underlying system are blended such that each of the two bending modes is isolated and can be individually controlled by a SISO controller.

Blending of Inputs and Outputs

Before actually blending inputs and outputs, the measurement signals are normalized as proposed in Section 3.2.4 as they are of different units. Furthermore, it is desired to adequately isolate the targeted modes, which is achieved by applying the mode decoupling constraints introduced in Section 3.4.2. For the given aeroelastic model, however, a full mode decoupling cannot be achieved since the number of control inputs and measurement outputs is smaller than the number of states. Nevertheless, most of the given aeroelastic modes feature a minor controllability and observability and hence, it is acceptable to decouple the two bending modes only from the short period, the wing transverse, and the HTP bending mode. Thereby, it is sufficient to either make the three modes uncontrollable from the virtual inputs or unobservable from the virtual outputs. Here, the latter is chosen since the number of measurements is much larger than the number of control surfaces. In doing so, a larger blending efficiency factor η , defined in Equation (3.21), is obtained, resulting in a smaller feedback gain required for a certain damping increase. Besides, the short period mode must not be excited by the GLA system in order to maintain adequate handling qualities. To that end, the short period mode is not only made unobservable but also made uncontrollable when applying the blending vectors. In that way, it is not only ensured that the dynamics of the short period mode are maintained, i.e., the underlying pole pair is not moved, but also that it is not excited at all by the GLA system. In addition to that, the resulting virtual inputs and virtual outputs also need to be decoupled from each other to enable individually controlling the modes they are dedicated to. This is achieved by enforcing the input and output blending vectors associated with one mode to be orthogonal on the input and output pole vectors of the other mode.

Considering that the damping of both bending modes should be increased without affecting their natural frequency, the goal for blending-based pole placement is to find blending vectors which place the zero z in the origin. See Equation (3.66) in Section 3.3.1 for more details. In comparison to that, the \mathcal{H}_2 -optimal blending vector design places the zero z of the blended mode such that the blending efficiency factor η becomes maximum. Consequently, the η obtained from \mathcal{H}_2 -optimal blending always yields the largest achievable η and hence is considered as an upper bound. The resulting efficiency factors are compared in Table 5.2, where the expected degradation of η when enforcing mode decoupling can also be seen.

Taking into account mode decoupling, the resulting efficiency factors from \mathcal{H}_2 -optimal blending are approximately twice as big as the ones from the blending-based pole placement. This is also visible in Figure 5.3, where the frequency responses from the virtual inputs to the virtual outputs, each one dedicated to one of the targeted modes, also differ by a similar factor. The peaks at the

Table 5.2: Comparison of blending efficiency factor η .

aeroelastic mode mode decoupling	1 st bending		2 nd bending	
	yes	no	yes	no
\mathcal{H}_2 -optimal blending	0.23	0.96	0.20	0.93
blending-based pole placement	0.11	0.13	0.10	0.14

natural frequency of the first and second wing bending mode indicate a good controllability and observability of the respective mode while the contribution of other nearby modes is negligibly small. Additionally, the virtual input of one mode is hardly measurable by the virtual output of the other mode, as required for independent mode control. The achieved decoupling can also be examined in terms of invariant zeros which are placed at the location of the poles which should not be affected when closing the loop. To illustrate this, the corresponding pole-zero maps are plotted in Figure 5.6 in Section 5.1.2 for both blending approaches.

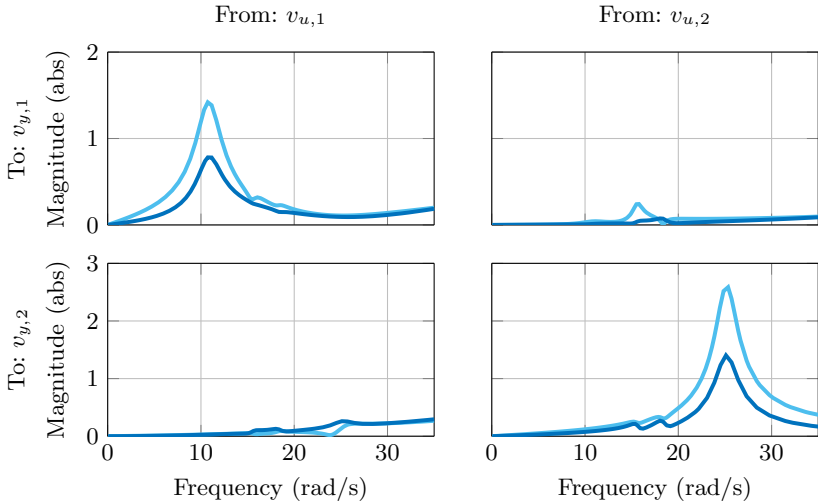


Figure 5.3: Frequency response from virtual inputs $v_{u,j}$ to virtual outputs $v_{y,j}$ for the 1st ($j = 1$) and 2nd ($j = 2$) wing bending mode, comparing \mathcal{H}_2 -optimal blending (—) and blending-based pole placement (—).

SISO Controller Design for Modal Damping

Herein, the goal of reducing the structural loads during gust encounters is translated to increasing the damping of the loads dominating first two wing bending modes. To this end, the input and output blending vectors k_u and k_y , designed for controlling the mode $M(s)$, are applied to the full order system $G(s)$, which approximately yields

$$k_y^T G(s) k_u \approx k_y^T M(s) k_u = \frac{\alpha s + \beta}{s^2 + 2\zeta\omega_n s + \omega_n^2}, \quad (5.1)$$

with $\alpha \in \mathbb{R}$ and $\beta \in \mathbb{R}$. In other words, $M(s)$ is well decoupled from $G(s)$ allowing for an individual mode control using a SISO controller. Hence, the original MIMO controller design problem becomes SISO one, where in this case, the objective is to increase the relative damping ζ without affecting the natural frequency ω_n of $M(s)$.

Considering the blending-based pole placement approach, the zero $z = -\beta/\alpha$ is placed in the origin as described in the previous Section 5.1.2. This allows increasing modal damping by means of a proportional feedback controller $\gamma \in \mathbb{R}$, which can be directly determined for a desired damping increase from Equation (3.96). Here, however, γ is considered as a free tuning parameter since the damping increase is not known but rather subject to being maximized under the constraints described below. In comparison to that, the \mathcal{H}_2 -optimal input and output blending yields a zero $z \neq 0$ for both targeted modes. In that case, modal damping can be increased by the proportional-derivative controller $\lambda(s) = \gamma(s + \alpha\omega_n^2/\beta)$ as described in Appendix A.2. Since the respective derivative term yields an undesired high-frequency amplification, it is commonly approximated as $s \approx s/(Ts + 1)$, where here $T = 5$ ms is chosen here. Based on that, the proposed SISO controller for damping the decoupled mode (5.1) is given as

$$\lambda(s) = \begin{cases} \gamma \left(\frac{s}{Ts + 1} + \frac{\alpha\omega_n^2}{\beta} \right) & \text{if } \beta \neq 0 \text{ (}\mathcal{H}_2\text{-optimal blending)} \\ \gamma & \text{if } \beta = 0 \text{ (blending-based pole placement),} \end{cases}$$

where $\gamma \in \mathbb{R}$ is considered as a free tuning parameter. Note that even if the gain γ is tuned, it is always considered as minimal for achieving a certain damping increase since this is guaranteed by the computed blending vectors.

For SISO controller tuning, the objective is to maximize the damping of the corresponding targeted mode taking into account robustness requirements and actuator limitations. To that end, the robustness of the control loop is evaluated in terms of the symmetric disk margin [18], which is computed at each of the multiple inputs and multiple outputs (loop-at-a-time). As a minimum requirement, a 45° phase margin is demanded, which is equivalent to a 7.7 dB

gain margin. Furthermore, control surface deflections and deflection rates are restricted to $\pm 5^\circ$ and $\pm 50^\circ/\text{s}$, respectively. To ensure that these limitations are not exceeded, time domain simulations for severe gust encounters are carried out in Section 5.1.3. In general, a higher feedback gain γ yields a higher damping of the corresponding targeted mode. Hence, the goal is to find the largest γ still fulfilling the robustness requirements and control surface deflection constraints, which are actually less restricting than the robustness constraints. For computing the minimum robustness margins, each control loop can be evaluated separately since the targeted modes are well decoupled. To confirm that this is legitimate, the minimum symmetric disk margins of the individual control loops are compared to the ones of the entire control loop, which are almost equal.

As a result, the two SISO controllers for damping the 1st and 2nd bending mode can be tuned manually and independently of each other. To that end, the minimum disk phase margins of each modal control loop are plotted over γ in Figure 5.4, where both blending approaches are compared. Considering the 45° phase margin requirement, a higher feedback gain and hence damping is possible for the 1st wing bending mode compared to the 2nd wing bending mode. This can also be seen in Figure 5.5, where the relative damping ζ is

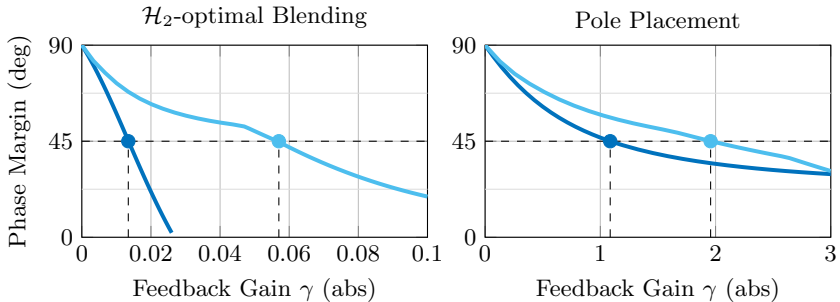


Figure 5.4: Minimum loop-at-a-time disk phase margin when individually damping the 1st (—) and 2nd (—) wing bending mode. The selected feedback gains are marked with a dot.

plotted over the feedback gain γ . For both blending approaches, the damping ζ of the two targeted modes is more than doubled when closing the loop, where the blending-based pole placement yields the better results as summarized in Table 5.3. The damping increase of the 1st and 2nd wing bending mode is also visible in Figure 5.6, where the poles of the open- and closed-loop system are compared. On the contrary, the residual modes are not, respectively barely, affected when closing the loop. Plotting the frequency response from the vertical

Table 5.3: Relative damping increase when closing the loop.

	1 st wing bending	2 nd wing bending
\mathcal{H}_2 -optimal blending	+154%	+114%
blending-based pole placement	+174%	+159%

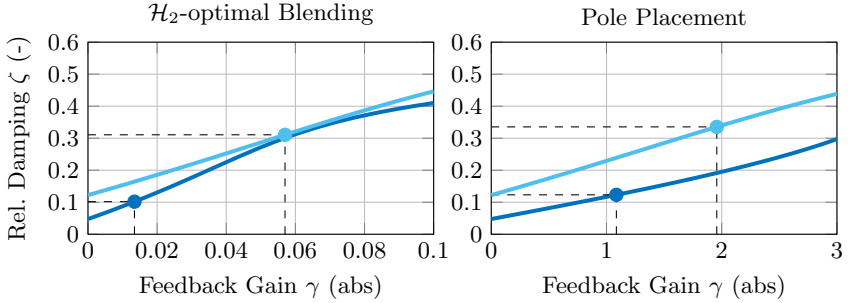


Figure 5.5: Relative damping of the 1st (—) and 2nd (—) wing bending mode when closing the loop. The selected feedback gains are marked with a dot.

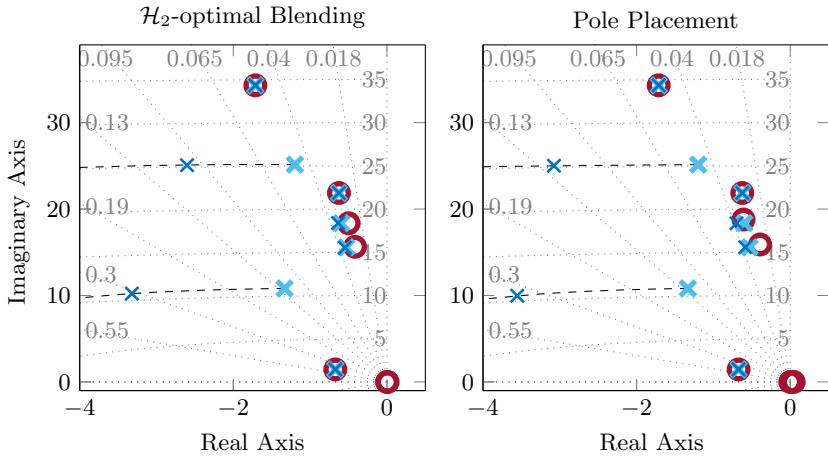


Figure 5.6: Open-loop (x) and closed-loop (x) poles, and invariant zeros (o) of the longitudinal aircraft model with blended inputs and outputs.

gust input to the WRBM output in Figure 5.7, the effect of the modal damping increase on the WRBM can be seen. While the low frequency range, covering the short period mode, is hardly affected, the resonance peaks of the 1st and 2nd wing bending mode are clearly reduced. This gives reason to expect a considerable WRBM reduction during gust encounters, which is validated in the following subsection.

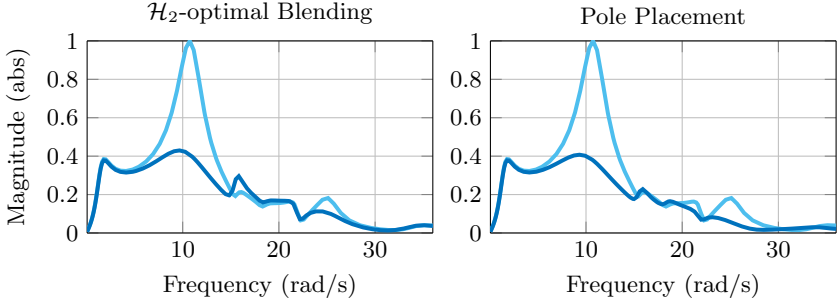


Figure 5.7: Comparison of open-loop (—) and closed-loop (—) frequency response from vertical gust input to wing root bending moment output (normalized).

5.1.3 Controller Validation

In order to validate the designed GLA controller, stochastic and discrete gust excitations are considered, which are taken from the certification requirements for large transport aircraft [36, 38]. For stochastic gust excitations, the normalized vertical gust velocity $w_{\text{gust}}^{(0)} = G_{\text{Dryden}}(s)w$ is generated by filtering white noise w with a Dryden form filter [61] given as

$$G_{\text{Dryden}}(s) = \frac{\sigma}{v_{\infty}} \sqrt{\frac{L}{v_{\infty}}} \frac{1 + \sqrt{3} \frac{L}{v_{\infty}} s}{\left(1 + \frac{L}{v_{\infty}} s\right)^2}. \quad (5.2)$$

Therein, the scale length $L = 533.4$ m, the free stream velocity $v_{\infty} = 260.86$ m/s, and the (severe) turbulence intensity $\sigma = 6$ m/s depend on the current flight point and are selected according to [106]. The Dryden form filter (5.2) features a low-pass characteristic with a cut-off frequency of around 0.5 rad/s as depicted in Figure 5.8(a).

For discrete gust excitations, the “1-cos” gust model described in [61] is used, which is given as

$$w_{\text{gust}}^{(0)}(t) = \begin{cases} \frac{v_{\text{ds}}}{2v_{\infty}} \left(1 - \cos\left(\frac{v_{\infty}}{H} \pi t\right)\right) & \text{if } 0 \leq t \leq \frac{2H}{v_{\infty}} \\ 0 & \text{otherwise,} \end{cases} \quad (5.3)$$

where the gust design speed v_{ds} depends on the current flight point, the gust length H and aircraft parameters like the maximum takeoff weight. According to the certification requirements [36, 38], the airframe must withstand gust lengths between 9 m and 107 m. For controller validation, nine different “1-cos” gusts of different length, which are plotted in Figure 5.8(b), are considered. In

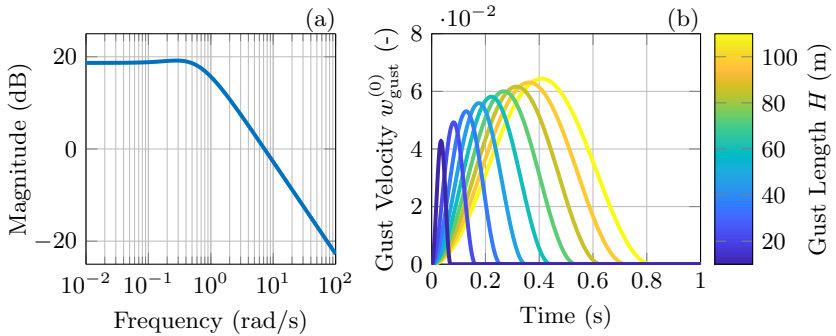


Figure 5.8: Dryden filter in (a) and “1-cos” gusts in (b) considered for controller validation.

order to quantify the achieved WRBM reduction for “1-cos” gust encounters, the maximum peak values of the resulting WRBM are computed. In comparison to that, the WRBM reduction during Dryden gust excitation is quantified in terms of the expected WRBM variance. For both excitation types, the blending-based pole placement approach performs better than the \mathcal{H}_2 -optimal blending approach as it can be seen in Table 5.4. This was to be expected since a higher modal damping is achieved with the blending-based pole placement approach as discussed in Section 5.1.2.

Furthermore, the maximum control surface deflection and deflection rates for the considered “1-cos” gusts are evaluated and summarized in Table 5.5. It can be seen that for these extreme excitations, the actuator limits of $\pm 5^\circ$ and $\pm 50^\circ/\text{s}$ are not exceeded. The length of the worst-case “1-cos” gust causing the largest WRBM is determined as $H = 94.5$ m. For this gust, the open- and

closed-loop response of the WRBM and pitch rate are compared in Figure 5.9. The responses are almost identical for both blending approaches and it can be seen that the pitch rate is hardly affected by the GLA control system. This is a direct result of the explicit decoupling of the short period mode and of great importance since the pitch rate is already controlled by the flight control system. Furthermore, not only the peaks but also undesired oscillations of the WRBM are clearly reduced. Summing up, both blending approaches show good GLA capabilities, where the blending-based pole placement approach yields a better robustness allowing for a slightly higher load reduction performance.

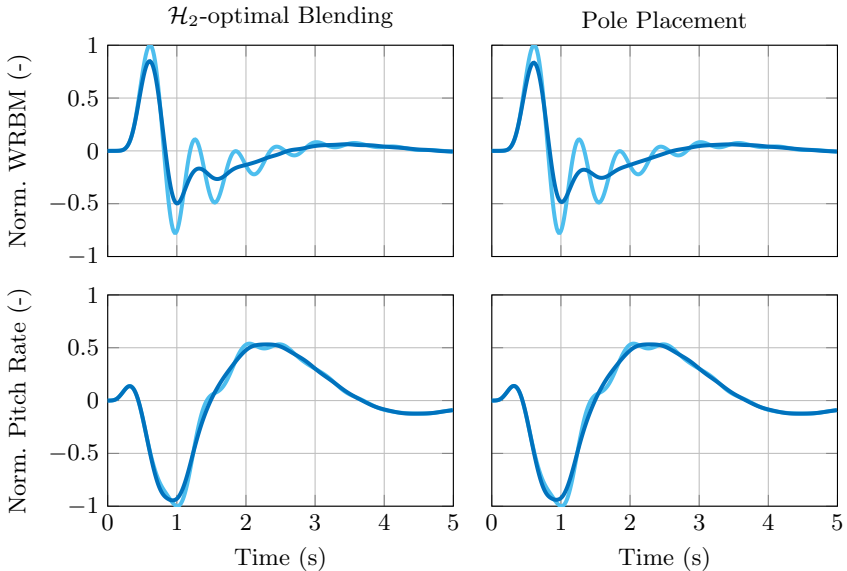


Figure 5.9: Normalized wing root bending moment (top) and pitch rate (bottom) for the worst-case “1-cos” gust excitation with $H = 94.5$ m in the open-loop (—) and closed-loop (—) case using \mathcal{H}_2 -optimal blending (left) and blending-based pole placement (right).

Table 5.4: Reduction of the wing root bending moment for different gust models.

	“1-cos” (peak)	Dryden (variance)
\mathcal{H}_2 -optimal blending	-15.1 %	-11.2 %
blending-based pole placement	-16.6 %	-11.7 %

Table 5.5: Maximum deflections and deflection rates of control surfaces for the considered “1-cos” gust excitations.

	max. deflection	max. deflection rate
\mathcal{H}_2 -optimal blending	4.8°	41.9 °/s
blending-based pole placement	4.6°	41.9 °/s

5.1.4 Conclusions

For the considered large transport aircraft, both the \mathcal{H}_2 -optimal blending approach and the blending-based pole placement approach achieve an excellent GLA performance. Blending the numerous control inputs and measurement outputs, the loads dominating modes are well isolated from the high order aeroelastic model. Thereby, an individual SISO controller design for damping each targeted mode is enabled, where the respective controller parameters can be tuned manually since they hardly interact. Both derived GLA controllers are validated by standardized gust simulations, where the blending-based pole placement approach yields slightly better results compared to the \mathcal{H}_2 -optimal blending approach. However, the blending-based pole placement directly yields a static gain feedback controller with limited possibilities for controller tuning, e.g., to satisfy robustness requirements or actuator limitations. In comparison, the \mathcal{H}_2 -optimal blending approach generally allows choosing an arbitrary SISO controller, where herein, a fixed proportional-derivative structure is proposed with only a single tuning parameter. However, it is assumed that selecting a higher order SISO controller allows for an improved GLA performance by specifically taking into account the residual modes which are not yet considered during blending vector design. All in all, straight forward controller design procedures are derived for both blending-based control approaches proving their applicability and effectiveness on high order aeroelastic systems.

5.2 Active Flutter Suppression for an Unmanned Aerial Vehicle

Flutter describes an unstable coupling of aerodynamics and structural mechanics which typically occurs at higher airspeeds. Especially in highly fuel-efficient aircraft designs, this adverse aeroelastic effect often limits the operational velocity range of the aircraft. A promising technology to counteract this adverse effect is active flutter suppression, where feedback control is used to stabilize the aircraft beyond the critical flutter speed, see [94, 155, 156] for examples.

In this section, such an active flutter suppression system is designed and validated for the UAV depicted in Figure 5.10. The considered UAV is specially developed for testing new flutter suppression technologies as a part of the Horizon 2020 project *Flutter Free FLight Envelope eXpansion for ecOnomic Performance improvement* (FLEXOP) [39]. The highly flexible, high aspect ratio wings of the UAV feature a span of 7 m and tend to flutter above a certain airspeed. To actively suppress this flutter and thereby expand the aircraft's operational velocity range, the wings are equipped with numerous control surfaces and sensors. Furthermore, a 300 N jet engine is mounted on the dorsal surface of the fuselage ensuring that the critical flutter speed can be reached for research purposes.



Figure 5.10: The FLEXOP flutter demonstrator.

In Section 5.2.1, a nonlinear aeroelastic model of the demonstrator aircraft is derived, which serves as a basis for flutter suppression controller design and validation. For controller design, the \mathcal{H}_2 -optimal blending approach from Section 3.2 is applied, which allows isolating the critical flutter modes even if they are within the same frequency range. As a result, each isolated flutter mode can be stabilized by a separate SISO controller which is scheduled with airspeed. A detailed description of the design and tuning of the overall flutter suppression controller is given in Section 5.2.2. The promising results of the achieved flight envelope expansion, validated by nonlinear simulations, are discussed in Section 5.2.3.

5.2.1 Aircraft Modeling and Analysis

For flutter suppression controller design and validation, the highly flexible UAV with a maximum takeoff weight of 65 kg is modeled as described in [167]. To that end, the UAV is discretized by 3300 aerodynamic panels and 111 structural nodes, which are both depicted in Figure 5.11. Based on that, the unsteady aero-

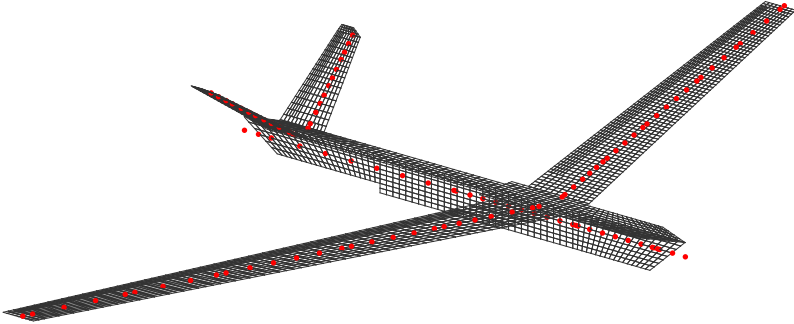


Figure 5.11: Discretized aircraft model with aerodynamic boxes (black) and structural nodes (red).

dynamics model and the structural dynamics model are generated according to Chapter 4. In the structural dynamics model, the first 50 flexible modes and the nonlinear equations of motions from flight mechanics are considered. The unsteady aerodynamics model is realized in state space using rational function approximation according to Roger [135] and includes a gust input which acts at all aerodynamic panels simultaneously. As control inputs, the UAV features four ruddervators on the aircraft's V-tail and four pairs of ailerons on the wing as illustrated in Figure 5.12. For flutter control, only the outermost ailerons are used while the remaining control surfaces are dedicated to primary flight control and high lift generation. The actuators to steer the control surfaces are modeled as second-order systems obtained from frequency-based system identification and include position and rate limits. Furthermore, the thrust generated by the jet engine and the aerodynamic drag are added as additional forces acting on the aircraft structure at predefined locations. To compute the respective forces, a polar-based drag model [138] and a nonlinear second-order model of the jet engine [146] are included. The response of the highly flexible UAV is captured by 13 IMUs located in the wings and near the center of gravity as illustrated in Figure 5.12. Each of the IMUs measures rotational rates and translational accelerations in different spatial directions, where only vertical acceleration and pitch rate measurements are used for flutter control. The individual sensors are

modeled as first-order linear systems including a sensor delay of 15 ms. Eventually, an integrated nonlinear aeroelastic model is obtained by combining the individual models as described in Section 4.4. For more details on modeling of the FLEXOP flutter demonstrator see also [167] and [100].

In order to perform a stability analysis on the FLEXOP flutter demonstrator, the nonlinear model is linearized around steady horizontal flight at different airspeeds. Subsequently, a modal decomposition is carried out on each of the resulting LTI systems allowing for an individual analysis of the obtained aeroelastic modes. The operational velocity range of the UAV is greatly limited by two aeroelastic modes which turn unstable at higher airspeeds. Both unstable modes describe flutter mechanisms based on a coupling of wing bending and torsion, where the mode shape is of symmetric and asymmetric nature, respectively. This is illustrated in Figure 5.13, which is obtained from high-fidelity computational fluid dynamics simulations [139]. While the symmetric flutter mode becomes unstable at around 52 m/s with 8.0 Hz (50.3 rad/s), the asymmetric flutter mode follows at 54.5 m/s with 7.3 Hz (45.9 rad/s). This can also be seen in Figure 5.14 which compares natural frequency and relative damping of both flutter modes, where instability is indicated by a negative relative damping. To increase the aircraft's operational velocity range, it is hence required to stabilize the flutter modes, which is also denoted as flutter suppression as described in the following subsection.

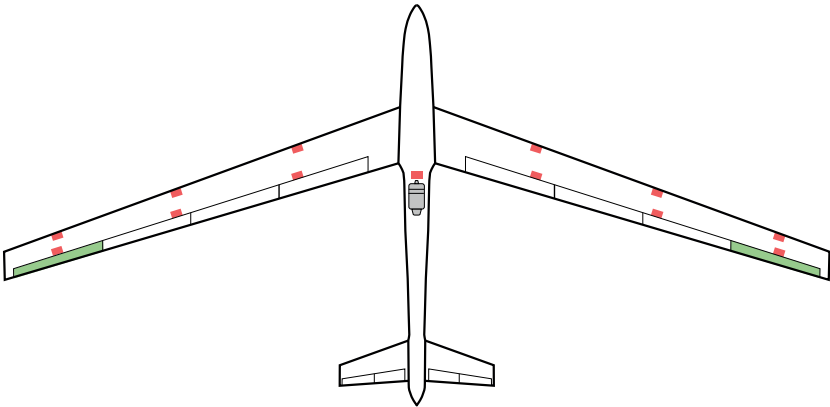


Figure 5.12: Locations of the inertial measurement units (■) and outermost pair of ailerons (■) used for active flutter suppression. The jet engine mounted on the fuselage dorsal surface is depicted in gray (■).

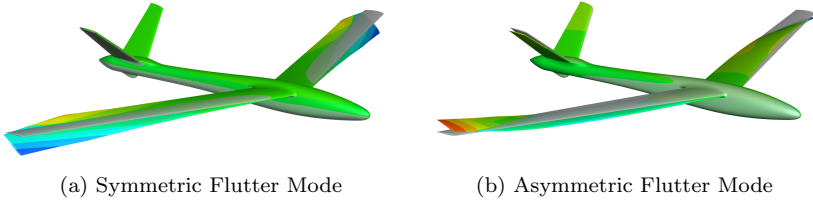


Figure 5.13: Modeshapes of the dominating flutter modes [139].

5.2.2 Flutter Suppression Controller Design

For flutter suppression controller design, the \mathcal{H}_2 -optimal blending approach from Section 3.2 is applied. Thereby, the two flutter modes, which are close in frequency but well distinguishable by their mode shapes, are decoupled and an individual mode stabilization by dedicated SISO controllers is enabled. The corresponding blending vectors and SISO controllers are designed as follows.

Blending of Inputs and Outputs

The control inputs considered for active flutter suppression are the deflections commanded to the outermost aileron on each wing. As measurement signals, the pitch rate and vertical acceleration captured by the 13 different IMUs are considered. Thereby, it is noted that the rate and acceleration measurements are normalized as proposed in Section 3.2.4 since they are of different units. Subsequently, the \mathcal{H}_2 -optimal blending vectors associated to the first (symmetric) and second (asymmetric) flutter mode are computed according to Section 3.2.3. The obtained input and output blending vectors mirror the shape of the underlying modes and thus are also symmetric and asymmetric with respect to the corresponding aileron and sensor positions. Furthermore, sensors at the outer part of the wing are better suited to measure the corresponding flutter modes and hence are higher weighted in the output blending vector. Since the mode shapes change only slightly within the critical airspeed range, it is sufficient to compute the blending vectors at a single airspeed of 60 m/s and hold them constant within the whole flight envelope. Applying the computed blending vectors, the virtual inputs $v_{u,j}$ and virtual outputs $v_{y,j}$ are generated, which are dedicated to the symmetric ($j = 1$) and asymmetric ($j = 2$) flutter mode. The overall achieved decoupling of the two flutter modes can be reviewed in the frequency response depicted in Figure 5.15. It can be seen that the virtual input dedicated to one mode is hardly measurable by the virtual output of the other mode, which is required for an independent SISO controller design. The peaks at the natural frequencies of the symmetric and asymmetric flutter mode further indi-

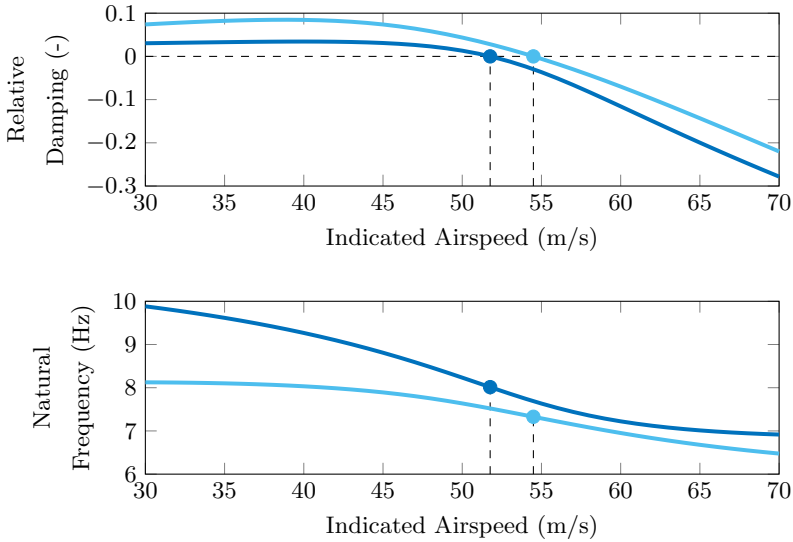


Figure 5.14: Relative damping and natural frequency of the symmetric (—) and asymmetric (—) flutter mode, which turn unstable at around 52 m/s (●) and 54.5 m/s (●), respectively.

cate a good controllability and observability of the respective modes while the contribution of other nearby modes is minor. Taking a look at the higher frequency range, however, it has to be noticed that the flutter modes are not fully decoupled from the rest of the system. Since the frequency separation is large, however, this can be efficiently counteracted by dynamic filtering as described in Section 3.4.1, which is considered in SISO controller design as follows.

SISO Controller Design

With the derived blending vectors, it is possible to design dedicated SISO controllers for the symmetric ($j = 1$) and asymmetric ($j = 2$) flutter mode. The structure of the SISO controllers is predefined as

$$\lambda_j(v_{ias}) = W_{bp} W_j(v_{ias}), \quad (5.4)$$

where W_{bp} denotes a band-pass filter to ensure that no interference occurs with the flight control system operating at lower frequencies and that higher frequency modes are not excited. For both flutter modes, a Butterworth band-pass

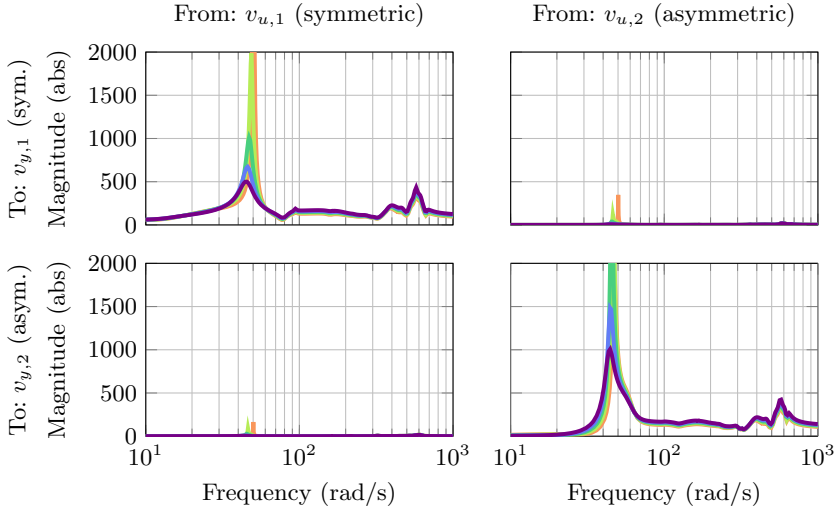


Figure 5.15: Bode-magnitude plots from virtual inputs $v_{u,j}$ to virtual outputs $v_{y,j}$ dedicated to the symmetric ($j = 1$) and asymmetric ($j = 2$) flutter modes. The plots are shown for 52 m/s (—), 54 m/s (—), 56 m/s (—), 58 m/s (—), and 60 m/s (—) indicated airspeed.

filter of fourth order is chosen with a fixed passband from 40 rad/s to 400 rad/s. The corresponding corner frequencies are selected such that both flutter modes are well inside the passband and controller performance is affected as little as possible. Since a large velocity range needs to be considered, the core of the flutter suppression controller $W_j(v_{\text{ias}})$ is gain-scheduled with indicated airspeed $v_{\text{ias}} = v_{\text{ias}}(t)$. For better tuning capabilities, it is desired to keep the order of $W_j(v_{\text{ias}})$ as small as possible, whereas a larger order may allow for a better controller performance or robustness. Hence, a careful balancing between controller order and performance is required. Herein, a satisfactory performance is achieved when choosing a minimum order of two and one for the first (symmetric) and second (asymmetric) flutter mode, respectively. The corresponding state space matrices $Z_j = \{A_j, B_j, C_j, D_j\}$ of $W_j(v_{\text{ias}})$ depend linearly on the indicated airspeed, i.e. $Z_j = Z_j(v_{\text{ias}}) = Z_{j,0} + Z_{j,1}v_{\text{ias}}$, where the matrices $Z_{j,0}$ and $Z_{j,1}$ are subject to be optimized. To that end, two separate robust control design problems are formulated according to [5] considering the predefined parametric SISO controller structure. As explicit optimization constraints, a gain margin of 6 dB and a phase margin of 45° are demanded on the blended

input channel at an indicated airspeed of 30, 40, 50 and 60 m/s. The resulting constrained multi-model optimization problems are non-convex and solved using Matlab's `syntune` routine based on non-smooth optimization techniques [7]. In Figure 5.16, the obtained SISO controllers without the band-pass filter are depicted. Note that with increasing airspeed, the controller gain increases in the symmetric case and decreases in the asymmetric case in the frequency range of the corresponding flutter mode.

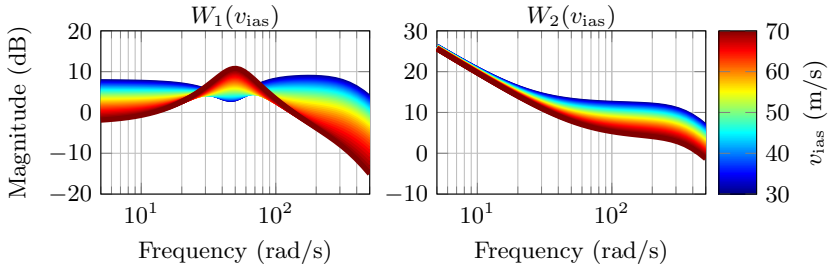


Figure 5.16: Gain-scheduled SISO controllers $W_1(v_{ias})$ for the symmetric flutter mode and $W_2(v_{ias})$ for the asymmetric flutter mode, with indicated airspeed v_{ias} ranging from 30 to 70 m/s.

Linear Closed-Loop Analysis

Closing the two SISO loops stabilizes both flutter modes as it is illustrated in the pole migration plot in Figure 5.17. The plot compares the open-loop poles in gray to the closed-loop poles depicted in color dependent on the airspeed. Clearly visible is the unstable behavior, i.e., the crossing to the right half plane of the first (symmetric) and second (asymmetric) flutter mode in the open-loop. With the flutter suppression controller, the symmetric flutter mode can be stabilized up to airspeeds of 65.5 m/s. The asymmetric mode is stabilized even beyond 70 m/s. Demanding additional single-loop robustness margins of 6 dB in gain and 45° in phase to the critical flight point leads to a maximum operational speed of about 60 m/s. This still results in an increase in allowable aircraft velocity of more than 15% compared to the case without active flutter suppression. Also noticeable is that the other poles of the system(s) are not largely affected by the flutter suppression controller. This is acceptable anyways since damping is rather increased than decreased. The linear analysis results discussed in this section provide an initial validation of the controller. The next mandatory step on the way to the implementation of the control algorithms on the aircraft is to test them in a nonlinear simulation environment of the highly flexible UAV.

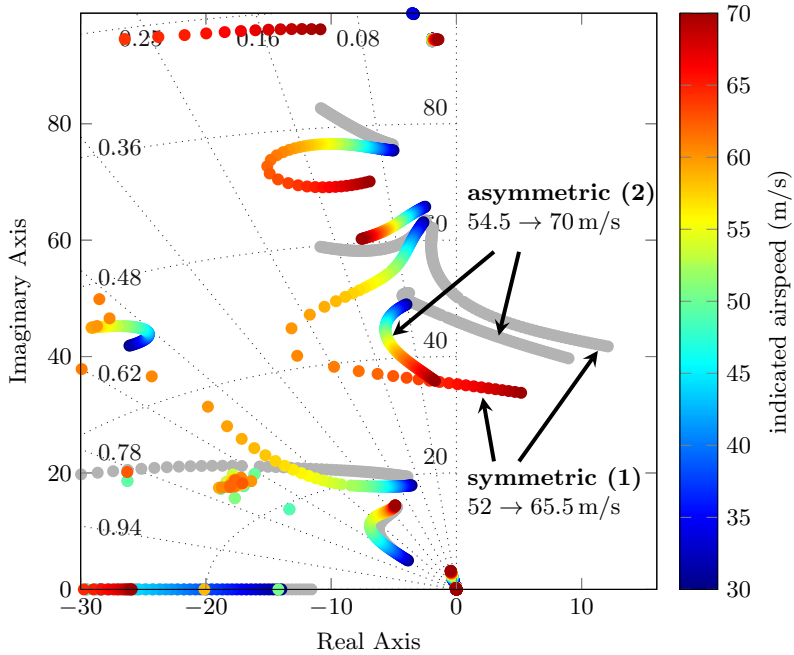


Figure 5.17: Comparison of the open-loop poles (gray) and closed-loop poles (colored) dependent on indicated airspeed.

5.2.3 Controller Validation

To validate the derived flutter suppression controller, two different flight scenarios are simulated using the nonlinear aircraft model from Section 5.2.1. The first scenario is a stepwise acceleration in straight and level flight and the second one is based on a predefined flight test pattern. For this purpose, the aircraft model is augmented by the baseline flight controller derived in [114], which allows for tracking parameters like flight direction, velocity, or altitude. By means of the nonlinear simulations, the results from the linear closed-loop analysis in Section 5.2.2 are validated, confirming the increase of the speed where the aircraft becomes unstable.

Stepwise Acceleration in Straight and Level Flight

In the first flight test scenario, the velocity of the aircraft is stepwise increased until flutter occurs, with and without the flutter suppression controller. To that end, the aircraft is first accelerated from its trim condition at 38 m/s to 50 m/s. Then, its velocity is increased by 4 m/s steps until 62 m/s. In the case where the flutter controller is inactive, the aircraft becomes unstable before reaching 54 m/s, which coincides well with the predicted behavior from linear analysis. Turning on the flutter suppression controller, the aircraft is successfully stabilized and velocity can be further increased using a smaller step size of 2 m/s. At around 66 m/s, the aircraft with active flutter suppression becomes unstable, which confirms the predicted increase in allowable aircraft velocity of around 15%.

In Figure 5.18, the corresponding simulation results are depicted, where flutter suppression is inactive in the two plots on the left (a,b) and active in the two plots on the right (c,d). The unstable regime can be clearly recognized by the drastic drop of the indicated airspeed depicted in (b,d) and the exponential increase of the vertical wing tip acceleration depicted in (b,d). This is also highlighted by coloring the corresponding signals as (—) and (—) in the stable and unstable regime, respectively. Note that in reality, the aircraft would have been lost as soon as it enters the unstable region, but the encountered highly nonlinear behavior is not captured by the given model.

Predefined Flight Test Pattern

Next, the aircraft is simulated on the predefined flight test pattern depicted in Figure 5.19a. For the description of the pattern it is assumed, without loss of generality, that the north direction is equal to the y-axis of the defined coordinate system. The flight simulation starts at (➤) towards the main reference point (●), after which a 180° turn is performed and the actual flutter test is started. The segment between the start and reference point is denoted as the inbound leg, which is dedicated for tracking the reference point in order to ensure a uniform start of the outbound turn. After the outbound turn the aircraft reaches the outbound leg, on which aircraft velocity is increased to test the flutter suppression controller. On the last part of the outbound leg the aircraft is decelerated to avoid flying turns above open-loop flutter speed. Overall, this results in four main segments, for which the reference signals need to be provided. To generate the reference signals, a state-machine with sub-tasks, which are selected based on switching criteria, is implemented [96, 114]. This state-machine together with the baseline and flutter controller allow navigating the aircraft around the test pattern fully autonomously.

In Figure 5.19, the relevant flight parameters of the 200 s long test flight

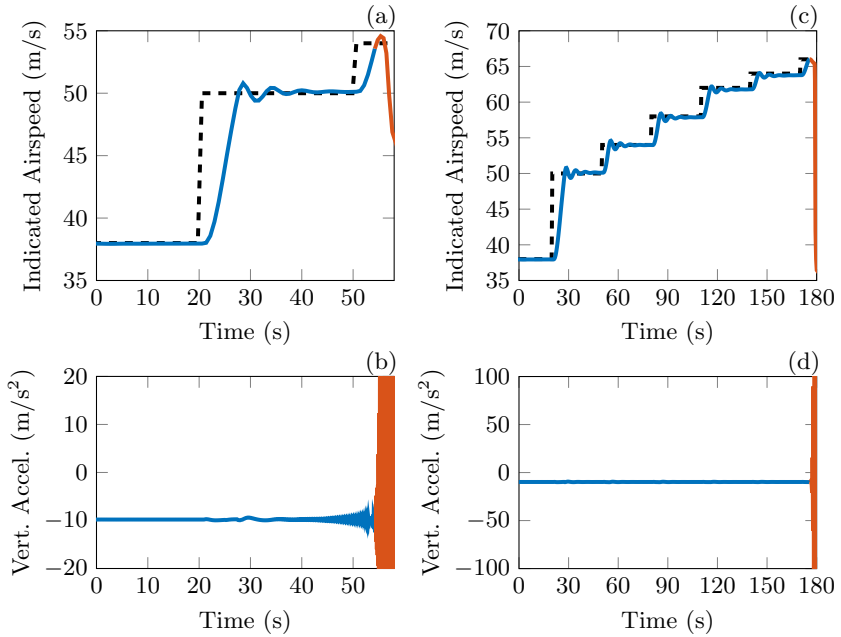


Figure 5.18: Nonlinear simulation results for acceleration test scenario with flutter suppression inactive in (a,b) and active in (c,d). Indicated airspeed is depicted in (a,c) and vertical acceleration at the left wing tip is depicted in (b,d). The reference values are shown as dashed lines (---) and the actual values in stable and unstable regime are represented as (—) and (—), respectively.

along the described pattern are depicted. The chosen flight time corresponds to approximately two laps on the test pattern shown in Figure 5.19a. On the outbound leg of each lap, the aircraft is brought into the open-loop flutter regime. The indicated airspeed (—) is depicted in Figure 5.19c together with its reference command (- - -). The pattern is flown with a nominal speed of 38 m/s. On the outbound leg the speed is increased to 54 m/s in the first lap and 58 m/s in the second lap. The altitude is maintained by the baseline flight controller at 348 m as shown in Figure 5.19b. The visible spikes at about 65 s and 160 s in altitude and airspeed are due to vertical wind gusts simulated on the outbound leg to validate the robustness of the overall control system against disturbances. The impact of the applied gust, generated by a Dryden filter [61], is further visible in Figure 5.19d, where the vertical acceleration at the left wing tip is depicted. While the aircraft is successfully stabilized by the flutter suppression controller, the baseline controller adequately tracks the demanded values in the relevant flight parameters. The control surface deflections commanded by the individual controllers are well within limits, where it is noted that each controller uses separate control surfaces to avoid actuator saturation. Additionally, it is confirmed that the flight control system and the flutter suppression controller

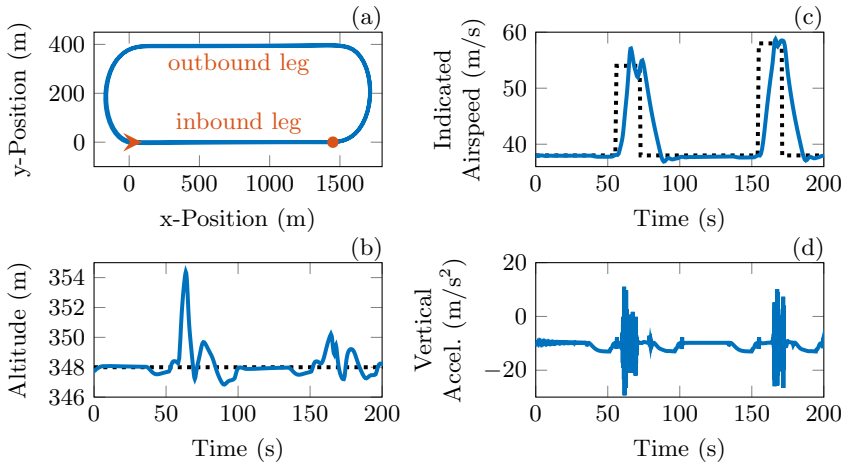


Figure 5.19: Simulated aircraft position during two laps on the test track in (a), where the start (➤) and reference (●) point are marked. The reference (.....) and actual (—) values of the altitude and indicated airspeed are depicted in (b) and (c), respectively. In (d), the vertical accelerations at the left wing tip are depicted.

do not interfere with each other since they are operating in clearly separated frequency ranges. For active flutter suppression, the outermost ailerons are used, where the corresponding deflections are shown in Figure 5.20a and 5.20b for the two flutter test phases. In the first flutter test phase between 62 s and 71 s, the aircraft is accelerated up to 54 m/s and in the second phase between 164 s and 173 s, the aircraft reaches a velocity of around 58 m/s. It can be seen that the left and right ailerons are deflected equally in both phases, which indicates that the symmetric flutter mode is the predominant unstable mode in the considered velocity range.

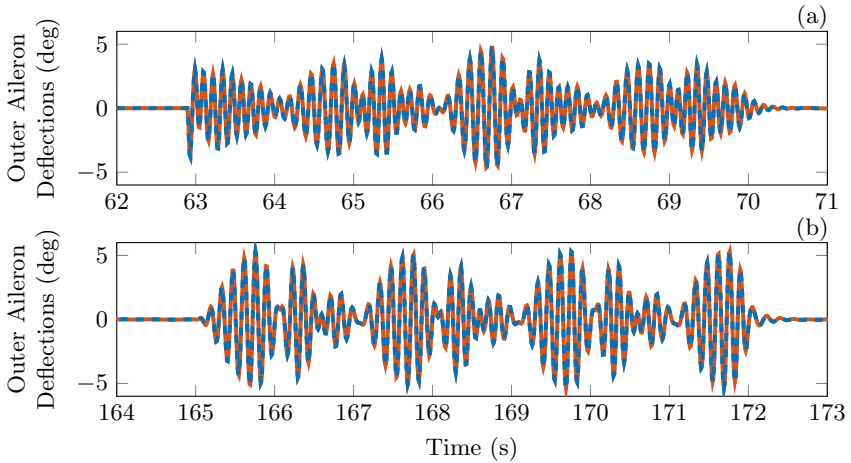


Figure 5.20: Deflections of the left (—) and right (- - -) outermost aileron, which are commanded by the flutter suppression controller on the outbound test lag in the first (a) and second (b) lap.

5.2.4 Conclusions

The presented flutter suppression system aims at increasing the operational velocity range of the FLEXOP demonstrator aircraft by stabilizing the critical flutter modes. To that end, the critical flutter modes are isolated using the proposed \mathcal{H}_2 -optimal blending approach and individually stabilized by separate SISO controllers. The gains of the dedicated SISO controllers are scheduled with airspeed and systematically tuned in a model-based optimization setup using robust control techniques. To validate the derived flutter suppression controller, high-fidelity nonlinear simulations are carried out for different test sce-

narios. The promising results show that it is possible to extend the aircraft's operational speed range by around 15% using the developed control system. Thereby, the applicability of the proposed \mathcal{H}_2 -optimal blending approach to parameter-varying unstable systems is successfully demonstrated. Furthermore, a high degree of confidence is gained that the developed system will also work satisfactorily during the real flight tests.

5.3 Control of a Highly Flexible Wing in a Wind Tunnel

This section focuses on the design and experimental validation of a GLA system for the highly flexible wing depicted in Figure 5.21. The experimental wing is designed within the DLR project KonTeKst (Configurations and Technologies for Short Range Aircraft) [86] and serves as a technology demonstrator for active GLA. To that end, the wing is equipped with, among others, three trailing edge flaps, eight vertical acceleration sensors and a piezo balance measuring the structural loads in the wing root. For controller validation, the wing is mounted in a closed circuit wind tunnel with a maximum flow velocity of 65 m/s and excited with gusts simulated by a pitching motion of the wing. The overall experimental setup including the positions of the flaps and sensors is depicted in Figure 5.22.

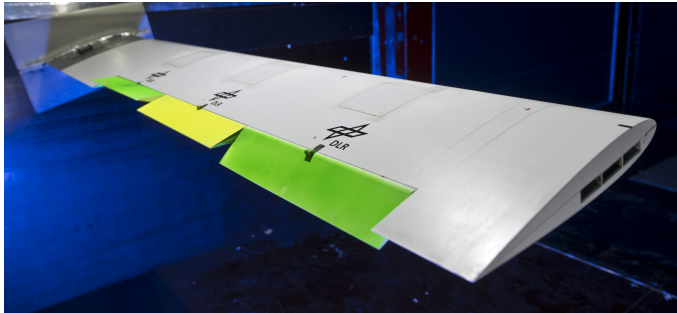


Figure 5.21: Flexible wing mounted in the wind tunnel.

The GLA controller is designed using the \mathcal{H}_2 -optimal blending approach from Section 3.2. For this purpose, an aeroelastic model of the experimental wing, which features a span of 1.6 m and a chord length of 0.25 m, is derived as described in Section 5.3.1. To also consider actuator faults and flap deflection constraints, the GLA controller further includes the control allocation proposed in Section 3.5. The developed GLA system is extensively tested in wind tunnel experiments considering different excitations, airspeeds and fault scenarios. The promising results are discussed in Section 5.3.3 and pave the way to proceed with research activities on real aircraft.

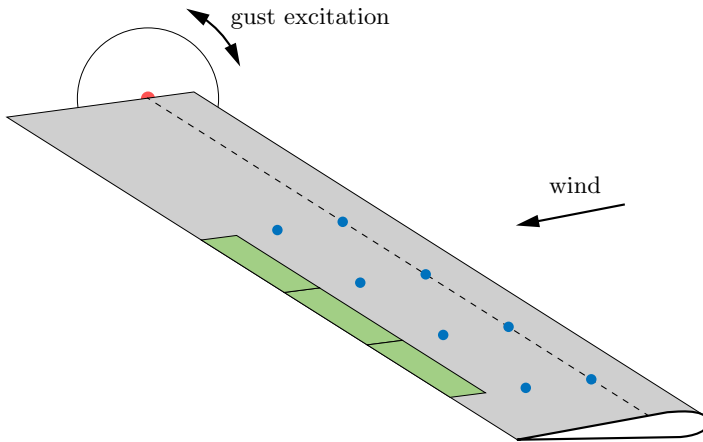


Figure 5.22: Experimental setup of the flexible wing mounted in the wind tunnel. The locations of the quarter chord line (---), the three trailing edge flaps (■), the vertical acceleration sensors (●) and the piezo balance measuring the structural loads (●) are marked.

5.3.1 Wing Modeling

Structural Dynamics Model

The wing structure consists of highly flexible glass fiber skins and a foam core. To model the corresponding structural dynamics, an FE model with 35 structural nodes is generated. See [30, 31] for more details. As depicted in Figure 5.23, the nodes are placed along the quarter-chord line of the wing and the hinge lines of the flaps. In order to obtain a model of high accuracy, the masses of the individual components like actuators or sensors are separately determined and added as point masses to the FE model. See Table 5.6 for a summary of the individual component masses. Furthermore, a modal test is carried out on the

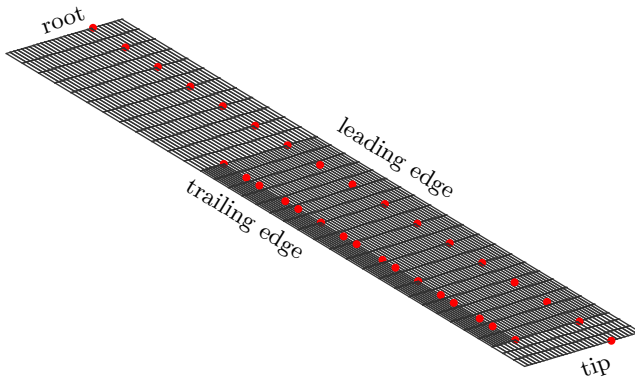


Figure 5.23: Discretized wing model with aerodynamic boxes (black) and structural nodes (red).

Table 5.6: Masses of individual components.

component	mass (g)
sensors (incl. cables)	167
actuators (incl. cables)	260
flaps (incl. mounting)	300
wing (incl. mounting)	2840
total wing mass	3567

fully assembled wing to determine the natural frequency, the relative damping and the shape of the wing's flexible modes. To that end, the wing is excited at different locations with a modal hammer. On the resulting response, captured by specifically mounted acceleration sensors, a modal analysis is carried out according to [50]. The first four identified flexible modes are listed in Table 5.7, where it is noted that these modes are considered as *structural* modes and not *aeroelastic* modes since the speed of the surrounding airflow is zero. Based on

Table 5.7: Identified flexible modes.

mode name	frequency (Hz)	damping (%)
1 st bending	7.96	0.4
1 st in-plane	29.10	0.5
2 nd bending	42.20	0.7
1 st torsion	82.70	1.9

that, theoretical and experimental modal results are matched by optimizing uncertain parameters like the fiber angles of the skin or the density of the foam core in the FE model. See [30, 31] for more details. Eventually, a modal analysis is carried out on the optimized FE model and the eight flexible modes with the lowest natural frequency are selected for aeroelastic modeling. Considering the rigid-body motion, only the pitching DOF around the quarter-chord line is modeled since the wing is rigidly mounted on the pitch excitation system described in Section 5.3.1. Eventually, an updated structural dynamics model is obtained which includes the first eight flexible modes and a single rigid-body mode.

Aerodynamics Model

The highly flexible wing is 1.6 m long and features a symmetric NACA 0015 profile with a chord length of 0.25 m. The corresponding aerodynamics model is derived according to Section 4.2 and consists of 1250 aerodynamic panels, which are depicted in Figure 5.23. For a better modeling accuracy, the panel size is reduced for the trailing edge flaps, where each flap has a size of 30 cm (span-wise) by 5 cm (chord-wise). The unsteady aerodynamics model is realized in state space using Roger's approximation, where the resulting model is reduced to an order of 20 applying balanced truncation [161].

Sensors and Actuators

For active control, eight vertical acceleration sensors are installed inside the flexible wing. The sensor positions are close to the flap positions as depicted in Figure 5.22. Additionally, the performance of the GLA control system is validated by measuring the open- and closed-loop structural loads in the wing root using a piezo balance. The sensor equations for both the acceleration and loads measurements are derived in Section 4.3 and included in the aeroelastic model.

The unfiltered acceleration signals are processed by the feedback control system running at a sampling time of 1 kHz yielding control commands which are sent to the flap servos by means of pulse width modulation (PWM). The transfer function from the commanded to the actual flap deflection angle is experimentally identified and approximated as $G_{\text{flap}}(s) = 90/(s+90) G_{\text{padé}}(s)$ for all three flaps. The time delay of the actuators is 8 ms and approximated according to Padé as $G_{\text{padé}}(s) = (250 - s)/(250 + s)$. Note that the 8 ms time delay also includes a 1 ms process time of the controller. Furthermore, the backlash of the inner, mid and outer flap is identified as 1.5° , 0.4° and 1.2° , respectively. Note that backlash is not considered in the linear model used for controller design, however, it has a great impact on controller performance as discussed in Sections 5.3.2 and 5.3.3. For a more detailed description of the actuation system and also its nonlinear characteristics, see [151].

Gust Excitation

In order to excite the experimental flexible wing, vertical gusts are simulated by a forced pitching motion around the wing's quarter-chord line. In the frequency range of interest, this kind of excitation is comparable to an external gust generator due to the high torsional stiffness of the wing. Pitching the wing adds an additional angle of attack, similar to vertical gusts during flight. To induce the desired pitching motion, the wing is mounted on a pitch excitation system at its root. The pitch excitation system includes a separate control unit which allows tracking a desired pitch angle θ_{cmd} by generating the required pitching moment. In the integrated aeroelastic model derived in Section 4.4, this pitching moment is described by the external forces $p_{\text{other}} = G_{\text{pitch}}(s)\theta_{\text{cmd}}$ acting on the wing. Therein, the pitch excitation system $G_{\text{pitch}}(s)$ is modeled as a second-order Butterworth low-pass filter with a roll-off frequency of 200 rad/s.

Model Integration

Eventually, the models of the structural dynamics, aerodynamics, actuators, sensors and gust excitation system are combined as depicted in Figure 4.2 in

Section 4.4. The resulting integrated aeroelastic model has 46 states and depends on the surrounding airspeed. For more details on the modeling of the experimental wing see [30, 31, 127].

5.3.2 Gust Load Alleviation Controller Design

To reduce the structural loads of the flexible wing during gust encounters, a GLA controller is designed consisting of two modules: a linear baseline control law and a control allocation module. The baseline control law aims at reducing the WRBM by damping the wing using the \mathcal{H}_2 -optimal blending approach described in Section 3.2. For control allocation, the approach described in Section 3.5 is used which allows handling actuator constraints like saturation and faults. The design of both the baseline controller and the control allocation is discussed as follows.

Baseline Controller Design

In order to apply the \mathcal{H}_2 -optimal blending approach from Section 3.2 for GLA controller design, the loads dominating aeroelastic modes need to be identified first. To that end, the airspeed of the aeroelastic model derived in Section 5.3.1 is fixed at different values and a modal decomposition is carried out on the resulting LTI systems. Thereby, it becomes clear that the lightly damped first and second wing bending modes dominate the WRBM. This can also be seen in Figure 5.24a, where the two peaks around 8 and 46 Hz are associated to the first and second wing bending mode, respectively. The second wing bending

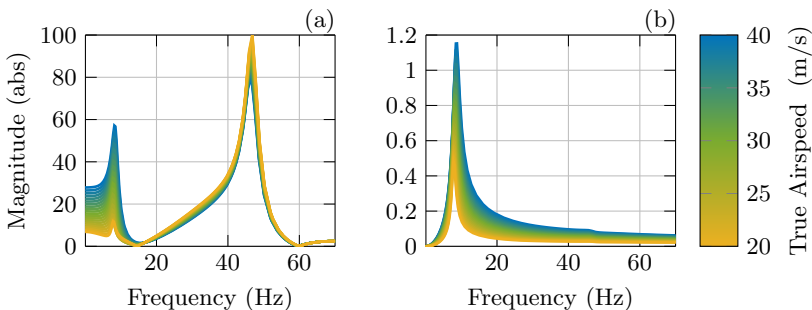


Figure 5.24: Selected frequency responses at different airspeeds:
 (a) from pitch angle (deg) to WRBM (Nm)
 (b) from blended inputs (deg) to blended outputs (m/s^2).

mode, however, is marginally excited during gust encounters due to its high natural frequency and the low-pass characteristic of gusts. Thus, the objective for blending-based GLA controller design is to increase the damping of the first wing bending mode.

For the blending vector design, the three flap deflection commands are considered as control inputs, and all eight vertical acceleration sensor signals are considered as measurement outputs. Since the shape of the first wing bending mode varies only slightly within the considered airspeed range, the corresponding input and output blending vectors $k_u \in \mathbb{R}^3$ and $k_y \in \mathbb{R}^8$ are computed at a single airspeed $v_{\text{tas}} = 40$ m/s and held constant for all airspeeds. Applying the computed blending vectors isolates the first wing bending mode as depicted in Figure 5.24b and enables the design of a SISO controller to increase its damping. As SISO controller, a gain-scheduled proportional-integral (PI) controller is chosen which is augmented with the band-pass filter W_{bp} . The band-pass filter restricts controller activity to the frequency range of the first wing bending mode and suppresses noise at high frequencies. The proportional and integral gains $k_p(v_{\text{tas}}(t))$ and $k_i(v_{\text{tas}}(t))$ are scheduled with true airspeed $v_{\text{tas}}(t)$, where both gains are manually tuned at $v_{\text{tas}} = 20, 30, 40$ m/s and linearly interpolated in between. The controller is tuned in such a way that the damping of the first wing bending mode is maximized considering flap deflection limits and robustness requirements. The maximum flap deflections are given as $\pm 10^\circ$ and are evaluated in terms of closed-loop simulations carried out for the worst-case harmonic pitch excitation causing ± 10 cm wing tip deflection. The robustness of the control loop is evaluated in terms of the symmetric disk margin [18], which is computed at each of the multiple inputs and multiple outputs (loop-at-a-time). As a minimum requirement, a 45° phase margin is demanded, which is equivalent to a 7.7 dB gain margin. Eventually, the baseline GLA controller computes the flap deflection commands as

$$u(t) = k_u W_{\text{bp}} \left(k_p(v_{\text{tas}}(t)) k_y^T y(t) + \int_0^t k_i(v_{\text{tas}}(\tau)) k_y^T y(\tau) d\tau \right), \quad (5.5)$$

where $y(t)$ collects the eight vertical acceleration measurements. Furthermore, it is noted that the true airspeed $v_{\text{tas}}(t)$ is separately measured by a pitot tube mounted in the windtunnel.

The achieved damping of the first wing bending mode for fixed airspeeds is depicted in Figure 5.25. It can be seen that the relative damping is increased by a factor of more than five at higher airspeeds while it is not even tripled at lower airspeeds. This is due to the fact that flap efficiency increases with increasing airspeed. Furthermore, it is noted that the poles of the remaining aeroelastic modes are hardly affected when closing the loop. This is a result of the band-pass behavior of the SISO controller and the isolation of the first wing bending mode via input and output blending.

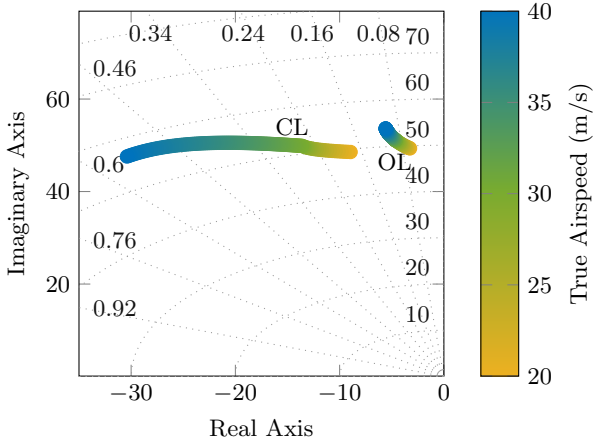


Figure 5.25: Comparison of the open-loop (OL) and closed-loop (CL) poles of the first wing bending mode at different airspeeds.

Control Allocation

In the case of actuator saturation or faults, the performance of the derived baseline controller is generally decreased. Since the considered flexible wing is actually over-actuated, this performance loss can be avoided or at least reduced by means of control allocation [115]. Implementing the control allocation proposed in Section 3.5, the actual control inputs u are computed from the virtual control input v_u such that nominal controller performance is maintained as good as possible in presence of actuator constraints. The corresponding optimization problem is given in Equation (3.112), where $p = 2$ is chosen here. This means that the objective is to minimize the 2-norm of the slack variable τ and redistribution vector Δu , which are weighted by $W_\tau = 2 \times 10^9$ and $W_u = I$, respectively. In doing so, it is enforced that control input redistribution is preferred over controller performance degradation. Furthermore, it is noted that no mode decoupling constraints are considered during baseline controller design and thus also control allocation, i.e., $R_{u,j} = 0$ with $j = 1$. To solve the optimization problem (3.112), which is a convex quadratic program when reformulated according to Equation (3.115), numerous computationally efficient methods are readily available. Herein, a derivative of the KWIK algorithm described in [143] is used, where the lower and upper actuator limits u_{\min} and u_{\max} can be updated in real-time. This allows, e.g., to consider a faulty actuator by setting both of its limits to zero.

5.3.3 Experimental Validation

The aeroelastic model derived in Section 5.3.1 and the GLA control system derived in Section 5.3.2 are validated at the Crosswind Simulation Facility of the German Aerospace Center (DLR) in Göttingen. The maximum flow velocity of the closed-circuit wind tunnel is 65 m/s and the dimension of the test section is 2.4 m (width) by 1.6 m (height). The flexible wing mounted in the wind tunnel is depicted in Figure 5.21. At the wing root, the wing is attached to the pitch excitation system, which is installed outside of the wind tunnel such that only the wing is exposed to the airflow. Just as the control system, which runs on a Jäger ADwin Gold real-time system at a sampling rate of 1 kHz. The validation of the aeroelastic model and the baseline controller without and with control allocation is performed at different airspeeds, where the results are discussed as follows.

Aeroelastic Model Validation

In order to validate the aeroelastic model derived in Section 5.3.1, sweep excitations are performed at 20, 30 and 40 m/s true airspeed. In this way, the transfer functions from the pitch angle and the individual flap deflection angles to the vertical accelerations and loads measurements are identified. The experimental results correspond well to the simulation results as seen in Figure 5.26. As expected, the same excitations yield larger accelerations and loads at higher airspeeds due to the increased dynamic pressure. To ensure that structural load limits are not exceeded, flap and pitch deflections are limited depending on the current airspeed. Furthermore, the aeroelastic modes of interest are directly identified during the experiments by means of the real-time capable output-only modal analysis described in [70] and [71]. For the first wing bending mode, the natural frequency remains almost constant while its damping increases with airspeed. This also corresponds well to the theoretical results as compared in Table 5.8.

Baseline Controller Validation

The performance of the baseline controller, i.e., the GLA system without control allocation, is evaluated by performing open- and closed-loop experiments for different gust excitations. The gust excitations are simulated by pitching the wing and include both discrete and stochastic gusts. Additionally, sweep excitations are carried out. Each pitch excitation is performed with and without the GLA controller at 20, 30 and 40 m/s true airspeed, where the resulting WRBMs are compared for controller performance evaluation.

For discrete gusts, the “1-cos” gust model from [61] is considered, which is also used in Section 5.1.3 where a more detailed description is given. To identify

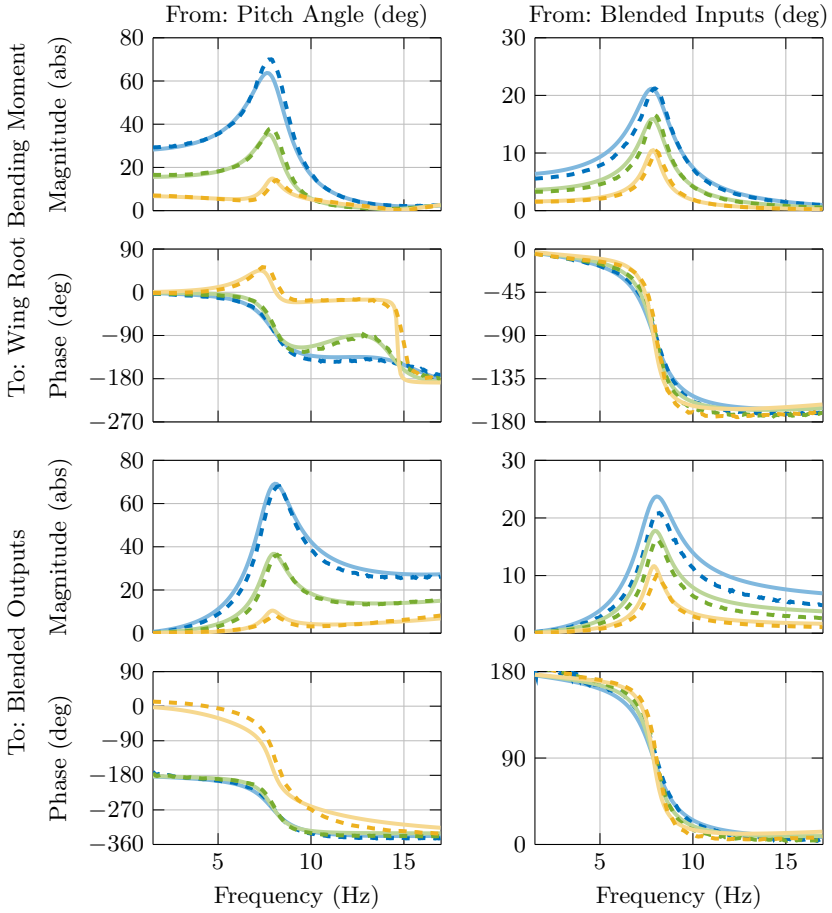


Figure 5.26: Comparison of aeroelastic simulation model (solid) and experimentally identified model (dashed) for 20 m/s (—, - - -), 30 m/s (—, - - -) and 40 m/s (—, - - -) true airspeed.

the critical “1-cos” gust, first the gust length H is determined which causes the largest WRBM for a moderate design speed. As expected, gust lengths yielding gusts in the frequency range of the first wing bending mode cause the largest WRBM. Then, the design speed v_{ds} is adjusted such that the WRBM does not exceed 100 N m. In Figure 5.27, the input and output data for the critical “1-cos” gust excitation at 40 m/s true airspeed is shown. The pitch excitation signal for both experiments open- and closed-loop is depicted in Figure 5.27a together with the closed-loop flap deflection commands. Comparing the inner, mid, and outerflap deflections, it can be seen that the ratio between them remains constant as a result of input blending. Thereby, the outer flap is deflected the most and the inner flap the least, which reflects the shape of the first wing bending mode. The resulting reduction of the WRBM is visible in Figure 5.27b, where the open- and closed-loop measurements are compared. Clearly, both the peak and the settling time of the WRBM are reduced when closing the loop confirming the load reduction capabilities of the baseline controller. Note that the WRBM measurement is only used for controller performance analysis and is not used in the feedback channels of the controller. Thereby it provides an independent variable to validate the performance of the developed algorithms. In Figure 5.27c and 5.27d, the measured data is further analyzed using fast Fourier transformations (FFTs). Figure 5.27c illustrates that the “1-cos” pitch signal excites the system up to a frequency of about 15 Hz, where the main energy is concentrated in the lower frequency range. In Figure 5.27d, the peak in the open-loop response lies at around 8 Hz, which is caused by the lightly damped first wing bending mode. The baseline controller, designed to increase the damping of this mode, flattens the peak and greatly reduces the output energy around its natural frequency, which is marked with a dotted line.

To simulate stochastic gusts and test a broader frequency range, noise is commanded to the pitch motor. The noise is generated with a variance of 0.7 deg within a frequency range of 3 Hz and 20 Hz. A short section of the 300 s long excitation signal in time domain is depicted in Figure 5.28a. In Figure 5.28c, the FFT of the 300 s long input signal is depicted. Note that the signal has been smoothed for better readability. Clearly, the main energy of the input signal is concentrated in the lower frequency range between 3 Hz and 10 Hz. The reduction of the WRBM peaks by the controller are well visible by comparing the open-loop and closed-loop time signals in Figure 5.28b. FFTs of these two signals further reveal that energy around 8 Hz is clearly reduced in the closed-loop compared to the open-loop, see Figure 5.28d. Similarly to the “1-cos” excitation, the main energy in the output signal is concentrated around 8 Hz in the open-loop although this is not the case for the input signal. This is due to the lightly damped first bending mode at 8 Hz. Increasing its damping with the baseline controller leads to the desired reduction of energy in the output signal.

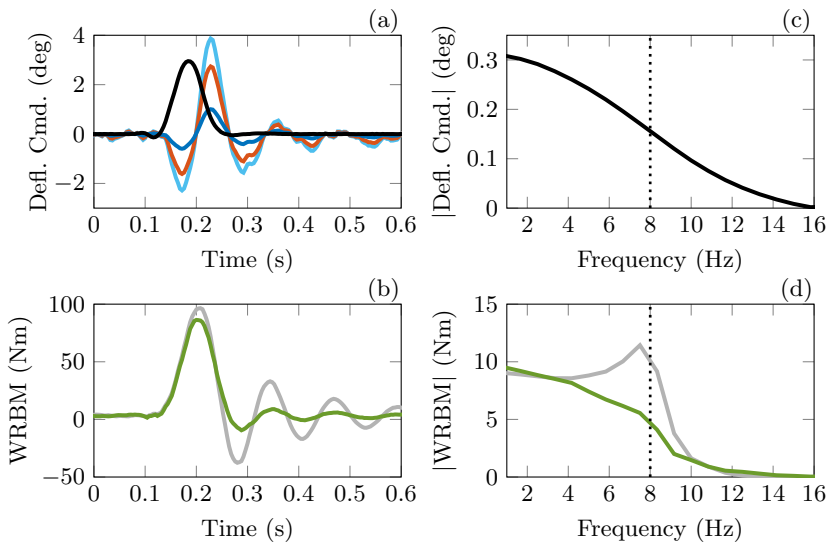


Figure 5.27: Input and output data for the critical “1-cos” pitch excitation at 40 m/s in the time domain in (a,b) and in the frequency domain in (c,d). In (a,c), the pitch excitation signal (—) is depicted. In (b,d), the open-loop (—) and closed-loop (—) wing root bending moment (WRBM) is compared. Additionally, the closed-loop inner (—), mid (—), and outer (—) flap deflection commands are shown in (a).

Finally, closed-loop sweep excitations are performed with the pitch motor at different airspeeds. The identified transfer functions are compared with the open-loop results from model validation in Figure 5.29. The WRBM reduction resulting from actively damping the first wing bending mode is clearly visible at all airspeeds. Furthermore, the actual increase in modal damping is identified online and verified offline, where the corresponding values are given in Table 5.8. Compared to the simulation results, the achieved damping of the first wing bending mode is considerably smaller than expected, independent of the airspeed. The main reason for this lies in the large backlash of the flap actuation system, which is also discussed in the next subsection.

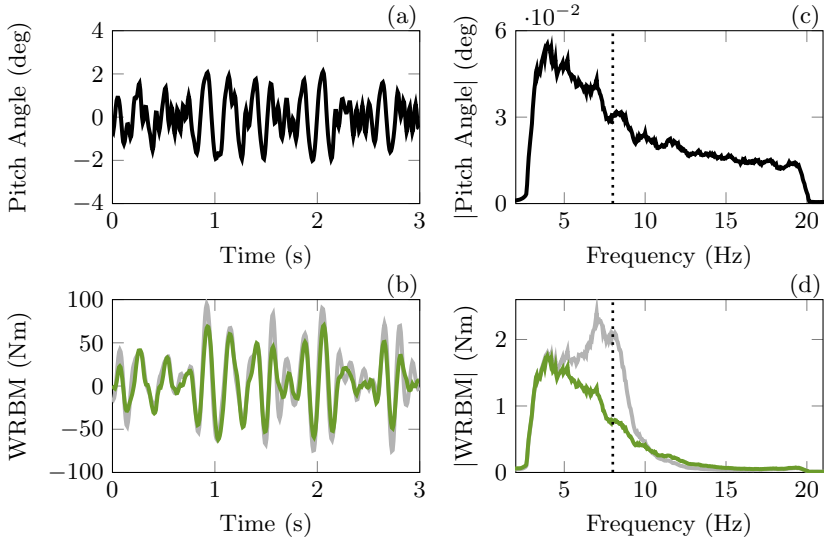


Figure 5.28: Snippet of input and output data for noise excitation at 40 m/s true airspeed in time domain in (a,b) and frequency domain in (c,d). In (a,c) the pitch motor noise excitation (—) is depicted, while in (b,d) the open-loop (—) and closed-loop (—) wing root bending moment (WRBM) is compared.

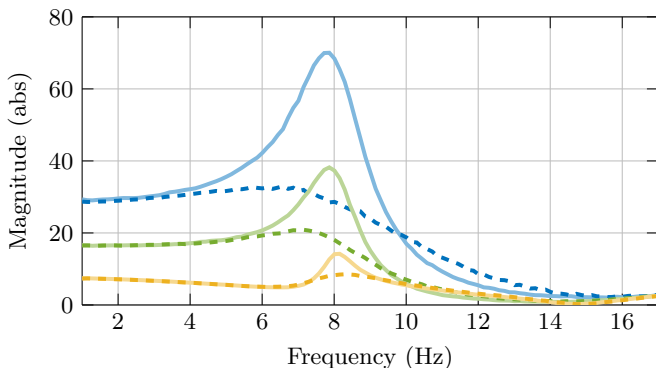


Figure 5.29: Identified open-loop (solid lines) and closed-loop (dashed lines) frequency response from pitch angle (deg) to wing root bending moment (Nm) at 20 m/s (—, - - -), 30 m/s (—, - - -) and 40 m/s (—, - - -) true airspeed .

Table 5.8: Natural frequency and relative damping of the first bending mode in simulation (SIM) and experiment (EXP) for open- and closed-loop.

true airspeed (m/s)	natural frequency (Hz)		relative damping (%)	
	open-loop SIM / EXP	closed-loop SIM / EXP	open-loop SIM / EXP	closed-loop SIM / EXP
20	7.9 / 8.1	7.9 / 8.2	6.6 / 4.9	18.1 / 11.0
30	8.2 / 8.0	8.2 / 7.8	8.9 / 8.4	26.2 / 21.1
40	8.6 / 8.0	9.0 / 8.1	10.4 / 11.0	53.8 / 34.4

Control Allocation Validation

Eventually, the augmented baseline controller with control allocation is validated at 20, 30 and 40 m/s true airspeed. For the different airspeeds, similar results are obtained and hence, only the ones at 40 m/s are discussed herein. In a first step, closed-loop experiments are carried out for an 8 Hz sinusoidal pitch excitation of 1° amplitude where flap deflection commands are artificially restricted to $\pm 1.5^\circ$. To evaluate the effect of the control allocation, the experiments are performed twice, with and without control allocation, where each experiment is carried out for 60 s. Also taking into account the nominal closed-loop without any command limitations and only the baseline controller, three different controller configurations are tested in total, which are summarized in Table 5.9. For each of the three controller configurations, the resulting inner

Table 5.9: Controller configurations for control allocation validation.

Configuration Name	Associated Color	Command Limitation	Control Allocation
nominal		off	off
restricted		on	off
reconfigured		on	on

($\bullet\bullet\bullet\bullet$), mid (---), and outer (---) flap deflection commands are depicted in Figure 5.30a-c, respectively. Considering the nominal closed-loop, the flap deflections are not limited and no saturation occurs as depicted in Figure 5.30a. In comparison to that, control commands are limited to $\pm 1.5^\circ$ in the restricted controller configuration, which drives the outer and mid flap into saturation as depicted in Figure 5.30b. Thereby, the commands are generally increased since wing damping is degraded and higher accelerations are fed back to the flap actuators, as it is especially visible for the inner flap. Activating control allocation in the reconfigured case, the saturation of the mid and outer flap is compensated by a larger deflection of the non-saturated inner flap as shown in Figure 5.30c. In doing so, however, also the inner flap is driven into saturation. As soon as all three flap commands are saturated, nominal controller performance cannot be fully recovered anymore, which is indicated by the slack variable τ depicted in Figure 5.30d. Recall that the slack variable is considered as a direct measure for modal controller performance degradation, where $\tau = 0$ means full controller performance and $\tau = 1$ means that the controller is actually turned off.

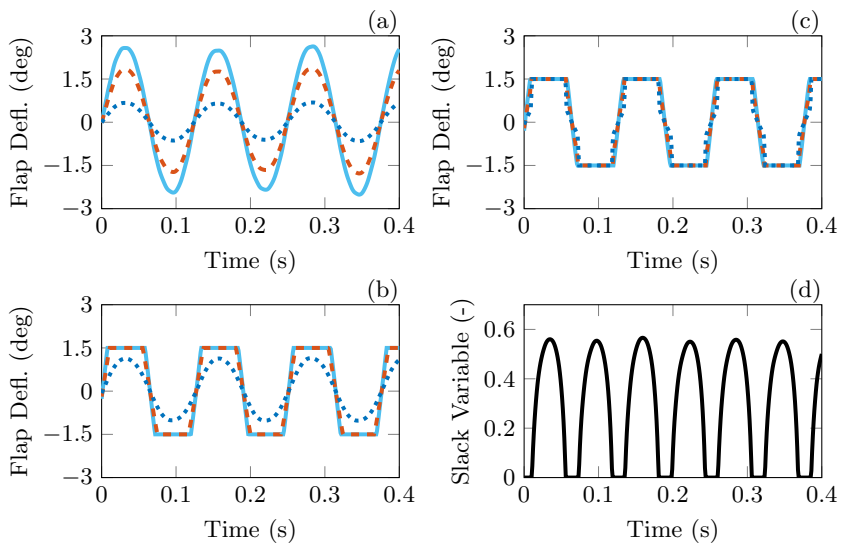


Figure 5.30: Inner (\cdots), mid ($-\cdots-$), and outer ($-$) flap deflection commands for the nominal (a), restricted (b) and reconfigured (c) controller configuration. The slack variable ($-$) of the reconfigured configuration with active control allocation is depicted in (d). The experiments are performed at 40 m/s true airspeed with an 8 Hz sinusoidal pitch excitation of 1° amplitude.

The performance of each controller configuration is validated in terms of the achieved WRBM reduction, which is computed as

$$\eta_f = 1 - \frac{f(|y_{\text{wrbm},\text{cl}}|)}{f(|y_{\text{wrbm},\text{ol}}|)}, \quad (5.6)$$

where $y_{\text{wrbm},\text{ol}}$ and $y_{\text{wrbm},\text{cl}}$ denote the open- and closed-loop WRBM measurements, and the function $f = \{\text{max}, \text{rms}\}$ returns the maximum (max) or root-mean-square (rms) value of the given signal. In Figure 5.31, η_{rms} and η_{max} are depicted for the three different controller configurations given in Table 5.9. As expected, limiting flap deflections degrades nominal controller performance, where both η_{rms} and η_{max} show similar tendencies. Activating control allocation in the reconfigured controller configuration notably increases controller performance. However, nominal controller performance cannot be fully recovered since all flaps are driven into saturation.

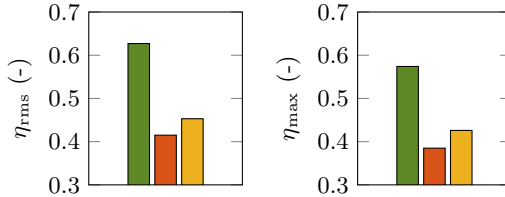


Figure 5.31: Controller performance η_{rms} and η_{max} for the nominal (■), restricted (■), and reconfigured (■) controller configuration considering a $\pm 1.5^\circ$ command limitation for the latter two configurations. The experiments are performed at 40 m/s true airspeed with an 8 Hz sinusoidal pitch excitation of 1° amplitude.

In a second step, the capability of the control allocation to compensate actuator faults is investigated. To that end, a faulty outer flap actuator is simulated by freezing it at 0° . To deal with the faulty actuator, its lower and upper deflection limits are set to zero in the control allocation. As a consequence, it is enforced that the virtual control command is distributed to the non-faulty actuators while zero is commanded to the faulty one. For a comparative performance assessment, closed-loop experiments are carried out for each of the three controller configurations given in Table 5.9. But instead of limiting all flap deflections to $\pm 1.5^\circ$ in the restricted and reconfigured controller configuration, only the outer flap is limited here by freezing it at 0° . As gust excitations, the “1-cos” and noise excitation from baseline controller evaluation are taken into account besides the sinusoidal excitation from the previous experiments. The resulting WRBM reduction is again evaluated in terms of η_{rms} and η_{max} , which

are computed according to Equation (5.6) and compared in Figure 5.32. As expected, controller performance is clearly reduced in the restricted case, where the outer flap is not working, compared to the nominal case, where all three flaps are operating regularly. Activating control allocation, nominal controller performance is recovered in the reconfigured case by compensating the faulty outer flap with larger deflections of the two remaining flaps. Taking a closer look on Figure 5.32, however, it can be recognized that the WRBM reduction in the reconfigured case, with only two flaps in operation, is slightly higher than the one resulting from the nominal case, with all three flaps working. After some closer investigation, this curious result is traced back to the large backlash of the inner flap, which is around 1.5° . Nonlinear simulations reveal that in the nominal case without any actuator fault, the inner flap is actually not, or only marginally deflected since the commanded deflections are mostly within free play. Obviously, this reduces nominal controller performance. In contrast, the reconfigured controller configuration commands larger deflections to the inner flap yielding a smaller performance loss due to the increased operation outside of the backlash area.

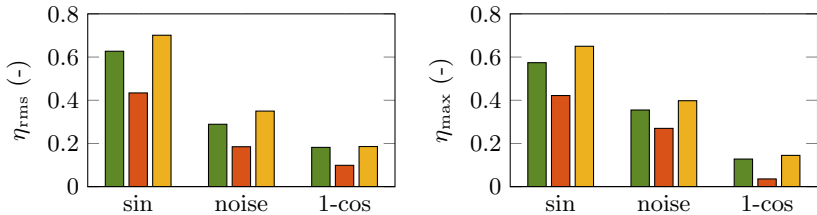


Figure 5.32: Controller performance η_{rms} and η_{max} for the nominal (■), restricted (■), and reconfigured (■) controller configuration considering a faulty outer flap for the latter two configurations. The experiments are performed at 40 m/s true airspeed with sine, noise and “1-cos” pitch excitations.

In a final step, an entire fault scenario is tested where the outermost flap actuator is frozen at 2° not from the beginning on but in the middle of the experiment. As excitation, a sinusoidal pitching motion of 8 Hz frequency and 1° amplitude is chosen. The resulting control and measurement signals are depicted in Figure 5.33 and can be divided into four main segments. The test is started in open-loop, i.e., only the excitation signal at the pitch motor is present and excites the wing while the GLA controller is switched off. After around 2 s the GLA controller is switched on. Figure 5.33a shows the deflections commanded to the inner (—), mid (—), and outer (—) flap counteracting the wing

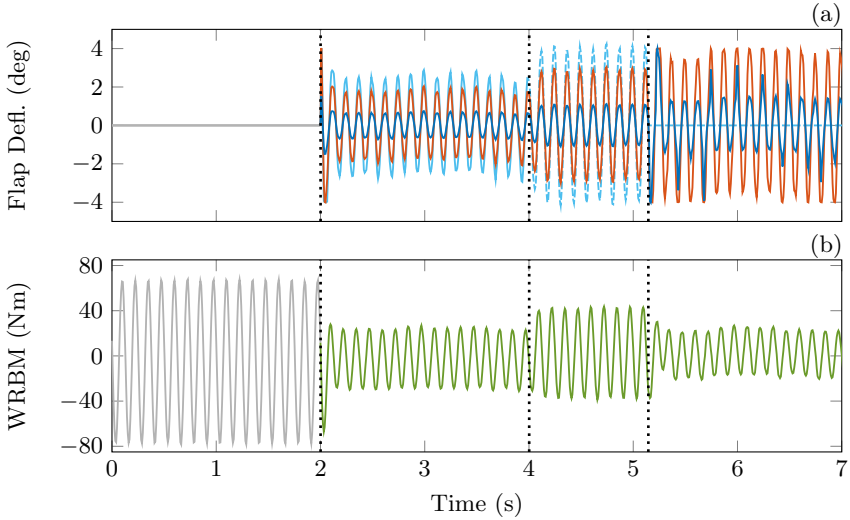


Figure 5.33: Input and output data of the fault-tolerant control experiment with an outer flap actuator fault during sinusoidal pitch excitation. The commands for the inner (—), mid (—), and outer (---) flap are depicted in (a), where (---) denotes that the outer flap command is not realized due to the simulated actuator fault. In (b), the measured wing root bending moment is depicted with open- and closed-loop operation indicated by (—) and (—), respectively.

oscillations. In Figure 5.33b, the measured WRBM is depicted. As soon as the baseline controller is activated, the WRBM is reduced by almost 60%. At around 4 s the outer flap actuator is frozen at 2° . As the fault is present but the controller has not been reconfigured, commands to the outer flap are still present but not realized in the third part of the experiment, which is indicated by the dashed line (---). Due to the frozen actuator position, the WRBM increases as seen in Figure 5.33b. Compared to the open-loop case, however, the WRBM is still reduced since the mid and inner flaps are still in operation. After a fault detection time of a bit more than 1 s, which is reasonable as evaluated in [115], the GLA controller is reconfigured and control allocation is activated at around 5 s. From thereon, the demanded control effort is distributed to the two inner flaps while the command to the faulty actuator is set to zero. Clearly visible in Figure 5.33a are the increased deflections commanded to the inner (—) and mid (—) flap in the fourth segment. Thereby, controller performance in

terms of WRBM reduction is not only recovered but actually outperformed as it can be seen in Figure 5.33b. The reason for this continues to be the large backlash of the inner flap as confirmed by nonlinear simulations. Furthermore, the peaks in the inner flap command are a compensation of the saturation of the mid flap command, which is limited to $\pm 4^\circ$ in the control allocation. This shows that the control allocation allows handling both deflection limitations and actuator faults at the same time. Within this final experiment, also the transition behavior of the GLA controller is investigated. As desired and visible in Figure 5.33, the transitions between the different controller configurations are smooth and bumpless during the entire experiment. Based on the discussed results, the designed GLA system is successfully validated, demonstrating that the proposed combination of \mathcal{H}_2 -optimal blending and control allocation is well suited for modal damping under actuator constraints.

6 Conclusions

This thesis develops modal control approaches for mitigating adverse aeroelastic effects, i.e., undesired couplings of structural dynamics and aerodynamics, which often arise in highly fuel-efficient aircraft designs. The challenge thereby is the high complexity of the given control problem resulting from high-order plant models and a continuously increasing number of effectors and sensors. To reduce the complexity of the control problem, a “divide and conquer” strategy is applied in this thesis. More precisely, it is proposed to divide controller design into a blending vector design for generating dedicated virtual inputs and outputs, and a subsequent single-input single-output (SISO) controller design. In this way, controller design and tuning is greatly facilitated, where the focus of this thesis is put on developing corresponding blending vector design methods.

In general, blending the inputs and outputs of a system does not affect its poles but rather changes the overall system gain and generates additional zeros. Hence, the gripping question is where to place the additional zeros in order to achieve desired closed-loop specifications with minimum feedback gains. To this end, two different blending approaches are developed in this thesis, initially considering only a single dynamic mode to be controlled. The first blending method optimally places an additional zero such that the controllability and observability of the blended mode is maximized in terms of the \mathcal{H}_2 norm. This approach is then extended in the second blending method, which further enforces a specified root locus enabling a desired pole shift by static gain feedback. Both blending approaches aim at keeping the gains of the subsequently designed SISO controllers small in order to reduce control action and increase robustness. Thereby, the second blending method assumes the SISO controllers to be static whereas the first blending method allows for advanced SISO controllers including, e.g., high order filters or scheduled gains.

In both blending methods, the respective blending vector design problem is formulated as an unconstrained optimization problem of a single variable. This means that controller synthesis becomes independent of the number of actual inputs and outputs, making it extremely well suited for over-actuated and over-sensed systems. Furthermore, it is highlighted that a pair of input and output blending vectors is computed jointly and not separately or iteratively as it is the case in many other blending approaches as reviewed in Chapter 2. Separately blending inputs and outputs generally leads to a simplified blending

vector design problem but often results in suboptimal overall solutions, which is demonstrated by means of a numerical example in Section 3.2.6. Moreover, the algorithm proposed for deriving \mathcal{H}_2 -optimal blending vectors is based on a specially developed formula for computing the \mathcal{H}_2 norm of first- and second-order linear time-invariant (LTI) systems. This formula is considered as one of the major contributions of this thesis and may serve as a basis for developing further analysis and synthesis methods. Note that the \mathcal{H}_2 -optimal blending approach is not to be confused with \mathcal{H}_2 -optimal control approaches such as the linear-quadratic regulator (LQR) which requires solving a Riccati equation.

In order to ensure that residual modes are not affected, it is further proposed to make them uncontrollable or unobservable in the generated virtual inputs and outputs. This is achieved by considering additional orthogonality constraints during blending vector design, which yield zeros at the pole locations of the residual modes. Note that this is not to be confused with standard pole-zero cancellations where the corresponding zeros are introduced by derivative terms in the controller, which should generally be avoided due to robustness reasons. The proposed mode decoupling approach can be seen as a useful alternative to well-established dynamic filtering techniques, which generally require a sufficient frequency separation of the considered modes. To further consider actuator constraints such as saturation or faults, it is proposed to augment the developed control laws with a real-time control allocation. The control allocation distributes the virtual control inputs to the actual control inputs such that actuator constraints are not violated and nominal controller performance is maintained as effectively as possible.

The developed blending approaches are applied to three aeroelastic systems, where each one implicates a different problem formulation and different design challenges. This demonstrates the versatility and sophistication of the proposed blending approaches. In the first application, the first two wing bending modes of a large transport aircraft are actively damped in order to reduce structural loads during gust encounters. Thereby, it is important that residual system dynamics such as rigid-body motions are not affected. This is achieved by mode decoupling constraints considered during blending vector design, where both blending methods are compared under the same conditions. Additionally, systematic procedures are given for the design and tuning of the respective SISO controllers, incorporating robustness requirements and actuator limitations. Both controllers are thoroughly evaluated by means of standardized gust simulations and show a similarly good performance of more than 15% bending moment reduction at the wing root.

In the second application two unstable modes of a highly flexible flutter demonstrator unmanned aerial vehicle (UAV) are successfully stabilized, increasing its operational velocity range by around 15%. The so-called flutter suppression controller is designed using a generalized version of the \mathcal{H}_2 -optimal

blending approach demonstrating its applicability to unstable systems for which the \mathcal{H}_2 norm is not defined. The effectiveness of the flutter suppression controller is thoroughly evaluated in nonlinear simulations including the primary flight control law and realistic gust excitations.

In the third application a gust load alleviation system for a highly flexible wing is designed and successfully validated in extensive wind tunnel tests. The designed gust load alleviation system applies the real-time control allocation in combination with the \mathcal{H}_2 -optimal blending approach and demonstrates its effectiveness under actuator constraints and faults. To that end, the structural loads are measured at the wing root and compared with and without the gust load alleviation system for different gust excitations and actuator constraints. Surprisingly, in the test scenario with a faulty outer flap, nominal controller performance is not only maintained but even exceeded. This curious result is traced back to the large backlash of the inner two flaps, which mostly operate within backlash in the nominal case whereas in the failure case, the adverse backlash effect is reduced due to higher deflection commands. This calls for advanced control methods allowing for directly considering backlash, an undesired effect that often occurs in mechanical systems.

In the latter two applications – the flutter demonstrator and the wing in the wind tunnel – the respective SISO controllers are gain-scheduled in order to increase controller performance. In addition to this, it is expected that scheduling not only the SISO controllers but also the blending vectors enables further performance improvements. This is considered as crucial when the shape of the targeted mode changes considerably over time. Hence, future research directions should include an extension of the presented blending methods to allow for a systematic scheduling of the blending vectors. One possibility for this is to formulate LTI blending vector design problems in terms of linear matrix inequalities (LMIs), which can then be easily extended for multiple or parameter-varying models. Corresponding attempts have been published recently, e.g., in [9, 10].

Another subject that should be further investigated is robustness against modeling uncertainties. In the developed control approaches, uncertainties may only be considered during SISO controller design when blending inputs and outputs in the proposed \mathcal{H}_2 -optimal way. To incorporate modeling uncertainties already during blending vector design, methods based on the well established structured singular value μ [117] are generally promising.

A different approach for improving the robustness and performance of a blending-based control law is to combine it with online system identification methods. This allows for an adaption of the control law to varying or unknown system dynamics in real-time. Thereby, an undesired controller behavior may be avoided by restricting the gains of the SISO controllers or the directions of the blending vectors.

One way of doing that is to enforce the blending vectors to be orthogonal on the input or output space of identified residual modes, which allows for an efficient mode decoupling as described in Section 3.4.2. However, fully decoupling the targeted mode in this way requires a sufficient number of inputs and outputs and usually leads to controllers of increased gains. Alternatively, mode decoupling can also be achieved by dynamic filtering, which generally requires a sufficient frequency separation of the considered modes. This comparison reveals that it remains to be investigated how to decouple targeted modes in an efficient and systematic way such that the gains of the overall feedback controller are minimized.

Besides these specific suggestions for generally improving blending-based control laws, the proposed blending methodologies may also be used to select an optimal subset of actuators and sensors for controlling one or multiple modes. Naturally, large elements in an input or output blending vector indicate a good controllability or observability of the mode they are designed for. Note that in this regard, \mathcal{H}_2 -optimal blending vectors allow for a rather general statement whereas blending vectors computed for pole placement consider a static gain feedback and require to specify the desired root locus beforehand.

The above suggestions show, on the one hand, a number of frontiers yet to be addressed for transferring the developed methodologies into modern-day design practice. On the other hand, the great potential of blending-based control is revealed, opening up new possibilities to solve challenging control problems. This is enabled by interpreting multivariable control laws as a combination of blending vectors, i.e., directions, and SISO controllers, i.e., gain and phase adjustments. In this way, the rather complex process of multivariable controller design and tuning becomes clearer and easier to understand, which is crucial for an application on an industrial level. The promising results from advanced simulations and wind tunnel tests greatly motivate further research activities, where one of the next steps will be an in-flight validation of the flutter suppression controller developed in this thesis.

A Appendix

A.1 Linear Independent Inputs and Outputs

In order to generate a minimum number of linearly independent inputs and outputs of over-actuated and over-sensed systems, the following decomposition is proposed.

Lemma A.1 (Decomposition of over-actuated or over-sensed LTI systems). *Let the transfer function matrix of a strictly proper LTI system $G(s)$ of order n_x be given and have n_u inputs and n_y outputs. Then, there exists a decomposition*

$$G(s) = Q_C \tilde{G}(s) Q_B^T, \quad (\text{A.1})$$

where $\tilde{G}(s)$ describes a strictly proper LTI system of order n_x with $n_{\tilde{u}} \leq n_x$ linearly independent inputs and $n_{\tilde{y}} \leq n_x$ linearly independent outputs, and both $Q_C \in \mathbb{R}^{n_y \times n_{\tilde{y}}}$ and $Q_B \in \mathbb{R}^{n_u \times n_{\tilde{u}}}$ form an orthonormal basis, respectively.

Proof. Let the transfer function matrix of a strictly proper LTI system be given as

$$G(s) = C (sI - A)^{-1} B,$$

where $A \in \mathbb{R}^{n_x \times n_x}$, $B \in \mathbb{R}^{n_x \times n_u}$ and $C \in \mathbb{R}^{n_y \times n_x}$ describe a minimal state space realization of $G(s)$. Then, a thin QR decomposition [49] is carried out on

$$\begin{aligned} B^T &= Q_B R_B, \\ C &= Q_C R_C, \end{aligned}$$

which allows writing

$$\tilde{G}(s) = R_C (sI - A)^{-1} R_B^T,$$

where $R_B \in \mathbb{R}^{n_{\tilde{u}} \times n_{\tilde{u}}}$, $R_C \in \mathbb{R}^{n_{\tilde{y}} \times n_{\tilde{y}}}$, and both $Q_B \in \mathbb{R}^{n_u \times n_{\tilde{u}}}$ and $Q_C \in \mathbb{R}^{n_y \times n_{\tilde{y}}}$ form orthonormal bases, respectively. \square

Remark A.1. The proof may also be derived using other matrix decompositions such as a singular value decomposition (SVD).

A.2 Proportional-Derivative Controller for Mode Damping

In general, modal velocity feedback allows for changing the damping of a mode without affecting its natural frequency [13, 125]. In case modal velocity is not directly measured, it can be computed from a given sensor signal by means of a proportional-derivative filter, assuming that no direct feedthrough is present. This is shown by the following proposition, where an oscillating mode with a single input and a single output is considered.

Proposition A.1 (Proportional-Derivative Controller for Mode Damping). *Let the transfer function $m(s) = \frac{\alpha s + \beta}{s^2 + 2\zeta\omega_n s + \omega_n^2}$ with $\alpha \in \mathbb{R}$ and $\beta \in \mathbb{R}_{\neq 0}$ be given and feature a relative damping $\zeta \in \mathbb{R}$ and a natural frequency $\omega_n \in \mathbb{R}_{\geq 0}$. Then, the relative damping of $m(s)$ is changed to a value $\zeta_{cl} \in \mathbb{R}$ by feeding back the outputs to the inputs via the proportional-derivative controller*

$$\lambda(s) = \gamma \left(s + \frac{\alpha\omega_n^2}{\beta} \right), \quad (\text{A.2})$$

where $\gamma = 2\beta\omega_n \frac{\zeta - \zeta_{cl}}{(\alpha\omega_n)^2 - 2\alpha\beta\zeta_{cl}\omega_n + \beta^2}$.

Proof. The proof is given by substituting the feedback controller $\lambda(s)$ from Equation (A.2) into the closed-loop transfer function

$$m_{cl}(s) = \frac{m(s)}{1 - m(s)\lambda(s)} = \frac{\alpha s + \beta}{s^2 + \underbrace{\frac{2\zeta\omega_n\beta - \gamma\beta^2 - \gamma(\alpha\omega_n)^2}{\beta - \alpha\beta\gamma}}_{2\zeta_{cl}\omega_{n,cl}} s + \underbrace{\omega_n^2}_{\omega_{n,cl}^2}}. \quad (\text{A.3})$$

From the denominator in Equation (A.3), two conditions for determining the relative damping ζ_{cl} and natural frequency $\omega_{n,cl}$ of the closed-loop are obtained as

$$\omega_{n,cl}^2 = \omega_n^2, \quad (\text{A.4})$$

$$2\zeta_{cl}\omega_{n,cl} = \frac{2\zeta\omega_n\beta + \gamma\beta - \gamma(\alpha\omega_n)^2}{\beta - \alpha\beta\gamma}. \quad (\text{A.5})$$

While the first condition reveals that the natural frequency is not changed when closing the loop, the feedback gain γ required to achieve a desired ζ_{cl} can be directly computed from the second condition. \square

Remark A.2. For $\beta = 0$ and $\alpha \neq 0$, a relative damping ζ_{cl} is achieved by the closing the loop with the proportional feedback controller $\lambda = 2\omega_n(\zeta - \zeta_{cl})/\alpha$. For more details, see Equation (3.69).

Bibliography

- [1] Ackermann, J. Der Entwurf linearer Regelungssysteme im Zustandsraum. *Automatisierungstechnik*, 20(1-12):297–300, 1972.
- [2] Airbus. A350 XWB Family. <https://www.airbus.com/aircraft/passenger-aircraft/a350xwb-family.html>. Accessed: 2019-12-31.
- [3] Albano, E. and Rodden, W. A doublet-lattice method for calculating lift distributions on oscillating surfaces in subsonic flows. *AIAA Journal*, 7(2):279–285, 1969.
- [4] Annamdas, V. G. M. Review on developments in fiber optical sensors and applications. *International Journal of Materials Engineering*, 1(1):1–16, 2011.
- [5] Apkarian, P., Dao, M. N., and Noll, D. Parametric robust structured control design. *IEEE Transactions on Automatic Control*, 60(7):1857–1869, 2015.
- [6] Apkarian, P., Gahinet, P., and Buhr, C. Multi-model, multi-objective tuning of fixed-structure controllers. *European Control Conference*, pages 856–861. IEEE, 2014.
- [7] Apkarian, P. and Noll, D. Nonsmooth \mathcal{H}_∞ synthesis. *IEEE Transactions on Automatic Control*, 51(1):71–86, 2006.
- [8] Åström, K. and Wittenmark, B. *Adaptive Control*. Dover Publications, 2nd edition edition, 1995.
- [9] Baár, T. and Luspay, T. An $\mathcal{H}_2/\mathcal{H}_\infty$ blending for mode decoupling. *2019 American Control Conference*, pages 175–180, 2019.
- [10] Baár, T. and Luspay, T. Decoupling through input-output blending. *European Journal of Control*, 2020.
- [11] Bakule, L. Decentralized control: An overview. *Annual reviews in control*, 32(1):87–98, 2008.
- [12] Balas, M. Feedback control of flexible systems. *IEEE Transactions on Automatic Control*, pages 673–679, 1978.

- [13] Balas, M. Direct velocity feedback control of large space structures. *Journal of Guidance, Control, and Dynamics*, 2(3):252–253, 1979.
- [14] Bals, J. *Aktive Schwingungsdämpfung flexibler Strukturen*. PhD thesis, Karlsruhe Institute of Technology, 1989.
- [15] Barbarino, S., Bilgen, O., Ajaj, R. M., Friswell, M. I., and Inman, D. J. A review of morphing aircraft. *Journal of intelligent material systems and structures*, 22(9):823–877, 2011.
- [16] Bernstein, D. What makes some control problems hard? *IEEE Control Systems Magazine*, 22(4):8–19, 2002.
- [17] Bisplinghoff, R., Ashley, H., and Halfman, R. *Aeroelasticity*. Addison-Wesley, Cambridge, Mass, 1955.
- [18] Blight, J., Dailey, L., and Gangsaas, D. Practical control law design for aircraft using multivariable techniques. *International Journal of Control*, 59(1):93–137, 1994.
- [19] Bodson, M. Evaluation of optimization methods for control allocation. *Journal of Guidance, Control, and Dynamics*, 25(4):703–711, 2002.
- [20] Boeing. 777X By Design. <http://www.boeing.com/commercial/777x/by-design/#/777-8-characteristics>. Accessed: 2019-12-31.
- [21] Boskovic, J., Wise, R., and Jackson, J. A flutter suppression and drag optimization approach for flexible aircraft. *58th AIAA/ASCE/AHS/ASC Structures, Structural Dynamics, and Materials Conference*, 2017.
- [22] Boyd, S. and Vandenberghe, L. *Convex optimization*. Cambridge university press, 2004.
- [23] Chughtai, S. and Munro, N. Diagonal dominance using LMIs. *IEE Proceedings - Control Theory and Applications*, 151(2):225–233, 2004.
- [24] Collar, A. R. The expanding domain of aeroelasticity. *The Aeronautical Journal*, 50(428):613–636, 1946.
- [25] Danowsky, B. Flutter suppression of a small flexible aircraft using MIDAAAS. *AIAA Atmospheric Flight Mechanics Conference*, page 4353, 2017.
- [26] Danowsky, B., Thompson, P., Lee, D.-C., and Brenner, M. Modal isolation and damping for adaptive aeroservoelastic suppression. *AIAA Atmospheric Flight Mechanics Conference*, Boston, USA, 2013.

-
- [27] Davison, E., Aghdam, A., and Miller, D. *Decentralized Control of Large-Scale Systems*. Springer, 2020.
- [28] De Lathauwer, L., De Moor, B., and Vandewalle, J. Jacobi-algorithm for simultaneous generalized schur decomposition in higher-order-only ica. In *Proc. of the IEEE Benelux Signal Processing Symposium (SPS98), Leuven, Belgium*, pages 67–70, 1998.
- [29] De Schutter, J., Torfs, D., Bruyninckx, H., and Dutré, S. Invariant hybrid force/position control of a velocity controlled robot with compliant end effector using modal decoupling. *The International Journal of Robotics Research*, 16(3):340–356, 1997.
- [30] Dillinger, J., Meddaikar, M. Y., Lübker, J., Pusch, M., and Kier, T. Design and optimization of an aeroservoelastic wind tunnel model. *International Forum on Aeroelasticity and Structural Dynamics*, Savannah, Georgia, USA, 2019.
- [31] Dillinger, J. K. S., Meddaikar, Y. M., Lübker, J., Pusch, M., and Kier, T. Design and optimization of an aeroservoelastic wind tunnel model. *Fluids*, 5(1), 2020.
- [32] Dowell, E., Clark, R., Cox, D., Curtiss, H., Edwards, J., Hall, K., Peters, D., Scanlan, R., Simiu, E., Sisto, F., and Strganac, T. *A modern course in aeroelasticity*. Springer, 2004.
- [33] Doyle, J. C., Glover, K., Khargonekar, P. P., and Francis, B. A. State-space solutions to standard \mathcal{H}_2 and \mathcal{H}_∞ control problems. *IEEE Transactions on Automatic control*, 34(8):831–847, 1989.
- [34] Durham, W., Bordignon, K. A., and Beck, R. *Aircraft Control Allocation*. John Wiley & Sons, 2016.
- [35] European Aviation Safety Agency. Proposed special condition for installation of flutter suppression system; applicable to Boeing B 747-8F/-8. <https://www.easa.europa.eu/sites/default/files/dfu/SC%20C-18%20for%20publication.pdf>, 2011. Accessed: 2019-12-31.
- [36] European Aviation Safety Agency. *Certification Specifications and Acceptable Means of Compliance for Large Aeroplanes, CS-25, Amendment 16*, 2015.
- [37] Fan, W., Liu, H., and Kwong, R. Gain-scheduling control of flexible aircraft with actuator saturation and stuck faults. *Journal of Guidance, Control, and Dynamics*, 40(3):510–520, 2017.

- [38] Federal Aviation Administration. *Federal Aviation Regulations Part 25, Airworthiness Standards: Transport Category*, 2015.
- [39] The FLEXOP project. <https://www.flexop.eu>. Accessed: 2019-11-30.
- [40] Föllinger, O. and Konigorski, U. *Regelungstechnik: Einführung in die Methoden und ihre Anwendung*. VDE Verlag, 2013.
- [41] Fransen, S. An overview and comparison of OTM formulations on the basis of the mode displacement method and the mode acceleration method. *Worldwide Aerospace Conference & Technology Showcase, MSC Software Corporation, Toulouse, France, April*, pages 8–10, 2002.
- [42] Friswell, M. On the design of modal actuators and sensors. *Journal of Sound and Vibration*, 241(3):361–372, 2001.
- [43] Gözse, I., Luspay, T., Péni, T., Szabó, Z., and Vanek, B. Model order reduction of lpv systems based on parameter varying modal decomposition. In *Proc. of 2016 IEEE 55th Conference on Decision and Control*, pages 7459–7464, Dec 2016.
- [44] Garcia, C. E., Prett, D. M., and Morari, M. Model predictive control: theory and practice - a survey. *Automatica*, 25(3):335–348, 1989.
- [45] Gawronski, W. Modal actuators and sensors. *Journal of Sound and Vibration*, 229:1013–1022, 2000.
- [46] Gawronski, W. and Lim, K. Balanced actuator and sensor placement for flexible structures. *International Journal of Control*, 65(1):131–145, 1996.
- [47] Gawronski, W. K. *Dynamics and control of structures: A modal approach*. Springer Science & Business Media, 2004.
- [48] Glover, K. All optimal hankel-norm approximations of linear multivariable systems and their \mathcal{L}_∞ -error bounds. *International journal of control*, 39(6):1115–1193, 1984.
- [49] Golub, G. and Van Loan, C. F. *Matrix Computations*. Johns Hopkins University Press, 1985.
- [50] Govers, Y., Böswald, M., Lubrina, P., Giclais, S., Stephan, C., and Botargues, N. Airbus A350XWB ground vibration testing: Efficient techniques for customer oriented on-site modal identification. In *Proc. of the International Conference on Noise and Vibration Engineering. KU Leuven, Belgium*, pages 2503–2516, 2014.

-
- [51] Gracey, W. *Measurement of aircraft speed and altitude*. John Wiley & Sons, 1981.
- [52] Grosdidier, P. and Morari, M. Interaction measures for systems under decentralized control. *Automatica*, 22(3):309–319, 1986.
- [53] Guyan, R. J. Reduction of stiffness and mass matrices. *AIAA Journal*, 3(2):380–380, 1965.
- [54] Hać, A. and Liu, L. Sensor and actuator location in motion control of flexible structures. *Journal of sound and vibration*, 167(2):239–261, 1993.
- [55] Hamdan, A. and Nayfeh, A. Measures of modal controllability and observability for first-and second-order linear systems. *Journal of guidance, control, and dynamics*, 12(3):421–428, 1989.
- [56] Hanel, M. *Robust integrated flight and aeroelastic control system design for a large transport aircraft*. PhD thesis, Universität Stuttgart, 2001.
- [57] Hawkins, D. J. Pseudodiagonalisation and the inverse-Nyquist array method. In *Proc. of the Institution of Electrical Engineers*, volume 3, pages 337–342, 1972.
- [58] Haykin, S. *Adaptive filter theory*. Pearson Education India, 2005.
- [59] Hirsch, M. and Smale, S. *Differential Equations, Dynamical Systems, and Linear Algebra*. Academic Press, Inc., San Diego, CA, USA, 1974.
- [60] Hjartarson, A., Seiler, P., and Balas, G. LPV analysis of a gain scheduled control for an aeroelastic aircraft. *American Control Conference*, pages 3778–3783. IEEE, 2014.
- [61] Hoblit, F. *Gust loads on aircraft: concepts and applications*. AIAA, 1988.
- [62] Hönlinger, H., Zimmermann, H., Sensburg, O., and Becker, J. Structural aspects of active control technology. *AGARD Flight Mechanics Panel Symposium*, Turin, Italy, 1995.
- [63] Hoogendijk, R., Heertjesand, M., van de Molengraft, R., and Steinbuch, M. Directional notch filters for motion control of flexible structures. *Mechatronics*, 24(6):632–639, 2014.
- [64] Hovd, M., Braatz, R., and Skogestad, S. SVD controllers for \mathcal{H}_2 -, \mathcal{H}_∞ and μ -optimal control. *Automatica*, 33(3):433–439, 1997.

- [65] Hovd, M. and Skogestad, S. Sequential design of decentralized controllers. *Automatica*, 30(10):1601–1607, 1994.
- [66] Hung, Y. and MacFarlane, A. *Multivariable feedback: a quasi-classical approach*. Springer-Verlag, 1982.
- [67] Inman, D. Modal decoupling conditions for distributed control of flexible structures. *Journal of Guidance, Control, and Dynamics*, 7(6):750–752, 1984.
- [68] International Energy Agency. *Transport, Energy and CO₂*, 2009.
- [69] ISO 2533:1975. Standard atmosphere. Standard, International Organization for Standardization, Geneva, Switzerland, 1975.
- [70] Jelcic, G., Schwochow, J., Govers, Y., Hebler, A., and Böswald, M. Real-time assessment of flutter stability based on automated output-only modal analysis. In *Proc. of the International Conference on Noise and Vibration Engineering. KU Leuven, Belgium*, 2014.
- [71] Jelcic, G., Schwochow, J., Govers, Y., Sinske, J., Buchbach, R., and Springer, J. Online monitoring of aircraft modal parameters during flight test based on permanent output-only modal analysis. *58th AIAA/ASCE/AHS/ASC Structures, Structural Dynamics, and Materials Conference*, 2017.
- [72] Johansen, T. and Fossen, T. Control allocation - a survey. *Automatica*, 49(5):1087–1103, 2013.
- [73] Joos, H.-D. Multi-objective parameter synthesis (mops). In *Robust Flight Control*, pages 199–217. Springer, 1997.
- [74] Kailath, T. *Linear systems*, volume 156. Prentice-Hall Englewood Cliffs, NJ, USA, 1980.
- [75] Kalman, R. E. On the general theory of control systems. In *Proceedings First International Conference on Automatic Control, Moscow, USSR*, 1960.
- [76] Karpel, M. Design for active flutter suppression and gust alleviation using state-space aeroelastic modeling. *Journal of Aircraft*, 19(3):221–227, 1982.
- [77] Karpel, M. and Strul, E. Minimum-state unsteady aerodynamic approximations with flexible constraints. *Journal of Aircraft*, 33(6):1190–1196, 1996.

-
- [78] Karpel, M., Moulin, B., and Chen, P. Dynamic response of aeroservoelastic systems to gust excitation. *Journal of Aircraft*, 42(5):1264–1272, 2005.
- [79] Kier, T. and Looye, G. Unifying manoeuvre and gust loads analysis models. *International Forum on Aeroelasticity and Dynamics. Seattle, USA*, 2009.
- [80] Knobloch, A. *Robust performance analysis for gust loads computation*. PhD thesis, Technische Universität Hamburg, 2015.
- [81] Kotikalpudi, A., Danowsky, B., Schmidt, D., Theis, J., and Seiler, P. Flutter suppression control design for a small, flexible flying-wing aircraft. *Multidisciplinary Analysis and Optimization Conference*, page 3426, 2018.
- [82] Kouvaritakis, B. *Characteristic locus methods for multivariable feedback systems design*. PhD thesis, University of Manchester Institute of Science and Technology, 1974.
- [83] Kraft, M. and White, N. *MEMS for Automotive and Aerospace Applications*. Woodhead Publishing, Cambridge, UK, 2013.
- [84] Kroll, N. and Rossow, C.-C. Digital-X: DLRs way towards the virtual aircraft. *NIA CFD Conference*, pages 6–8, 2012.
- [85] Kroo, I. A general approach to multiple lifting surface design and analysis. *AIAA paper*, 1984.
- [86] Krüger, W. R., Dillinger, J., Meddaikar, M. Y., Lübker, J., Tang, M., Meier, T., Pusch, M., and Kier, T. Design and wind tunnel test of an actively controlled flexible wing. *International Forum on Aeroelasticity and Structural Dynamics*, Savannah, GA, USA, 2019.
- [87] Leith, D. and Leithead, W. Survey of gain-scheduling analysis and design. *International journal of control*, 73(11):1001–1025, 2000.
- [88] Levin, J., Pérez-Arancibia, N., and Ioannou, P. Adaptive notch filter using real-time parameter estimation. *IEEE Transactions on Control Systems Technology*, 19(3):673–681, 2010.
- [89] Litz, L. *Reduktion der Ordnung linearer Zustandsraummodelle mittels modaler Verfahren*. Datenverarbeitung. Hochschul-Verlag, 1979.
- [90] Litz, L. Order reduction of linear state-space models via optimal approximation of the nondominant modes. *IFAC Proceedings Volumes*, 13(6):195 – 202, 1980.

- [91] Liu, L., Tian, S., Xue, D., Zhang, T., Chen, Y., and Zhang, S. A review of industrial MIMO decoupling control. *International Journal of Control, Automation and Systems*, 17(5):1246–1254, 2019.
- [92] Livne, E. Integrated aeroservoelastic optimization: Status and direction. *AIAA Journal of Aircraft*, 36(1):122–145, 1999.
- [93] Livne, E. Future of airplane aeroelasticity. *Journal of Aircraft*, 40(6):1066–1092, 2003.
- [94] Livne, E. Aircraft active flutter suppression: State of the art and technology maturation needs. *Journal of Aircraft*, 55(1):410–452, 2018.
- [95] Luenberger, D. G. Observing the state of a linear system. *IEEE transactions on military electronics*, 8(2):74–80, 1964.
- [96] Luspay, T., Baár, T., Teubl, D., Vanek, B., Ossmann, D., Wüstenhagen, M., Pusch, M., Kier, T., Waitman, S., Ianelli, A., Marcos, A., and Lowenberg, M. Flight control design for a highly flexible flutter demonstrator. *AIAA Atmospheric Flight Mechanics Conference*, San Diego, USA, 2019.
- [97] MacFarlane, A. and Kouvaritakis, B. A design technique for linear multivariable feedback systems. *International Journal of Control*, 25(6):837–874, 1977.
- [98] Maciejowski, J. Multivariable feedback design. *Electronic Systems Engineering Series*, 1989.
- [99] Mayne, D. The design of linear multivariable systems. *Automatica*, 9(2):201–207, 1973.
- [100] Meddaikar, Y., Dillinger, J., Klimmek, T., Krüger, W., Wüstenhagen, M., Kier, T., Hermanutz, A., Hornung, M., Rozov, V., Breitsamter, C., Alderman, J., Takarics, B., and Vanek, B. Aircraft aeroservoelastic modelling of the FLEXOP unmanned flying demonstrator. *AIAA Atmospheric Flight Mechanics Conference*, San Diego, CA, 2019.
- [101] Mees, A. Achieving diagonal dominance. *Systems & Control Letters*, 1(3):155–158, 1981.
- [102] Meirovitch, L. *Dynamics and control of structures*. John Wiley & Sons, 1990.
- [103] Meirovitch, L. *Fundamentals of Vibrations*. McGraw-Hill, 2001.

- [104] Meirovitch, L., Baruh, H., and Öz, H. A comparison of control techniques for large flexible systems. *Journal of Guidance, Control, and Dynamics*, 6(4):302–310, 1983.
- [105] Moore, B. Principal component analysis in linear systems: Controllability, observability, and model reduction. *IEEE transactions on automatic control*, 26(1):17–32, 1981.
- [106] Moorhouse, D. and Woodcock, R. *US Military Specification MIL-F-8785C*, 1980.
- [107] Morari, M. and Lee, J. H. Model predictive control: past, present and future. *Computers & Chemical Engineering*, 23(4):667 – 682, 1999.
- [108] Moreno, C., Seiler, P., and Balas, G. Model reduction for aeroservoelastic systems. *Journal of Aircraft*, 51:280–290, 01 2014.
- [109] Mukhopadhyay, V. Historical perspective on analysis and control of aeroelastic responses. *Journal of Guidance, Control, and Dynamics*, 26(5):673–684, 2003.
- [110] Murty, K. *Linear programming*. John Wiley & Sons, 1983.
- [111] Nguyen, N. Elastically shaped future air vehicle concept. *NASA Innovation Fund Award*, 2010.
- [112] Nguyen, N. and Tal, E. A multi-objective flight control approach for performance adaptive aeroelastic wing. *56th AIAA Structures, Structural Dynamics, and Materials Conference*, 2015.
- [113] Nguyen, N. and Urnes, J. Aeroelastic modeling of elastically shaped aircraft concept via wing shaping control for drag reduction. *AIAA Atmospheric Flight Mechanics Conference*, page 4642, 2012.
- [114] Ossmann, D., Luspay, T., and Vanek, B. Baseline Flight Control System Design for an Unmanned Flutter Demonstrator. In *Proc. of IEEE Aerospace Conference*, Big Sky, MT, 2019. IEEE.
- [115] Ossmann, D. and Pusch, M. Fault tolerant control of an experimental flexible wing. *Aerospace*, 6(7), 2019.
- [116] Owens, D. Dyadic expansion, characteristic loci and multivariable-control-systems design. In *Proc. of the Institution of Electrical Engineers*, volume 122(3), pages 315–320. IET, 1975.

- [117] Packard, A. and Doyle, J. The complex structured singular value. *Automatica*, 29(1):71–109, 1993.
- [118] Packard, A., Doyle, J., and Balas, G. Linear, multivariable robust control with a μ perspective. *ASME Journal of Dynamic Systems, Measurement and Control*, 1993.
- [119] Pernebo, L. and Silverman, L. Model reduction via balanced state space representations. *IEEE Transactions on Automatic Control*, 27(2):382–387, 1982.
- [120] Porter, B. and Crossley, R. *Modal control theory and applications*. Taylor and Francis, London, UK, 1972.
- [121] Preumont, A. *Vibration control of active structures*. Springer, 1997.
- [122] Pusch, M. Allocation of distributed flaps for gust load alleviation. In *Proc. of 1st IEEE Conference on Control Technology and Applications*, pages 2120–2125, Kohala Coast, Hawaii, USA, 2017.
- [123] Pusch, M. Aeroelastic mode control using \mathcal{H}_2 -optimal blends for inputs and outputs. *AIAA Guidance, Navigation, and Control Conference*, Orlando, FL, USA, 2018.
- [124] Pusch, M., Knoblach, A., and Kier, T. Integrated optimization of ailerons for active gust load alleviation. *International Forum on Aeroelasticity and Structural Dynamics*, Saint Petersburg, Russia, 2015.
- [125] Pusch, M. and Ossmann, D. Blending of inputs and outputs for modal velocity feedback. *27th IEEE Mediterranean Conference on Control and Automation*, Akko, Israel, 2019.
- [126] Pusch, M. and Ossmann, D. \mathcal{H}_2 -optimal Blending of Inputs and Outputs for Modal Control. *IEEE Transactions on Control System Technology*, 2019.
- [127] Pusch, M., Ossmann, D., Dillinger, J., Kier, T., Tang, M., and Lübker, J. Aeroelastic modeling and control of an experimental flexible wing. *AIAA Guidance, Navigation, and Control Conference*, San Diego, USA, 2019.
- [128] Pusch, M., Ossmann, D., and Luspay, T. Structured control design for a highly flexible flutter demonstrator. *Aerospace*, 6(3), 2019.
- [129] Pusch, M., Theis, J., and Ossmann, D. Partial pole placement using static output feedback. *21st IFAC World Congress*, Berlin, Germany, 2020.

-
- [130] Quero, D., Vuillemin, P., and Poussot-Vassal, C. A generalized state-space aeroservoelastic model based on tangential interpolation. *Aerospace*, 6(1):9, 2019.
- [131] Rayleigh, J. W. S. B. *The theory of sound*, volume 2. Macmillan, 1877.
- [132] Regan, C. and Jutte, C. Survey of applications of active control technology for gust alleviation and new challenges for lighter-weight aircraft. Technical Report NASA/TM-2012-216008, NASA, 2012.
- [133] Rodden, W. and Johnson, E. *MSC.Nastran Version 68, Aeroelastic Analysis and User's Guide*, 2004.
- [134] Rodriguez, D., Aftosmis, M., Nemec, M., and Anderson, G. Optimization of flexible wings with distributed flaps at off-design conditions. *Journal of Aircraft*, 53(6):1731–1745, 2016.
- [135] Roger, K. L. Airplane math modelling methods for active control design. *Structures and Materials Panel*, 1977.
- [136] Roppenecker, G. Polvorgabe durch Zustandsrückführung. *at-Automatisierungstechnik*, 29(1-12):228–233, 1981.
- [137] Rosenbrock, H. Distinctive problems of process control. *Chemical Engineering Progress*, 58(9):43–50, 1962.
- [138] Rößler, C., Stahl, P., Sendner, F., Hermanutz, A., K̄berle, S., Bartasevicius, J., Rozov, V., Breitsamter, C., Hornung, M., Meddaikar, Y., Dillinger, J., Sodja, J., Breuker, R. D., Koimtzoglou, C., Kotinis, D., and Georgopoulos, P. Aircraft design and testing of FLEXOP unmanned flying demonstrator to test load alleviation and flutter suppression of high aspect ratio flexible wings. *AIAA Atmospheric Flight Mechanics Conference*, San Diego, CA, 2019.
- [139] Rozov, V., Volmering, A., Hermanutz, A., Hornung, M., and Breitsamter, C. CFD-based aeroelastic sensitivity study of a low-speed flutter demonstrator. *Aerospace*, 6(3), 2019.
- [140] Russell, S. and Norvig, P. *Artificial intelligence: a modern approach*. Malaysia; Pearson Education Limited,, 2016.
- [141] Sadabadi, M. S. and Peaucelle, D. From static output feedback to structured robust static output feedback: A survey. *Annual Reviews in Control*, 42:11 – 26, 2016.

- [142] Schilders, W., Van der Vorst, H., and Rommes, J. *Model order reduction: theory, research aspects and applications*. Springer, 2008.
- [143] Schmid, C. and Biegler, L. Quadratic programming methods for reduced Hessian SQP. *Computers & chemical engineering*, 18(9):817–832, 1994.
- [144] Schmidt, D. *Modern flight dynamics*. McGraw-Hill New York, 2012.
- [145] Schneiders, M., van de Molengraft, R., and Steinbuch, M. Benefits of over-actuation in motion systems. In *Proc. of American Control Conference*, pages 505–510, Boston, MA, USA, 2004.
- [146] Sendner, F.-M., Stahl, P., Rößler, C., and Hornung, M. Designing an UAV propulsion system for dedicated acceleration and deceleration requirements. In *Proc. of 17th AIAA Aviation Technology, Integration, and Operations Conference, AIAA AVIATION Forum*, Denver, CO, 2017.
- [147] Shamma, J. and Athans, M. Gain scheduling: Potential hazards and possible remedies. *IEEE Control Systems Magazine*, 12(3):101–107, 1992.
- [148] Skogestad, S. and Postlethwaite, I. *Multivariable feedback control: analysis and design*, volume 2. Wiley New York, 2007.
- [149] Stanford, B. Gradient-based aeroservoelastic optimization with static output feedback. *Journal of Guidance, Control, and Dynamics*, 0(0):1–5, 2019.
- [150] Syrmos, V., Abdallah, C., Dorato, P., and Grigoriadis, K. Static output feedback - a survey. *Automatica*, 33(2):125 – 137, 1997.
- [151] Tang, M., Böswald, M., Govers, Y., and Pusch, M. Identification and assessment of a nonlinear dynamic actuator model for gust load alleviation in a wind tunnel experiment. *Deutscher Luft- und Raumfahrtkongress (DLRK)*, Darmstadt, Germany, 2019.
- [152] Tewari, A. Aeroservoelasticity. In *Aeroservoelasticity*. Springer, January 2015.
- [153] Theis, J. *Robust and linear parameter-varying control of aeroservoelastic systems*. Technische Universität Hamburg-Harburg, 2018.
- [154] Theis, J., Pfifer, H., Balas, G., and Werner, H. Integrated flight control design for a large flexible aircraft. *2015 American Control Conference*, pages 3830–3835. IEEE, 2015.

- [155] Theis, J., Pffifer, H., and Peter, S. Robust modal damping control for active flutter suppression. *Journal of Guidance, Control, and Dynamics*, 2020.
- [156] Theis, J., Pffifer, H., and Seiler, P. Robust control design for active flutter suppression. *Atmospheric Flight Mechanics Conference*, San Diego, CA, 2016.
- [157] Theis, J., Seiler, P., and Werner, H. LPV model order reduction by parameter-varying oblique projection. *IEEE Transactions on Control Systems Technology*, 26(3):773–784, 2017.
- [158] Vaes, D. *Optimal static decoupling for multivariable control design*. PhD thesis, University of Leuven, 2005.
- [159] Van De Wal, M. and De Jager, B. A review of methods for input/output selection. *Automatica*, 37(4):487–510, 2001.
- [160] VanAntwerp, J., Featherstone, A., and Braatz, R. Robust cross-directional control of large scale sheet and film processes. *Journal of Process Control*, 11(2):149–177, 2001.
- [161] Varga, A. Balancing-free square-root algorithm for computing singular perturbation approximations. In *Proc. of the 30th IEEE Conference on Decision and Control*, pages 1062–1065, 1991.
- [162] Waszak, M. and Schmidt, D. Flight dynamics of aeroelastic vehicles. *Journal of Aircraft*, 25(6):563–571, 1988.
- [163] Werner, H. Control systems theory and design. Unpublished Lecture Notes, Technical University Hamburg, 2013.
- [164] Widrow, B. and Stearns, S. *Adaptive signal processing*, volume 15. Prentice-hall Englewood Cliffs, NJ, USA, 1985.
- [165] Wu, F. *Control of linear parameter varying systems*. PhD thesis, University of California, Berkeley, 1995.
- [166] Wu, F., Grigoriadis, K., and Packard, A. Anti-windup controller design using linear parameter-varying control methods. *International Journal of Control*, 73(12):1104–1114, 2000.
- [167] Wüstenhagen, M., Kier, T., Pusch, M., Ossmann, D., Meddaikar, M. Y., and Hermanutz, A. Aeroservoelastic modeling and analysis of a highly flexible flutter demonstrator. In *Proc. of Atmospheric Flight Mechanics Conference, AIAA AVIATION Forum*, Atlanta, GA, USA, 2018.

- [168] Wykes, J. H., Borland, C. J., Klepl, M. J., and MacMiller, C. J. Design and development of a structural mode control system. *NASA/CR*, 143846, 1977.
- [169] Zhou, K., Doyle, J., and Glover, K. *Robust and optimal control*, volume 40. Prentice hall, NJ, USA, 1996.
- [170] Zhou, K. and Doyle, J. C. *Essentials of robust control*, volume 104. Prentice hall Upper Saddle River, NJ, USA, 1998.

List of Publications

Lead-authored

- [1] Manuel Pusch, Julian Theis, and Daniel Ossmann. Partial Pole Placement using Static Output Feedback. *21st IFAC World Congress*, Berlin, Germany, 2020.
- [2]* Manuel Pusch, Andreas Knoblach, and Thiemo Kier. Integrated optimization of control surface layout for gust load alleviation. *CEAS Aeronautical Journal*, 2019.
- [3] Manuel Pusch and Daniel Ossmann. Blending of inputs and outputs for modal velocity feedback. *27th IEEE Mediterranean Conference on Control and Automation*, Akko, Israel, 2019.
- [4]* Manuel Pusch, Daniel Ossmann, and Tamás Luspay. Structured control design for a highly flexible flutter demonstrator. *Aerospace*, 6(3), 2019.
- [5] Manuel Pusch, Daniel Ossmann, Johannes Dillinger, Thiemo Kier, Martin Tang, and Jannis Lübker. Aeroelastic modeling and control of an experimental flexible wing. *AIAA Scitech Forum*, San Diego, CA, USA, 2019.
- [6]* Manuel Pusch and Daniel Ossmann. \mathcal{H}_2 -optimal Blending of Inputs and Outputs for Modal Control. *IEEE Transaction of Control System Technology*, 2019.
- [7] Manuel Pusch. Aeroelastic mode control using \mathcal{H}_2 -optimal blends for inputs and outputs. *AIAA Scitech Forum*, Orlando, FL, USA, 2018.
- [8] Manuel Pusch. Allocation of distributed flaps for gust load alleviation. *1st IEEE Conference on Control Technology and Applications*, Kohala Coast, HI, USA, 2017.
- [9] Manuel Pusch, Andreas Knoblach, and Thiemo Kier. Integrated optimization of ailerons for active gust load alleviation. *International Forum on Aeroelasticity and Structural Dynamics*, Saint Petersburg, Russia, 2015.

*peer-reviewed journal publication

Co-authored

- [1]* Johannes Dillinger, Yasser Meddaikar, Jannis Lübker, Manuel Pusch, and Thiemo Kier. Design and optimization of an aeroservoelastic wind tunnel model. *Fluids*, 5(1), 2020.
- [2] Béla Takarics, Bálint Patartics, Tamás Luspay, Balint Vanek, Christian Roessler, Julius Bartasevicius, Sebastian Koeberle, Mirko Hornung, Daniel Teubl, Manuel Pusch, et al. Active flutter mitigation testing on the Flexop demonstrator aircraft. *AIAA Scitech 2020 Forum*, Orlando, FL, USA, 2020.
- [3]* Daniel Ossmann and Manuel Pusch. Fault tolerant control of an experimental flexible wing. *Aerospace*, 6(7), 2019.
- [4] Wolf Reiner Krüger, Johannes Dillinger, Yasser Meddaikar, Jannis Lübker, Martin Tang, Tobias Meier, Manuel Pusch, and Thiemo Kier. Design and wind tunnel test of an actively controlled flexible wing. In *International Forum on Aeroelasticity and Structural Dynamics*, Savannah, GA, USA, 2019.
- [5] Johannes Dillinger, Yasser Meddaikar, Jannis Lübker, Manuel Pusch, and Thiemo Kier. Design and optimization of an aeroservoelastic wind tunnel model. *International Forum on Aeroelasticity and Structural Dynamics*, Savannah, GA, USA, 2019.
- [6] Martin Tang, Marc Böswald, Yves Govers, and Manuel Pusch. Identification and assessment of a nonlinear dynamic actuator model for gust load alleviation in a wind tunnel experiment. *Deutscher Luft- und Raumfahrtkongress*, Darmstadt, Germany, 2019.
- [7] Thiemo Kier, Martin Leitner, Özge Sülözgen, and Manuel Pusch. An integrated flexible aircraft model for optimization of lift distributions. *AIAA Scitech Forum*, San Diego, CA, USA, 2019.
- [8] Tamás Luspay, Tamás Baár, Dániel Teubl, Bálint Vanek, Daniel Ossmann, Matthias Wüstenhagen, Manuel Pusch, Thiemo Kier, Sergio Waitman, Andrea Ianelli, Andres Marcos, and Mark Lowenberg. Flight control design for a highly flexible flutter demonstrator. *AIAA Scitech Forum*, San Diego, CA, USA, 2019.
- [9] Matthias Wüstenhagen, Thiemo Kier, Manuel Pusch, Daniel Ossmann, Muhammad Yasser Meddaikar, and Andreas Hermanutz. Aeroservoelastic modeling and analysis of a highly flexible flutter demonstrator. *AIAA Atmospheric Flight Mechanics Conference*, Atlanta, GA, 2018.

*peer-reviewed journal publication

-
- [10] Felix Goßmann and Manuel Pusch. LPV-Reglerentwurf zur Böenlastabminderung am flexiblen Flugzeug. *Deutscher Luft- und Raumfahrt Kongress*, Braunschweig, Germany, 2016.

Curriculum Vitae

Manuel Pusch born 21.07.1987 in Rohrbach

Employment History

since 07/2013 German Aerospace Center (DLR), Oberpfaffenhofen, Germany
Institute of System Dynamics and Control, Research Assistant.

Education

10/2007–05/2013 Technical University of Munich, Germany,
Aerospace Engineering (Diplom-Ingenieur Univ.).

10/2010–05/2011 Universidad de Antioquia, Medellín, Colombia,
Mechanical Engineering, Term abroad.

09/2001–06/2006 Höhere Technische Bundeslehranstalt Neufelden, Austria,
Business Computer Science, University Entrance Qualification
(Matura).

Internships and Secondary Employments

10/2012–05/2013 Technical University of Munich, Germany,
Institute of Information Technology, Student Employee.

11/2007–09/2011 Technical University of Munich, Germany,
Institute of Materials Handling, Material Flow and Logistics, Student Employee.

08/2005–09/2005 Plasser & Theurer, Linz, Austria,
Institute of Information Technology, Internship.

07/2004–08/2004 VA-Tech Hydro, Linz, Austria,
Institute of Information Technology, Internship.

08/2003 Sprecher Automation, Linz, Austria,
Institute of Information Technology, Internship.